UC Irvine

UC Irvine Electronic Theses and Dissertations

Title

Liquid Transport in Hierarchical Surfaces for Heat Transfer Application

Permalink

https://escholarship.org/uc/item/7sm1h6m6

Author

Lee, Jonggyu

Publication Date

2021

Peer reviewed|Thesis/dissertation

UNIVERSITY OF CALIFORNIA,
IRVINE

Liquid Transport in Hierarchical Surfaces for Heat Transfer Application

DISSERTATION

submitted in partial satisfaction of the requirements
for the degree of

DOCTOR OF PHILOSOPHY

in Mechanical and Aerospace Engineering

by

Jonggyu Lee

Dissertation Committee:
Assistant Professor Yoonjin Won, Chair
Associate Professor Ali Mohraz
Associate Professor Iryna V. Zenyuk

2021

DEDICATION

To

my family and friends

in recognition of their love and support

TABLE OF CONTENTS

LIST OF FIGURES

LIST OF TABLES

ACKNOWLEDGEMENTS

I would not have been able to complete this dissertation without the support and guidance from my mentors, friends, and family.

Firstly, I would like to thank my advisor, Professor Yoonjin Won, for her mentorship that allows me not only to keep continue my work productively but also to build my mindset as a learner, researcher, and tutor. She encourages me to dive into the interesting research topics of nano- and microscale surfaces and transport physics. I also would like to appreciate my academic co-advisor Professor Ali Mohraz for providing critical comments across on my research work, presentation, and scientific writing. He has been always strict in the professional area that shapes my research mindset with integrity, and always kindly supported me to continue my career.

I appreciate Professor Iryna Zenyuk for being a committee member of my dissertation and Qualifying exam. She has been always enthusiastic about the research and being a mentor to guide students. I thank my Qualifying committee, Professor Yun Wang and Professor Lorenzo Valdevit, who have provided invaluable time and effort to review my dissertation proposal. I also thank Dr. Michael Barako and Dr. Mansur Abahusayn for providing insightful and critical comments on my research work and introducing interesting research topics to pursue.

I also owe many thanks to my lab mates at the Won lab and the Colloid Science lab who help me a lot to finish my degree personally and professionally. They have always motivated me to work hard and provided critical insights during the discussions. They also helped me enormously when I faced overwhelmed situation when I could have never overcome by myself. I also deeply thank my dear friends in South Korea. They have encouraged me not to be fallen during my Ph.D. as well as the unprecedented Pandemic.

Last but the most, I deeply appreciate my parents for their unconditional love, understanding, and sacrifice. Any of my achievements would have never been possible without their support. I also would like to thank my family members for their understanding and belief.

VITA

Jonggyu Lee

2008-2013   B.S. in Environmental Materials Science, Seoul National University

2013-2015   M.S. in Environmental Materials Science, Seoul National University

2016-2021   Ph.D. in Mechanical Engineering, University of California, Irvine

FIELD OF STUDY

Materials Science, Heat and Mass Transfer, Energy Storage Devices, Interfacial Phenomena

JOURNAL PUBLICATIONS

1. Jonggyu Lee, Jinyoung So, Won-Gyu Bae, and Yoonjin Won, The design of hydrophilic nanochannel-macrostripe fog collector: Enabling wicking-assisted vertical liquid delivery for the enhancement in fog collection efficiency, *Advanced Materials Interfaces*, 1902150 (2020)

2. Quang Pham, Shiwei Zhang, Shuai Hao, Kimia Montazeri, Cheng-hui Lin, Jonggyu Lee, Ali Mohraz, Yoonjin Won, Boiling Heat Transfer with Well-Ordered Microporous Architecture, *ACS Applied Materials and Interfaces*, (16), 19174-19183 (2020)

3. Duong Vy Le, Quang Pham, Jonggyu Lee, Shiwei Zhang and Yoonjin Won, Evaporative Wicking Phenomenaa on Nanotextured Surfaces, *Journal of Electronic Packaging* (2019)

4. Jonggyu Lee, Bowen, Shao, and Yoonjin Won, Droplet Jumping on Superhydrophobic Copper Oxide Nanostructured Surfaces, *IEEE CPMT* (2018)

5. Jonggyu Lee, Youngjoon Suh, Pranav P. Dubey, Michael T. Barako, and Yoonjin Won, Capillary Wicking in Hierarchically Textured Copper Nanowire Arrays, *ACS Applied Materials and Interfaces* (2018) 11 (1), 1546-1554

6. Ji-Won Park, Gyu-Seong Shim, Jonggyu Lee, Seong-Wook Jang, Hyun-Joong Kim, and Jin-Nyung Choi, Evaluation of UV Curing Properties of Mixture Systems with Differently Sized Monomers, *Materials* (2018) 11 (4), 509

7. Ji-Won Park, Jonggyu Lee, Gyu-Seong Shim, Hyun-Joong Kim, Young-Kwan Kim, Sang-Eun Moon and Dong-Hun No, Evaluation of the Ultraviolet-Curing Kinetics of Ultraviolet-Polymerized Oligomers Cured Using Poly (Ethylene Glycol) Dimethacrylate, *Coatings* (2018) 8 (3), 99

8. Jonggyu Lee, Youbin Kwon, Ji-Young Ju, Sungho Choi, Yongku Kang, Woong-Ryeol Yu, Dong Wook Kim, Fiber electrode prepared by one-pot wet-spinning of graphene and MnO2 nanowire for wearable lithium-ion batteries, *Journal of applied electrochemistry* (2018) 47 (8), 865-875

9. Jonggyu Lee, Gyu-Seong Shim, Ji-Won Park, Hyun-Joong Kim, Kwan-Young Han, Kinetic and mechanical properties of dual curable adhesives for display bonding process, *International Journal of Adhesion and Adhesives* (2016), 70:249-259

10. Jonggyu Lee, Gyu-Seong Shim, Ji-Won Park, Hyun-Joong Kim, Sang-Eun Moon, Young-Kwan Kim, Dong-Hun No, Jong-Hwan Kim, Kwan-Young Han, Curing Behavior and Viscoelastic Property of Dual Curable Adhesives Based on Azo-initiator with High Reactivity, *Journal of Electronic Materials* (2016) 45:3768

CONFERENCE PROCEEDINGS

1. Jonggyu Lee, Bowen Shao, Yoonjin Won, Two-Level Copper Oxide Nanostructured Surfaces for Condensation Heat Transfer, *ITHERM Conference* (2018)

2. Jonggyu Lee, Kyle McDevitt, Ali Mohraz, Yoonjin Won, Wetting Properties of the Bijel-derived Hierarchical Nanostructures for Effective Two-phase Nucleation Boiling*, Droplet Conference* (2017)

CONFERENCE PRESENTATIONS

1. "Condensation Heat Transfer on Hierarchical Copper Inverse Opals" (poster presentation), *InterPACK*, Anaheim, CA, USA, 2019 (Best Poster Award)

2. "Two-Level Copper Oxide Nanostructured Surfaces for Condensation Heat Transfer" (oral and poster presentation), *ITHERM conference*, San Diego, CA, USA , 2018

3. "Wetting Behaviors of the Bijel-derived Hierarchical Nanostructures" (poster presentation), *Droplet Conference*, UCLA, CA, USA, 2017

4. "Preparation and Characterization of Dual Curable Adhesives for Display Bonding Process" (oral presentation), *53th Adhesion Society of Japan*, Aichi Institute of Technology, Nagoya, Japan, 2015

5. "Characterization of Curing Behavior and Viscoelastic Property for Dual Curable Optically Clear Resin" (poster), *The Polymer Society of Korea*, Daejeon, Korea, 2015

6. "Effect of Binder Shrinkage at Sheet Resistance of Electrically Conductive Adhesives" (poster presentation), *The Korean Society of Industrial and Engineering Chemistry*, Daegu, Korea, 2014

7. "Research on Conductivity change of electrically conductive adhesives depends on Shrinkage" (oral presentation), *5th World Congress on Adhesion and Related Phenomena*, Nara, Japan, 2014

8. "Reducing Sheet Resistance of Silver-resin Composite Film with High Curing Shrinkage" (poster presentation), *The Polymer Society of Korea*, Daejeon, Korea, 2014

9. "Predication and Calculation of Properties of the Bio-Composite"(poster), *Mini-Symposium on Green Composite*, Seoul, Korea, 2013

ABSTRACT OF THE DISSERTATION

Liquid Transport in Hierarchical Surfaces for Heat Transfer Application

by

Jonggyu Lee

Doctor of Philosophy in Mechanical and Aerospace Engineering

University of California, Irvine, 2021

Professor Yoonjin Won, Chair

Two-phase heat transfer is an important heat transfer mechanism in many industrial applications that employ phase change processes such as power plants, desalination, and electronic cooling devices owing to its effectiveness at dissipating heat. Especially, as modern electronic devices become smaller, thinner, and higher power-density, advancement of thermal management systems is a crucial issue in terms of electronics' energy efficiency, lifespan, and performance. Recently, the thermal management strategy has been improved by utilizing passive two-phase cooling devices such as heat pipes or vapor chambers, which offer excellent heat dissipation performance by utilizing the latent heat of the liquid. The heat dissipation of passive cooling devices typically encounters operating limitation resulting from a lack of liquid replenish to the evaporator region, so-called capillary limit. To address the capillary limit, microscale porous surfaces such as sintered copper particles, copper microgrooves, and silicon microposts have been suggested as wicking materials. However, such homogeneous porous structures suffer from a tradeoff between two important

parameters: permeability and capillary pressure. The permeability, indicating how permeable liquid is through the porous media, can be improved with large pores, pore interconnection, and low tortuosity of pores. In contrast, capillary pressure is inversely proportional to the pore size. The tradeoff between permeability and capillary pressure as a result of pore size leads to the necessity of design optimization of porous media for efficient liquid transport.

To address this issue, hierarchically structured surfaces composed of structures with different length scales are suggested. The hierarchical surfaces offer significantly improved liquid transport performance by providing desirable properties in different length scales. Specifically, upper hierarchy such as micro or microscale structures provides large pore sizes for liquid pathways offering excellent liquid permeability. Then, the other competing factor, capillary pressure, can be improved in a lower hierarchy such as nanoscale pores and roughness that modifies surface wettability. Although liquid transport into porous media has been studied intensively over decades, understanding the liquid transport in each length scale is still vague due to the complexity of hierarchical geometry. For example, the liquid transport in hierarchical surfaces is dictated by complex parameters such as difference in length scales between hierarchy, surface wettability in the presence of nanoscale structures or heterogeneous properties of the surface.

In this dissertation, we investigate the liquid transport in hierarchical surfaces composed of upper-level hierarchy (e.g., vertically aligned nanowires, bijel-templated porous metal), and lower-level hierarchy (e.g., oxide nanofeatures, nanopores). The capillary-driven liquid transport is systematically investigated through liquid rate-of-rise

test based on the Lucas-Washburn equation. Due to the nanofeatures posing enormous roughness, the wettability of the hierarchical nanowires is significantly improved, resulting in the enhancement of capillary wicking. The capillary wicking through hierarchical surfaces is further confirmed through computational fluid dynamics (CFD) to demonstrate the role of surface wettability and hydraulic resistance. In addition, the hierarchical surfaces with heterogeneous properties successfully improve heat transfer coefficient (HTC) and critical heat flux (CHF) simultaneously by overcoming the competing effect of wettability on boiling heat transfer. The role of nanoscale morphology in liquid infiltration mechanisms is demonstrated through Environmental microscopic observations, in which the wetting through the nanopores occurs at the beginning followed by the liquid transport through the micropores. The findings in the current dissertation will shed light on microscale liquid transport through multiscale materials for various applications such as advanced thermal management systems or energy conversion.

CHAPTER 1: INTRODUCTION

1.1. Challenges in Thermal Management of Electronics

The thermal management of electronics has become of great interest due to the increase in heat generation of modern electronics associated with electronics miniaturization, higher transistor density, and smaller gate length. The increasing power density of the electronics requires heat dissipation over 100 W/cm^2 and is anticipated to increase in the next few years as shown in Figure 1.2a. Also, the non-uniformity of the power distribution of the electronics causes extreme power density exceeding 300 W/cm^2. In addition to that, high power generating systems such as solar photovoltaic cells, light-emitting diode (LED) and gallium nitride (GaN) power electronics demands efficient thermal management system which can handle the power density exceeding 1000 W/cm^2 (Figure 1.2b). The lack of the thermal management system adversely affects electronics' lifespan, performance, and reliability. Although current electronics cooling system could handle the heat dissipation through the forced air-cooling system and thermally conductive heat spreader using copper or nickel plate, the emerging high-power density of the electronics is demanding a more efficient cooling system. Furthermore, the electronics heat dissipation is a crucial issue not only on the chip and packaging module level but also system and facility level of the electronics (Figure 1.1). A rapidly increasing IT industry and communication technology causes an increased demand for electricity. In 2010, 1.5 % of global electricity was consumed by the data centers, and the electricity usage is expected to keep growing associated with the recent growth of the cloud computing system. Therefore, the importance of advancement in thermal management systems is obvious in terms of energy issues and overcome electronics design challenges.
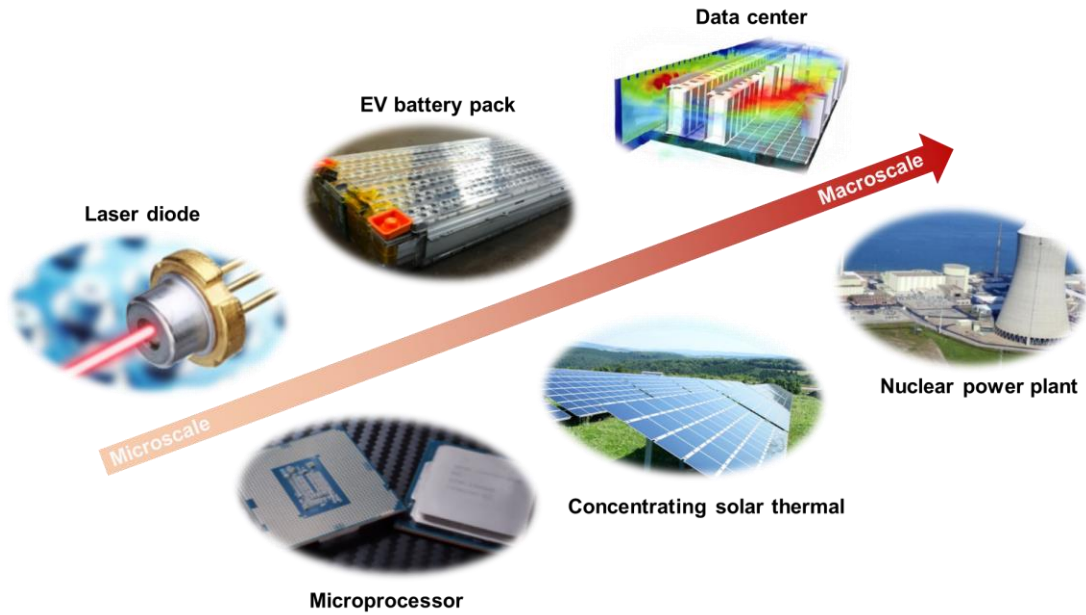
Figure 1.1. Broad impact of thermal energy systems. Efficient heat transfer is crucial for various applications such as electronics cooling, EV battery pack, concentrating solar thermal, and power plants. The process involves multiple heat transfer mechanisms such as nanoscale phonon transport, microscale convective and two-phase heat transfer, and macroscale natural or forced air convection.

1.2. Two-phase Heat Transfer

Two-phase heat transfer has been proposed as a promising solution for the efficient thermal management system of high-power electronic devices since it takes advantage of the latent heat of the fluid during phase change. To be specific, two-phase heat transfer such as boiling and evaporation could obtain at least two order magnitude higher heat transfer coefficient (HTC) compared to the traditional cooling system such as forced air-cooling system and liquid cooling system through convective heat transfer. The HTC of the forced air-cooling system is only up to 0.01 W/cm²K, and that of the forced liquid cooling system can reach up to 10 W/cm²K. On the other hand, the boiling two phase heat transfer can obtain over 100 W/cm²K as shown in Figure 1.3. Two-phase heat transfer using water shows a

superior heat transfer coefficient as the latent heat of water for liquid-vapor phase change is 2260 kJ/kg.
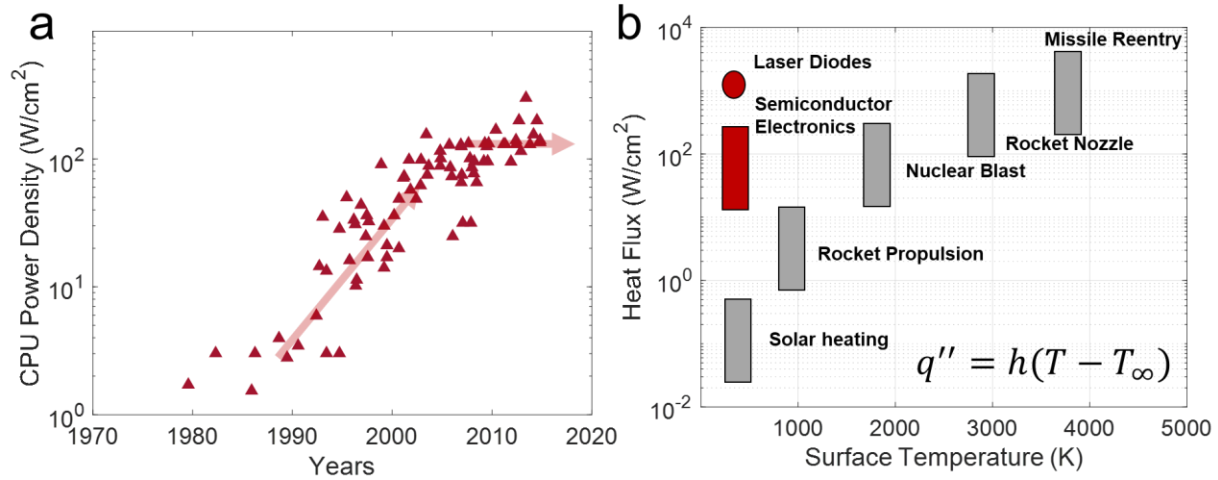
Figure 1.2. Power density of electronics. (a) Power density of successive node of CPU shows over 100 W/cm² of power density. The plot is reproduced from the data from ref [1]. (b) Heat flux comparison with various heat generation processes indicates importance of heat transfer coefficient to maintain operation temperature under high heat flux condition.

In the figure, the equation shown is:
$$q'' = h(T - T_\infty)$$
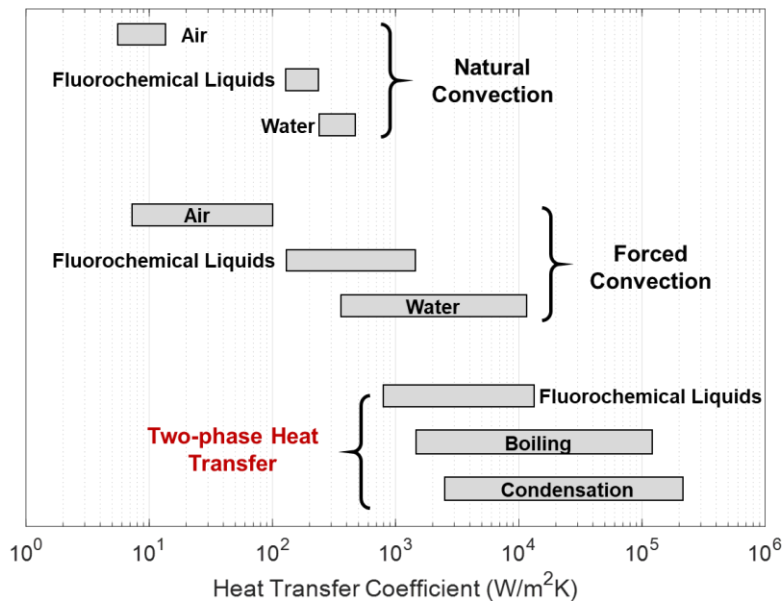
Figure 1.3. Comparison of heat transfer coefficient. The two-phase heat transfer offers two to five order higher heat transfer coefficient than that of natural convection, forced convection. The plot is reproduced from the figure in ref [2].

3

Forced air or liquid cooling system has been used commercially due to its own advantages such as its cost-effectiveness, easiness of maintenance, and simplicity. Due to the limitation of the low HTC of the cooling system associated with a low heat capacity of the air, extended surfaces, such as fin-type heat sink which is a passive heat exchanger, are used to improve heat dissipation efficiency. However, the forced air-cooling system faces the challenge as the electronics' size becomes smaller and thinner since the forced air-cooling system requires relatively large volume for the extended surfaces and cooling fans. The forced liquid cooling system has also been used in the high-power density electronics along with the forced air-cooling system. The liquid is circulated through the pipes and dissipate heat by its higher heat capacity than air. Thus, the forced liquid cooling system shows better heat dissipation than forced air cooling system. But it has also been limited to apply in modern electronics due to the large component such as a circulation system and a heat exchanger, which lowers the efficiency of the electronics due to the extra power consumption. Another limitation is caused by the non-uniformity of the temperature due to the temperature gradient of the working fluid.

Consequently, the passive cooling system with two-phase heat transfer such as heat pipes or vapor chamber has drawn great interest because the system could dissipate heat more efficiently than single phase cooling system without external power input and needing extra pumping system. Furthermore, the passive cooling system could meet the requirement of the demand for the modern electronics which become smaller, thinner, and flexible. The schematic illustration of the passive cooling system (heat pipes) is shown in Figure 1.4. The heat pipes are typically composed of four sections: 1) evaporator, 2) condenser, 3) porous

wick, and 4) vapor pathway. The evaporator region is bonded by the thermal interfacial material to lower the thermal resistance between the heat source and heat pipes. Once the liquid is evaporated, the vapor passing through the vapor pathway by the vapor pressure difference at the evaporator region and condenser region. Then, heat is dissipated by condensation at the condenser region. The condensed water is transported back to the evaporator region by the capillary action through the porous wick.
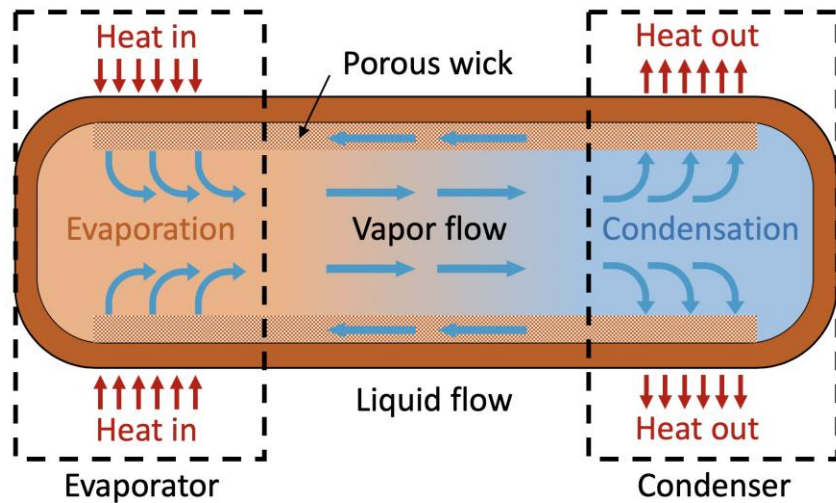
Figure 1.4. Schematic illustration of the typical heat pipes. The heat pipes are composed of four sections: 1) condenser, 2) evaporator, 3) porous wick, and 4) vapor pathway. Heat is dissipated during the phase-change process of working fluid. The working fluid circulates passively by capillary pressure in porous wick.

The operation of the heat pipes is limited by different limits according to the operating temperature. Among the operating limits, the capillary limit is a dominant factor in the typical operating temperature from 50 to 150 °C for the water-based heat pipes. The capillary limit occurs when the capillary pressure becomes less than the sum of other pressure drops as:

$$\Delta P_{cap} \leq \Delta P_l + \Delta P_v + \Delta P_e + \Delta P_c + \Delta P_g \tag{1.1}$$

where ΔP_{cap} is the capillary pressure, ΔP_l is the liquid pressure drop, ΔP_v is the vapor pressure drop, ΔP_e is the pressure drop at evaporator region, ΔP_c is the pressure drop at the condenser region, and ΔP_g is the pressure drop by gravitational acceleration. ΔP_{cap} is governed by the surface tension of the liquid, pore sizes of the wick, and surface wettability as following Young-Laplace equation:

$$\Delta P_{cap} = \frac{2\sigma_l \cos(\theta)}{R_p} \tag{1.2}$$

where σ_l is the surface tension of liquid, θ is the contact angle, and R_p is the pore radius. The effective pore radius is $R_{eff} = R_p/\cos(\theta)$, then the capillary pressure can be written $\Delta P_{cap} = 2\sigma_l/R_{eff}$. Since the pressure drop of ΔP_g, ΔP_v, ΔP_e, and ΔP_c is negligible comparing to the ΔP_l, the capillary limit can be obtained when $\Delta P_{cap} = \Delta P_l$.

The liquid pressure drop through porous media can be explained by Darcy's law:

$$\frac{dP}{dx} = -\frac{\mu_l \dot{m}}{\rho_l A K} \tag{1.3}$$

where μ_l is the dynamic viscosity of liquid, $\dot{m}$ is mass flux of liquid, and ρ_l is the density of liquid, A is the cross-sectional area of the porous media, and K is the permeability. Considering the mass flux is $\dot{m} = \rho_l A v \phi$, where v is the liquid velocity, and ϕ is the porosity of the porous media. Using the equation (1.2) and (1.3), the correlation of the capillary pressure is obtained as:

$$\frac{K}{R_{eff}} = \frac{\mu_l \phi L}{2\sigma_l} \frac{dL}{dt} \tag{1.4}$$

where L is the length of the heat pipes. The integrated form of the equation become following Lucas-Washburn equation:

$$L^2 = \left(\frac{4\sigma_l}{\mu_l \phi}\right)\left(\frac{K}{R_{eff}}\right)t \qquad (1.5)$$

The first part of the righthand equation is the liquid property and the second part of the equation is the capillary performance parameter (K/R_{eff}). In order to compare the wicking through the porous media to the evaporative mass flux, the evaporative mass flux can be determined by $Q = \dot{m}h_{fg}$, where Q is the heat flux, and h_{fg} is the latent heat of the working fluid. Using the equation (1.2) and (1.3), the correlation can be obtained as:

$$\frac{2\sigma_l}{R_{eff}} = \frac{\mu_l L}{\rho A K}\frac{Q}{h_{fg}} \qquad (1.6)$$

Then, we can rearrange the equation 1.6 as following equation:

$$Q = \left(\frac{h_{fh}\rho_l \sigma_l}{\mu_l}\right)\left(\frac{A}{L}\right)\left(\frac{K}{R_{eff}}\right) \qquad (1.7)$$

The first part of the righthand equation is the liquid property of the working fluid known as Merit number, the second part is the dimension of the heat pipes and the third part is the capillary pressure parameter. Therefore, if the dimension of the heat pipes and the working fluid is the same, the capillary performance dictates the heat dissipation performance of the heat pipes. Once the dry-out occurs at the evaporator region, the heat flux through the evaporation reaches to the maximum heat dissipation limit.
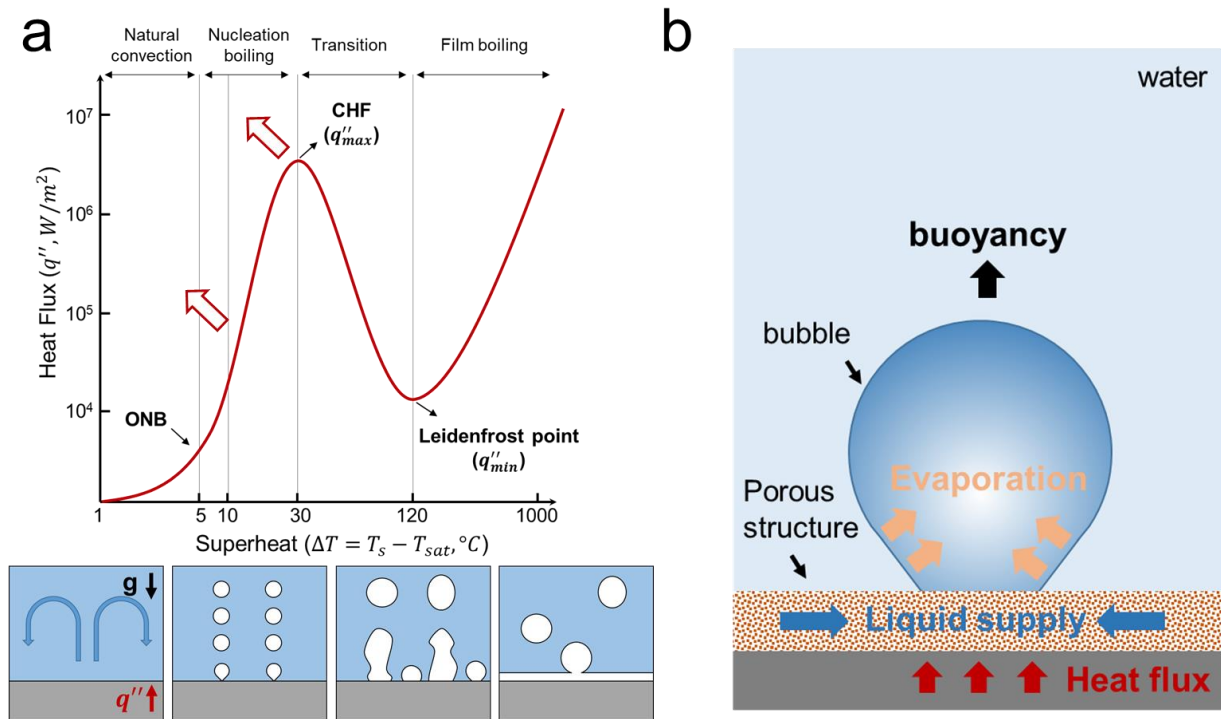
Figure 1.5. Two-phase heat transfer for pool boiling and thin-film evaporation. (a) boiling curve show the pool boiling mode in different superheat condition. (b) The illustration shows bubble dynamics on porous media with capillary-driven liquid transport for replenish of working fluid to heating region.

In the same manner, the continuous liquid supply plays a crucial role in terms of increase in critical heat flux (CHF) and HTC for the boiling or evaporation two-phase heat transfer. Firstly, pool boiling heat transfer has been studied extensively in the past few decades due to its importance in applications such as power generation, immersion cooling, and desalination. Figure 1.5a. shows the typical boiling curve showing four regimes along with the surface superheat ($\Delta T = T_s - T_{sur}$), which is 1) natural convection, 2) nucleation boiling, 3) transition boiling, and 4) film boiling. When the bubble starts to nucleate, the boiling heat transfer rate is rapidly increasing and reaches CHF. In transition boiling, the vapor blanket covers the heating region lowering the thermal conductivity between the surface and the liquid resulting in lowering heat flux once the superheat reaches to Leidenfrost point. Based on the

understanding of the CHF, the enhancement of boiling heat transfer performance can be achieved by preventing transition to film boiling through continuous liquid supply at the heating region.[3–12] Since the bubbles generated from the heating region are removed by the buoyancy, continuous liquid supply to the heating region facilitate bubble departure by supplying vapor to satisfy the buoyant force enough to overcome adhesion force, which lowers the thermal resistance between the surface and liquid (Figure 1.5b).[13]

Secondly, the maximum evaporation rate is also strongly related to the liquid supply that causes dry-out of the heating region.[14,15] The high heat transfer coefficient of the evaporation can be achieved by thin-film evaporation from a meniscus of the liquid.[14] The meniscus can form three regions: 1) absorbed film region, 2) thin-film region and 3) bulk meniscus region. The evaporation heat flux increases in the thin-film region comparing to the bulk meniscus region due to the low thermal resistance of the thin liquid film. When the liquid film is getting thinner to be the absorbed film region, the intermolecular adhesion interaction becomes dominant resulting in no heat dissipation through evaporation. It indicates that the dry-out of the evaporator region causes low heat flux. Therefore, past researches have been studied micro or nanostructured surfaces to increase the thin-film region and to enhance wicking performance.[16–18]

1.3. Surface Wettability and Capillary-Driven Liquid Transport

Enhancement of the two-phase heat transfer has been achieved through the improvement of the fabrication techniques for micro- or nanostructured surfaces owing to its unique properties. The micro- or nanostructured surface could provide enormous surface area and roughness compared to plain surface with the same surface chemistry and wetting

property. For example, previous studies have been explored metal oxide nanostructured surfaces (CuO, ZnO), silicon micropillar arrays, inverse opals structures, and woodpile structures.[19–21] The surface roughness of the structured surfaces provides magnified surface hydrophilicity due to the Wenzel state of wetting mode, and smaller pore sizes allow the structured surfaces to transport liquid with higher capillary pressure.
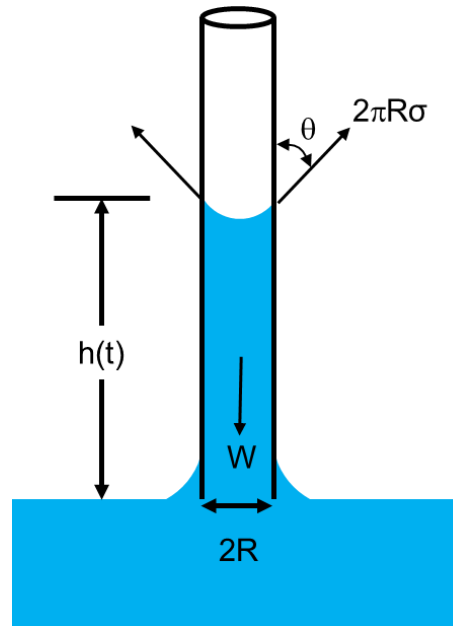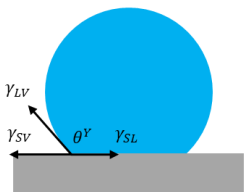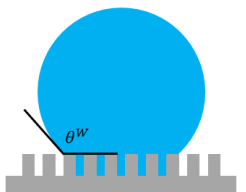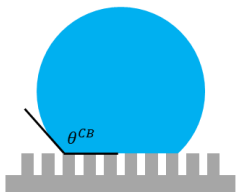
Figure 1.6. Capillary pressure applied in a thin tube between two immiscible liquid. Capillary pressure generated from interfacial tension is a driving force of liquid to move upward against gravity. The capillary pressure increases as pore radius increases and contact angle decreases.

The engineering surface with single length scale morphology or homogeneous structure is facing the liquid transport limit because of the tradeoff between two factors: permeability and capillary pressure. The permeability of the porous media become smaller when the pore size become smaller, while the capillary pressure increases when the pore size decreases (Figure 1.6). The capillary performance through the porous media could be

quantified by the capillary performance parameter K/R_{eff}, where K is the permeability, and R_{eff} is the effective pore radius $R_{eff} = R_p/\cos\theta$.[22–24] Since the decrease in pore sizes both decreases K of the porous media and R_{eff}, the total capillary performance parameter remains constant. Therefore, the hierarchically structured surfaces have been drawn great interest recently. The hierarchically structured surfaces could provide two different length scale morphology or roughness, which enhances permeability and capillary pressure at the same time. The large-scale pore provides the liquid pathway maintaining materials' permeability and nanoscale morphology decreases effective pore radius by decreasing pore size (R_p) or modifying surface wetting property (θ).

The surface wetting property can be explained by three classic theories: the Young-Dupre model, Wenzel model, and Cassie-Baxter model as shown in Figure 1.6. The Young-Dupre model first explains that the droplet contact angle θ on a flat surface is dictated by a force balance at all the three solid-vapor, solid liquid, and liquid-vapor interfaces: $\cos\theta^Y = (\gamma_{SV} - \gamma_{SL})/\gamma_{LV}$, where γ is surface tension. The subscripts SV, SL, and LV represent solid-vapor, solid-liquid, and liquid-vapor, respectively. In order to explain the surface roughness r impacts on the droplet formation, the Wenzel equation shows that contact angle on rough surfaces is defined by[25]: $\cos\theta^W = r\cos\theta^Y$, where r is the roughness that is the ratio of the total surface area to the projected area. This explains that hydrophobic surfaces become more hydrophobic or hydrophilic surfaces become more hydrophilic as the surface roughness increases. Once the Wenzel droplet is placed on a rough surface, it will completely wet the surface, resulting in the "Wenzel droplets". Considering the case where the droplet rests on the tip of nanostructures, the Cassie-Baxter theory introduces air gap between droplets and the rough surface[26]: $\cos\theta^{CB} = \phi_s(cos\theta^Y + 1) - 1$, where ϕ_s is a solid

fraction. The trapped air underneath the liquid-vapor interface helps droplets be suspended from the substrate, leading to "Cassie-Baxter droplets". The superscripts Y, W, and CB represent Young-Dupre, Wenzel, and Cassie-Baxter, respectively.

Wetting mode	Wetting on smooth surface	Wenzel	Cassie-Baxter
Surface	Plain surface	Rough surface	Rough surface
Governing equation	$\cos\theta = \dfrac{\gamma_{SV} - \gamma_{SL}}{\gamma_{LV}}$	$\cos\theta^W = r \times \cos\theta^Y$	$\cos\theta^{CB} = \phi_s(\cos\theta^Y + 1) - 1$

Figure 1.7. Schematic illustrations of surface wetting. The illustrations depict wetting modes on the smooth surface and roughened surface.

Based on the understanding of surface roughness on the wetting property, two factors should be considered to design the porous media for the capillary wick. First, surface roughness magnifies intrinsic wettability of the surface. For example, rough surfaces with hydrophilic property become more hydrophilic than plain surfaces based on Wenzel equation (Figure 1.7). Second, the wetting state should be the Wenzel state instead of the Cassie-Baxter state for the capillary-driven liquid transport. The wettability requirement for transition from Wenzel state to Cassie-Baxter state can be calculated by the critical contact angle. The critical contact angle of the roughened structures shows the minimum requirement of static contact angle of the material allowing capillary action. Therefore, the static contact angle θ_s of the materials' surface should be lower than the critical contact angle θ_c to be favorable for wicking where the θ_c can be calculated by the following equation:

$$\theta_c = \cos^{-1}\left(\frac{1-\varepsilon}{r-\varepsilon}\right) \tag{1.8}$$

where roughness r is the ratio of the projected surface area and the actual surface area, and ε is the solid fraction of the porous media.

Past research has studied the hierarchically structured surfaces for efficient wicking and enhanced HTC and CHF. Yao *et al.* studied the hydrophilic silicon nanowire incorporated microgroove achieving 120% enhancement of CHF comparing to the microgroove.[27] The hierarchically structured microgroove provides a large liquid pathway by the groove and more surface area with the nanowires. Chu *et al.* report the large enhancement in CHF on hierarchically structured Cu microposts.[28] They highlight the importance of the roughness with the multiple length scales for CHF enhancement. Recently, the enhanced bubble nucleation is studied using hierarchical surfaces with patterned copper nanowire arrays without surface treatment.[6] The nanowire arrays are patterned through the photolithography and prepared by templated electrodeposition method. The patterned hierarchical nanowire arrays achieve 71% of CHF enhancement and 185% of HTC enhancement by enhanced wicking of nanowires and improved nucleation site from microcavities. The hierarchically structured surfaces improve the wicking performance by additional roughness or wettability modification from the lower-level hierarchy, and also provide additional liquid pathways and cavities for bubble nucleation from the upper-level hierarchy.

1.4. Outline of Doctoral Research

This work aims to explore the liquid transport in the hierarchically surfaces and reveal the thermo-fluid dynamics in boiling two-phase heat transfer. Recently, the advancement of the fabrication method of micro- nanostructured surfaces enables the preparation of novel types of engineering surfaces *via* colloidal crystal template, wettability optimization, chemical oxidation, templated electrodeposition, and sintering processes. In this dissertation, we utilize those fabrication techniques to understand liquid transport behavior along with surface wettability and morphological characterization, which includes the role of microscale permeability in presence of nanoscale features, heterogeneous surface properties, and the role of nanoscale surface characteristics. To demonstrate the liquid transport behavior on the hierarchical surfaces, the experimental fabrication, and computational calculation are both utilized in this dissertation.

In Chapter 2, liquid transport in hierarchical engineering surfaces is demonstrated by using vertically aligned nanowires decorated with copper oxide nanofeatures. The permeability of nanowires is modulated by increasing hydraulic diameter with uniform porosity nanoscale feature size. We investigate the liquid spreading and infiltration behavior on the hierarchical nanowires with nanoscale features. Chapter 3 provides an understanding of liquid transport in hierarchical nanowires with heterogeneous properties such as surface wettability and morphology. In addition, the role of the heterogeneous properties on boiling two-phase heat transfer is demonstrated by investigating the bubble dynamics and heat flux. In Chapter 4, the liquid transport in three-dimensional hierarchical porous media is presented by using bijel-templated scaffolds. The bijel-templated scaffolds offer superior liquid permeability owing to low tortuosity, connectivity, and uniform domain size along

with future opportunities to control over domain size. We control lower hierarchy independently to demonstrate the effect of hierarchical structures on liquid infiltration and droplet imbibition process. Chapter 5 provides concluding remarks on the liquid transport in hierarchically structured surfaces for two-phase heat transfer and their potential for future research advancement.

CHAPTER 2: Capillary-Driven Liquid Transport in Hierarchically Textured Nanowires

Capillary wicking through homogeneous porous media remains challenging to simultaneously optimize due to the unique transport phenomena that occur at different length scales. This challenge may be overcome by introducing hierarchical porous media, which combine tailored morphologies across multiple length scales to design for the individual transport mechanisms. Here, we fabricate hierarchical nanowire arrays consisting of vertically-aligned copper nanowires (~100-1000 nm length scale) decorated with dense copper oxide nanostructures (~10-100 nm length scale) to create unique property sets that include a large specific surface area, high rates of fluid delivery, and the structural flexibility of vertical arrays. These hierarchical nanowire arrays possess enhanced capillary wicking (K/R_{eff} = 0.004-0.023 μm) by utilizing hemi-spreading and are advantageous as evaporation surfaces. The degree of effective inter-nanowire pore and porosity is shown to govern the capillary performance parameters, thereby this study provides the design strategy for capillary wicking materials with unique and tailored combinations of thermofluidic properties.

2.1. Background

Passive liquid delivery using porous media has been challenging because there are tradeoffs between different transport mechanisms that favor different length scales. For example, capillary-pumped liquid transport within porous materials favors small length scales but competes with viscous resistance attributed to constriction in the small pores.[29] Such competition may be mitigated using hierarchical porous morphologies that contain multiple length scales to simultaneously optimize around the length scales associated with each individual transport phenomenon. The ability to wick fluid through hierarchical porous materials pushes toward the fundamental mass transport limits in porous media by providing additional capillary pressure through small pores and by minimizing hydraulic resistances through large pores. However, materials used in past studies have been restricted to homogeneous porous media with a narrow distribution of length scales primarily due to fabrication capabilities.

Most of previous porous media used (e.g., sintered copper particles,[22,23,30–34] randomly oriented silicon nanowires,[35–37] and zinc oxide nanoporous layer[38]) have possessed random morphologies that exhibit a single set of properties with large deviations across their entire structures. Other microfabricated structures (e.g., silicon pillars) contain highly ordered microscale features.[39] However, such traditional microfabricated structures exhibit limitations in modulation of three-dimensional features or surface modifications, which makes it difficult to finely engineer hierarchical silicon structures. More recent approaches – nanofabrication techniques through templating – now can design hierarchically, textured pore morphology to be tuned through surface modification or oxidation. The surface textures can benefit transport applications by providing large fluid-

accessible surface areas and by modulating surface wettability simultaneously.[40–49] For example, our previous study for the wicking capability of hierarchical copper inverse opals has improved hydraulic transport capability, indicating a strong dependence on the effective pore size[50–55] and porosity.[21] Recent advances in wearable or flexible devices[56] have inspired the new porous media to be used in flexible thermofluidic systems. Examples of hierarchically designed wicks (e.g., hierarchical silicon microstructure,[57–59] zinc oxide nanowires,[60] or copper posts[50]) showed the potential to improve the capillary wicking by employing multiple length scales but they cannot be applied to flexible applications. Previous porous wicks tested on curved surfaces consist of either porous metals that cannot return to their original state after deformation due to the structural rigidity or porous polymers that do not provide sufficient thermal conductivity (< 1 W/m·K).[61] Therefore, the remaining challenge is to address the demands for the hierarchically designed, flexible porous metals that can still enable a capillary flow.

Hierarchically textured, vertically aligned arrays of copper nanowires may provide the unique characteristics for thermofluidic applications including effective thermal conductivity up to 70 W/m·K[62,63] and additional structural flexibility that is potentially possible through the combination of large inter-nanowire pores and a large aspect ratio of nanowire height to diameter. Such characteristics of hierarchical nanowires might make them ideal for flexible electronics applications. However, there have been no efforts to report the characteristics of hierarchically designed nanowires in past. Thus, a systematic study is required to fully understand the factors that impact the wicking capability of hierarchical nanowires. Specifically, it is essential to investigate how controlled morphologies of nanowires at the nanoscale can engineer thermofluidic properties of nanowires at the

macroscale. Understanding the thermofluidic properties of hierarchical nanowires on the flat or freestanding substrates is crucial to fully exploit the potential of hierarchical nanostructures for modern thermofluidic applications, such as microfluidic channels, flexible coolers, and heat pipes.[64]

We demonstrate hierarchical nanowires that contain a high density of sharp nanoscale features, through (1) templating pore membranes (~100-1000 nm length scale) via electrodeposition and (2) following surface modification using chemical solutions. Implementing sharp nanoscale features (~10-100 nm length scale) suggests the nanostructured surfaces to be hydrophilic. Furthermore, the combination of two length scales improves the overall capillary performance parameters, defined as the ratio of permeability to effective pore size, enabling the hemi-spreading phenomena. Therefore, we measure the capillary performance parameters of flat and curved hierarchical nanowire arrays by combining experimental and computational techniques. The capillary performance parameters of freestanding nanowire arrays on curved substrates show the potential to be used in flexible wicking applications. The computational models explain the role of effective pore diameter and porosity in determining the thermofluidic performances of hierarchical porous media.

2.2. Experimental Method

2.2.1. Fabrication and Surface Modification

A polycarbonate track etched membrane is laminated onto a metallized silicon surface (5/50 nm Ti/Au), and copper is electrodeposited into the pores to form the nanowires. The exposed deposition area is a 9 mm x 9 mm square created by patterning the Ti/Au evaporation with a shadow mask, and the electrolyte is further confined by an equally sized aperture in the electrochemical cell. We modify the deposition process by applying a constant voltage of V = -320 mV (Ag/AgCl) for 15 min. The nanowires are released by dissolving process of the polycarbonate template in dichloromethane (Sigma Aldrich, > 99%) for 1.5 hr at room temperature. The nanowire diameter is controlled by the membrane's pore size during the copper deposition process. In order to prepare hierarchically textured nanowires, the as-fabricated Cu nanowires are immersed in acetone, deionized water (DI water), and isopropanol for 30 sec each, and then rinsed with 2M HCl (Sigma Aldrich, $\geq$ 37%) for 5 min to remove native copper oxides layer. The copper nanowires are oxidized using the preheated alkaline solution at 70°C that is composed of a 1.7M $NaClO_2$ (Sigma Aldrich, $\geq$ 99%) and a 0.25M NaOH (Sigma Aldrich, $\geq$ 98% pellet) for 2 min. In addition, commercial copper substrates (110 copper sheet, 99.9% pure, McMaster-Carr) are employed to prepare CuO planar substrates by using the same cleaning and oxidation steps.

2.2.2. Surface Characterization and Wetting Property

Surface morphology of the nanowires and nanocactuses is captured using FEI Magellan 400 SEM at a 15 kV of accelerating voltage. For the cross-sectional images, the

sample is cleaved and mounted on the vertical sample holder. The transmission electron microscope study is conducted using JEM-2800 TEM. The nanocactuses are dispersed in acetone using a sonicator. The prepared sample solution is coated on a TEM grid and dried in vacuum chamber. Also, the chemical composition of the sample surface is investigated by XRD (Rigaku SmartLab) with Cu Kα radiation source where the scan rate of XRD measurement is 2°/min ranging from 30° to 80°. In addition, the depth profiling of the copper oxide layer is conducted using gas cluster ion source (GCIS) system equipped in the XPS (Kratos AXIS-SUPRA). The Ar ion beam allows us to investigate the chemical composition such as Cu or CuO.

Contact angles of the samples are measured using the sessile droplet method with a goniometer (MCA-3, Kyowa Interface Sciences) to validate the wicking capability of nanostructures. The goniometer dispenses a 15 nL of deionized water at room temperature on the substrate by minimizing the gravity effect. A high-speed camera captures the droplet dynamics at 5,000 fps, which allows us to quantify the contact angle, as a measure of surface tension using the half-angle method. The static contact angle reported values are averaged over 5 individual measurements for different sample locations, and the error bars represent the standard deviation of individual measurements.

2.2.3. Liquid Rate-of-rise Test

A 3 mm × 9 mm sample containing CuO nanocactuses is mounted on a sample stage in the water reservoir (where $\sigma = 7.197 \times 10^{-2}$ N/m and $\mu = 8.89 \times 10^{-4}$ Pa·s). The liquid reservoir in the chamber is covered by the parafilm to create a saturated vapor condition to

minimize the wicking fluids' evaporation. We measure the liquid-rise-height from the meniscus until the wicking front reaches maximum height. Due to the meniscus on the interface and the portion of the sample below the water level, the measurable height is limited to 8 mm. The average wicking heights are recorded at three locations: x = 0.5 mm, 1.5 mm, and 2.5 mm.

2.2.4 Computational Fluid Dynamics Computation

To prove the importance of the morphological details of nanowires on the overall capillary performance parameters, we develop computational fluid dynamics (CFD) models. Herein, we create a unit cell model consisting of hexagonally packed nanowires with smooth surfaces for the set of porosities (ϕ = 25%, 37%, and 72%), diameters (d = 0.4 μm to 3 μm), and height (h_{NW} = 30 μm) to represent the nanocactuses fabricated in this study by imposing corresponding surface energy values. The static liquid shapes in the nanowire arrays are first predicted based on surface energy minimization algorithms by utilizing Surface Evolver and are imported to ANSYS Fluent for CFD calculations. The average pressure difference computed between the inlet and outlet is used to calculate the permeability K by using the Darcy's law $Q = \frac{(KA)\Delta P}{\mu L_{unit}}$ where K is the permeability, A is the cross-sectional area of the formation, μ is the viscosity of the fluid, Q is the flowrate, ΔP is the pressure gradient, and L_{unit} is the traveling length of the system.
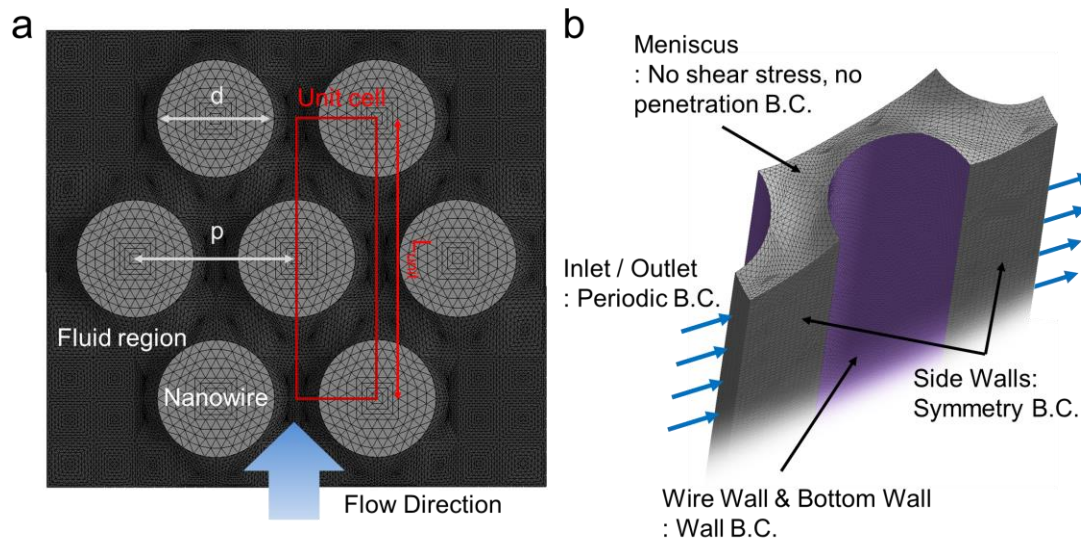
Figure 2.1. Unit cell and boundary conditions used for CFD simulation. (a) Schematic illustration of the hexagonally aligned nanowires and (b) boundary conditions for the numerical simulation.

The static liquid free surface shapes in the nanowire structures are first predicted based on surface energy minimization algorithms by utilizing Surface Evolver. The estimated meniscus shape is post-processed with a commercial CAD design package and imported to ANSYS Fluent for computer fluid dynamics (CFD) calculations. Figure 2.1 show the unit cell and the boundary conditions for the fluidic unit cell, where p is the distance between the center of the nanowires, and d is the nanowire diameter. We apply periodic pressure boundary conditions to ensure that the velocity profile is equal at the inlet and outlet. In this paper, we assume that the shear stress on the liquid meniscus is negligible because the viscosity of air is considerably smaller than that of water. A symmetry boundary condition is applied to the side walls. The simulation models employ SIMPLE scheme for pressure linked equations, PRESTO! Scheme for pressure discretization, and least square cell-based formulation for gradient spatial discretization.

2.3. Results and Discussion

2.3.1. Preparation of Nanowires and Surface Modification

We first prepare smooth copper nanowire arrays by electrodeposition into sacrificial porous membrane templates,[65–68] as illustrated in Figure 2.2a-c (see experimental section for the details). The template of the pore membrane with different nominal pore diameters of 200 nm, 400 nm, and 1000 nm directly sets the nanowire diameters, which hereafter will be referred to as NW1, NW2, and NW3, respectively. This templating method can be scalable and cost-effective, also it enables one-to-one morphology by using a predefined template. The complete fabrication protocol can be found in the previous references.[64,69] Then, we texture the nanowire surfaces using an aggressive oxidization treatment (Figure 2.2d) that enables the fast demonstration of nanofeatures with relatively low energy requirements. After the oxidization, the nanowire surface is found to contain a high density of sharp nanoscale features (Figure 2.2e-g) referred to as "CuO nanocactuses" (or CuO@Cu nanowires) where the as-fabricated nanowires are cylindrical with smooth surfaces (Figure 2.2c). The corresponding nanocactus diameter (see Table 2.1) increases with additional oxide nanofeatures compared to the initial nanowires (Figure 2.3a-c), as indicated in corresponding SEM images of nanocactuses (Figure 2.3d-i). The average diameter of the CuO nanocactuses is determined by measuring multiple nanowires and by further considering the angle-dependent radius of individual nanocactuses in order to account for the creation of oxide nanofeatures. The morphological details are described by scanning electron microscope (SEM) and transmission electron microscope (TEM) images in Figure 2.2f-g. The chemical compositions of the nanowires and nanocactuses are characterized by using X-ray diffraction (XRD) and ion-etching X-ray photoelectron

spectroscopy (XPS). This characterization confirms that cuprous oxide (Cu_2O) forms on the Cu surface first, and then cupric oxide (CuO) forms in series.
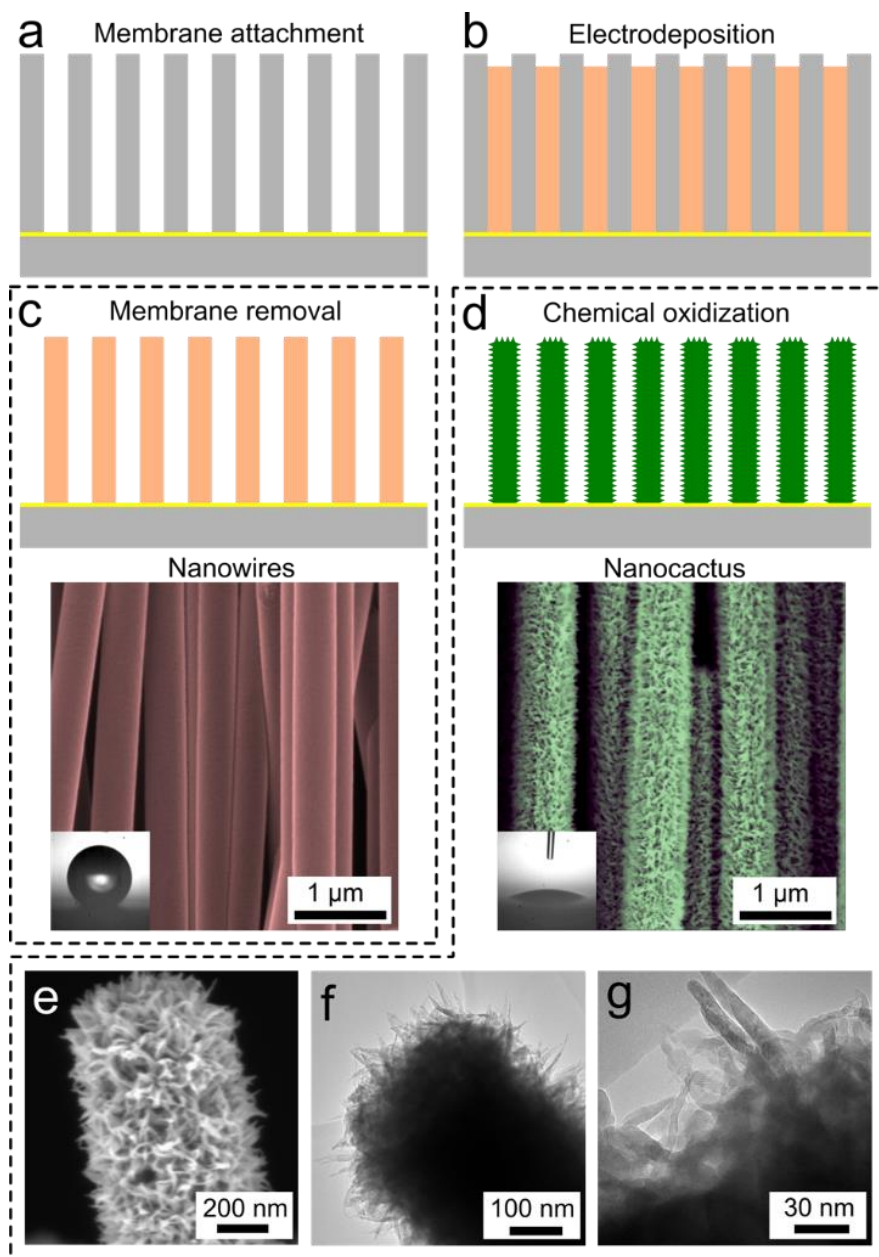
Figure 2.2. Details of Cu nanowires and hierarchically textured nanowires ("CuO nanocactuses" or "CuO@Cu nanowires"). Schematic diagrams in (a-d) show the fabrication process of the Cu nanowires and CuO nanocactuses. The porous membrane in (a) is used as a sacrificial template to confine the copper deposition in (b). (c) The removal of

the sacrificial template leaves behind nanowire arrays. Scanning electron microscope (SEM) image shows Cu nanowires and inset image confirms the hydrophobicity of Cu nanowires. (d) Nanowire arrays are further oxidized with an alkaline solution, resulting in the hierarchical morphology. SEM image shows CuO nanocactuses and inset image shows the hydrophilicity of CuO nanocactuses. € Scanning electron and (f-g) transmission electron microscope images indicate a high density of sharp nanoscale features around the individual nanocactus.
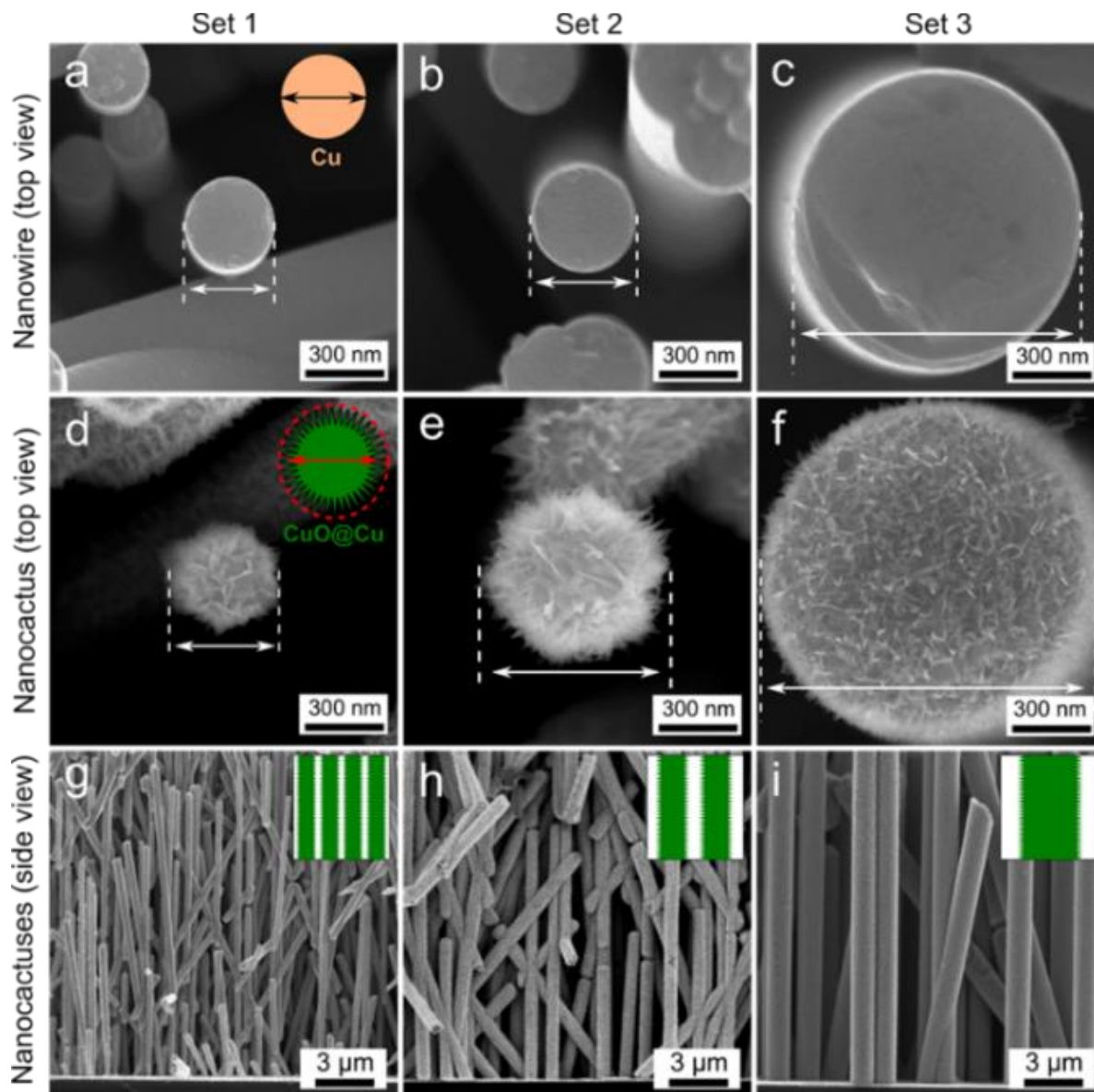
Figure 2.3. Top and cross-sectional SEM images. The SEM images show (a-c) Cu nanowires and (d-i) CuO nanocactuses for varying diameters. The surface oxidization forms a high density of sharp nanoscale features, resulting in the 16% - 45% increase in the nanowire diameter. Inset illustrations in (a and d) show an individual nanowire before and

after surface oxidization. (g-i) Cross-sectional SEM images clearly indicate the inter-nanowire spaces between adjacent CuO nanocactuses. Note that some CuO nanocactuses are damaged during the cleaving process. Inset illustrations delineate CuO nanocactuses with varying diameter and pitch.

2.3.2. Nanowires Morphological Details

The installation of nanoscale features on nanowire surfaces affects the overall porosity. The apparent porosity in this work is defined as the void fraction of the material system $\phi = 1 - \varepsilon$, where ε is the solid fraction that is occupied by nanowires. Thereby, the initial solid fraction is calculated by $\varepsilon = \pi d^2 N/4$, where d is nanowire diameter and N is the areal number density of nanowires. Then, the solid fraction is further modified in order to account for the level of nanowires' disorder, represented by nanowire-nanowire contacts due to their entanglements or zipping. This disorderness is quantified by investigating the detailed statistical distribution of nanowire arrays through top view SEM images shown in Figure 2.5a-c. The SEM images are converted to black and white images by using commercial software ImageJ to clearly identify nanowire tips and their contacts between adjacent nanowires, as shown in Figure 2.6a-c insets. The contacts result in the decrease in the overall solid fraction by 2.7%, 5.4%, and 0.2% for each set of nanowire arrays (Figure 2.4), which is considered to be relatively small. The overall porosity of the Cu nanowires is $\phi \sim 79\%$, whereas that of the CuO nanocactuses ranges from 50% to 60%, as shown in Figure 2.6d. The significant decrease in the porosity is caused by the creation of nanoscale features arounds the surface. Since the oxide surface is not fully dense, the porosity is calculated by considering nanostructures' profile along the surfaces (Figure 2.5).

27

	NW1	NW2	NW3
Portion of NW in contact	0.41	0.49	0.16
Areal lost due to NW in contact	0.066	0.11	0.013
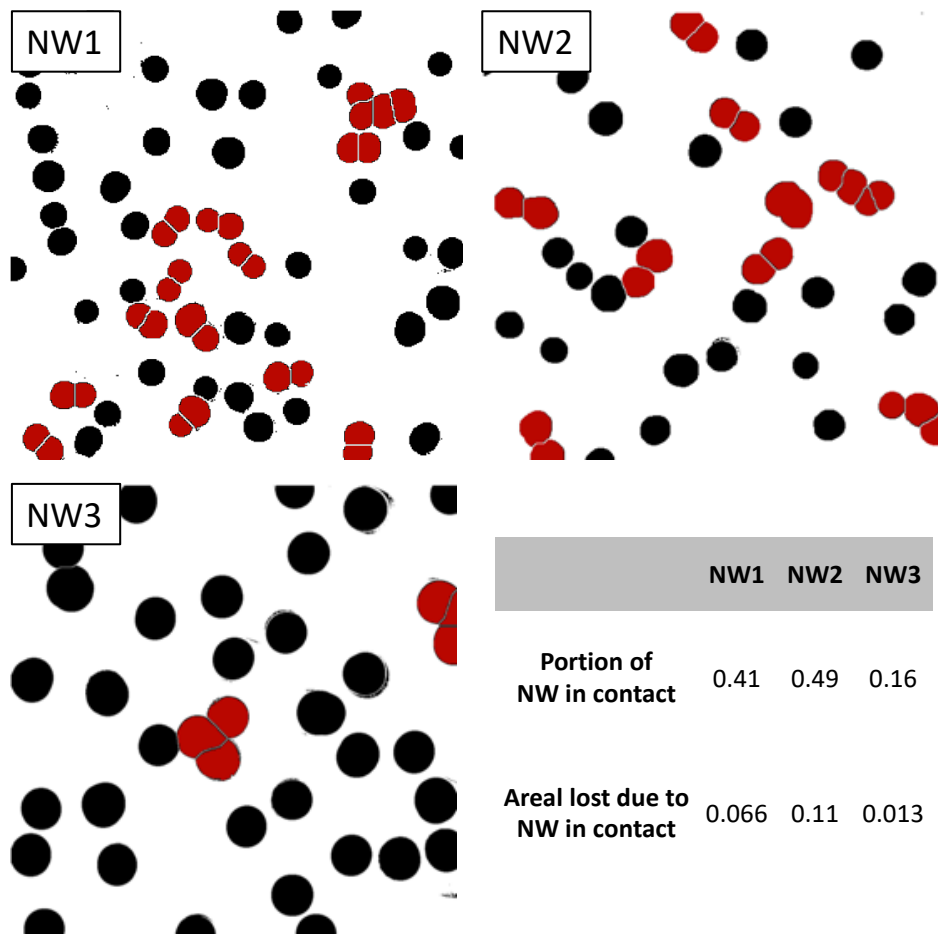
Figure 2.4. Post-processed SEM images showing nanowire tips in contact. Each dot represents the nanowire tip, which allows us to identify the nanowires in contact (red dots) and calculate the areal lost due to the contacts. The areal lost for each set is 2.7%, 5.4%, and 0.2% for NW1, NW2, and NW3, respectively.
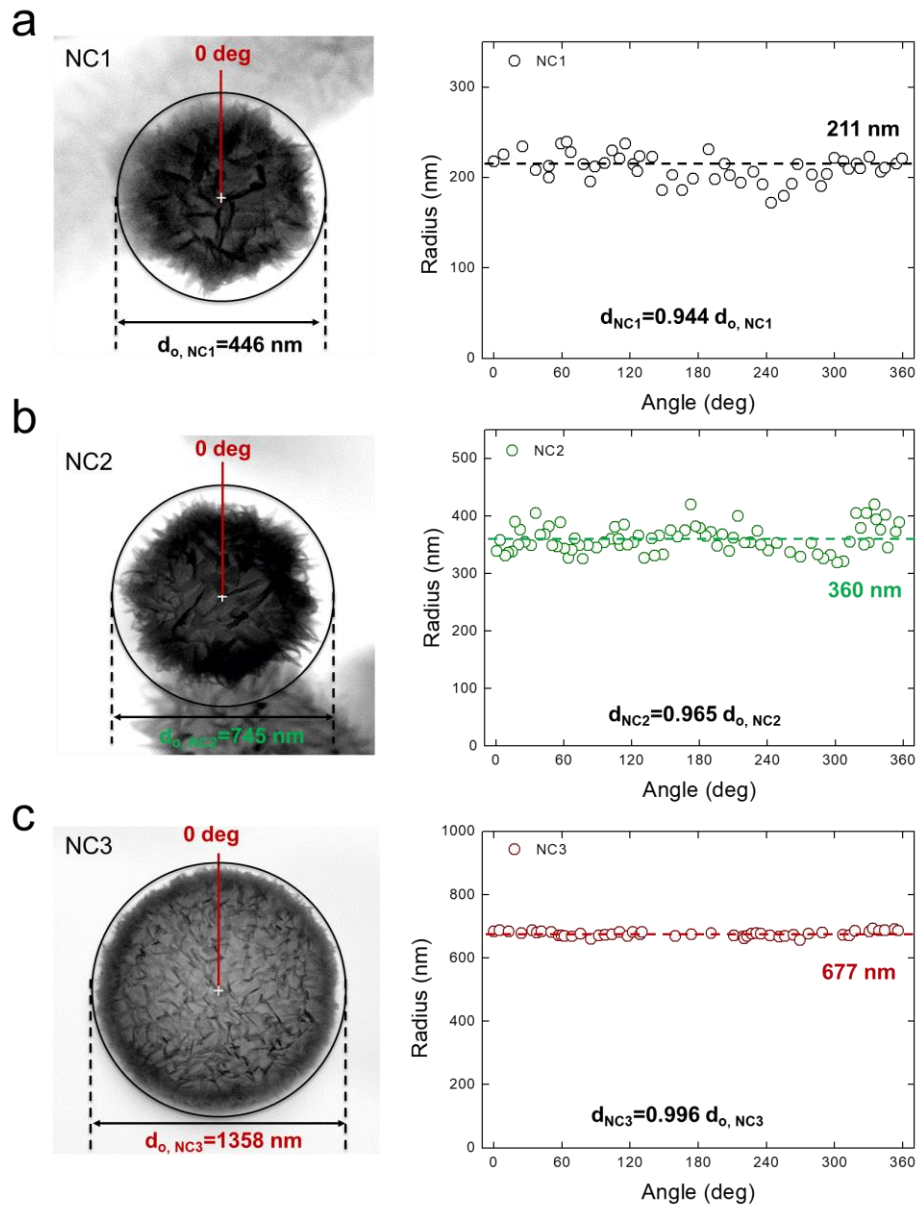
Figure 2.5. SEM images and plots showing the diameter analysis of an individual nanowire after oxidization. The SEMs show the outer diameter d_o of an individual nanowire from (a) NC1, (b) NC2, and (c) NC3. Then, the apparent diameter is analyzed by measuring the angle-dependent radius, allowing us to calculate the average diameter as well as overall porosity. The average diameter can be expressed as $d = Ad_o$, where the coefficients A are 0.944, 0.965, and 0.996 for NC1, NC2, and NC3, respectively.

As a next step, we measure the pitches between an individual nanowire and its neighboring nanowires by using top view images. The nanowire pitch distribution for each

29

set is displayed in Figure 2.6e-g, where the averaged pitch is calculated as 675 nm, 853 nm, and 2198 nm for NW1, NW2, and NW3, respectively. Then, the nanowire pitch distributions are compared with the nanowire pitch calculated by using a simplified, hexagonally packed nanowire model following this expression: $p_{hex} = \left(2/\sqrt{3}N\right)^{1/2}$. The comparison between the two approaches calculating pitches shows the difference of 2%-6%. This comparison thereby suggests that the hexagonal packing model assumption is valid and can be further employed to understand the relations between nanowire morphological details and their capillary wicking performances in the theory section.
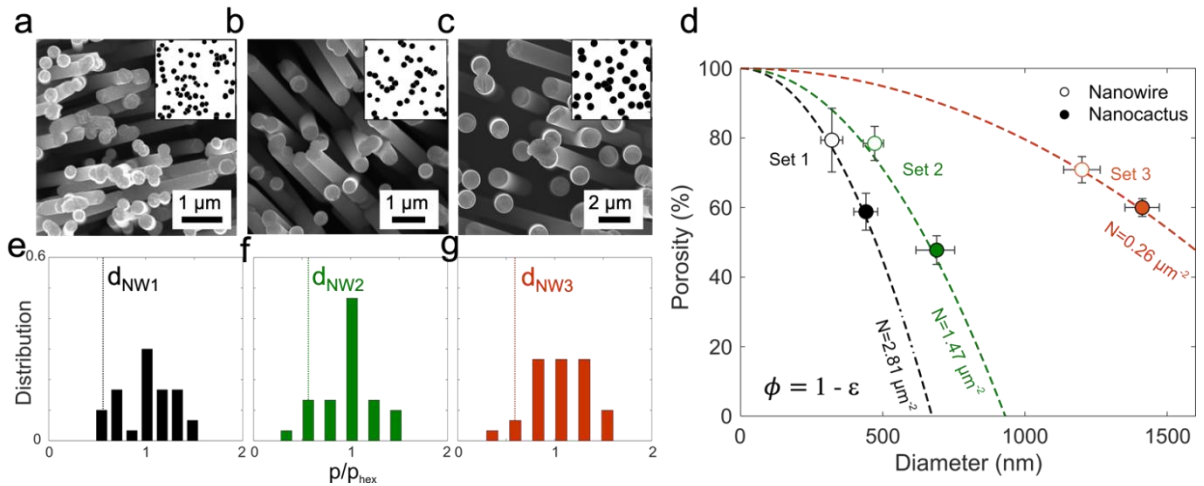
Figure 2.6. The quantification of the overall porosity and pitch distribution of nanowires. Top view SEM images show the level of disorders of (a) NW1, (b) NW2, and (c) NW3. (d) The apparent porosity, the void fraction of the material system, is calculated based on the nanowires' morphological details, indicating a significant decrease in the porosity after surface oxidization. The dashed lines represent the porosity prediction of each nanowire number density corresponding to the nanowire diameter. The error bars represent uncertainty in the diameter and the porosity. The pitch distributions of € NW1, (f) NW2, and (g) NW3 are plotted for the normalized pitches p/p_{hex}, indicating small deviations between two approaches. The pitches smaller than the corresponding nanowire diameter (dotted line) are attributed to the presence of nanowire-nanowire contacts.

2.3.3. Wetting Property of Nanowires and Nanocactuses

Hierarchically textured, aligned nanowires enhance capillary wicking by enabling a liquid pathway through the relatively large inter-nanowire pores while the capillary pressure is retained through the comparatively small features of the textured surface. We elucidate the droplet dynamics by using a sessile droplet method to understand the nanostructures' role in the capillary wicking related to the morphological information (Figure 2.8a-b). In this process, we measure the contact angle, the angle at which the liquid–vapor interface meets the solid-liquid interface as a function of time. Then, the liquid front of nanocactuses propagates to minimize the surface energy beyond the droplets, thereby a liquid film wicks through the hierarchical structure (Figure 2.7). This phenomenon is called hemi-spreading[64,69] (Figure 2.8b) and can be explained by the transition from the Wenzel state to the surface film state due to a small intrinsic contact angle between the nanostructured solid and liquid interfaces.[70,71] As a result, the droplet shows a rapid decrease in the contact angle θ_{NC} down to 5-10° within 5 ms and is completely absorbed through the nanocactuses within 10 ms in Figure 2.8c, whereas as-fabricated Cu nanowires show a consistent hydrophobicity (θ_{NW} > 145°) independently of the nanowires' diameter in Figure 2.8d. The wettability of the sharp nanofeatures can be estimated by measuring the dynamic contact angle of the CuO planar substrate θ_{CuO} (Figure 2.8b). The contact angle of 53° at 2000 ms serves as a reference that represents the nanostructures' static contact angle θ_s to be used to calculate effective pore size. This static contact angle is always smaller than the critical contact angle θ_c, suggesting the hemi-spreading of hierarchical nanowires:

$$\theta_c = \cos^{-1}\left(\frac{1-\varepsilon}{r-\varepsilon}\right) \tag{2.1}$$

The roughness r, the ratio of the actual surface area to the projected surface area, can be expressed as $r = 1 + 2\pi d h_{NW}/\sqrt{3}p^2$, where h_{NW} is the height of the nanowires. Thereby, the roughness increases proportionally to the nanowire diameter. The resulting critical contact angles are plotted as a function of the nanowire diameter in Figure 2.7b and show the saturated values for $d > 200$ nm due to the large surface roughness resulted from the large aspect ratio of nanowire height to nanowire diameter (> 25). The comparison between measured static contact angles and calculated critical contact angles confirms that the surface oxidization makes CuO nanocactuses hydrophilic to enhance the capillary performance. The detailed information of the geometry and wettability is listed in the Table 2.1.
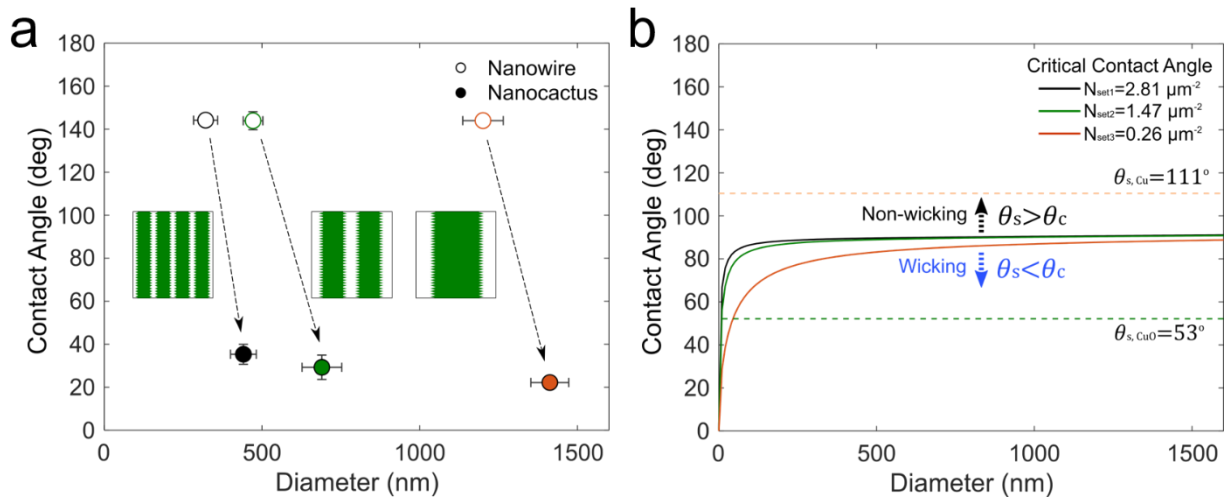
Figure 2.7. Contact angle and theoretical calculation of critical contact angle of the nanowire arrays for each number density. (a) Contact angle measurements show that hydrophobic Cu nanowires become hydrophilic CuO nanocactuses after surface texturing and oxidation. The error bars indicate the standard deviation of diameter and contact angle. (b) The critical contact angle shows a potential of the nanocactuses for wicking. Once the static contact angle is lower than critical contact angle, the porous surface favors capillary wicking. The critical contact angle plot is calculated based on the roughness. The static contact angles of Cu substrate and CuO textured substrate are 111° and 53°, respectively.

Table 2.1. Summary of the sample information and surface properties.

Sample set	Nominal pore diameter (nm)	Sample name	Diameter (d, nm)	Pitch (p_{avg}, nm)	Porosity (ϕ)	Initial contact angle (°)
Set 1	200	NW1	320 ± 40		0.79 ± 0.09	144 ± 1
				680 ± 160		
		NC1	440 ± 40		0.58 ± 0.05	35 ± 5
Set 2	400	NW2	470 ± 30		0.78 ± 0.05	144 ± 4
				850 ± 160		
		NC2	690 ± 60		0.47 ± 0.04	29 ± 6
Set 3	1000	NW3	1200 ± 60		0.70 ± 0.04	144 ± 3
				2200 ± 610		
		NC3	1400 ± 60		0.59 ± 0.03	22 ± 2

We further compare the contact angles of Cu or CuO planar substrates, Cu nanowires, and CuO nanocactuses by identifying $\theta_{\tau=0.5}$ in Figure 2.8e. The contact angles $\theta_{\tau=0.5}$ are recorded at $\tau = 0.5$, where the time is normalized by the total time required to get stabilized to account for the dynamic features of the contact angles. This analysis allows us to understand the impact of oxide features on wettability by comparing Cu and CuO planar substrates or Cu and CuO nanowires. Also, it further confirms that the creation of hierarchy via surface modification decreases the contact angle of CuO nanocactuses down to 15° compared to CuO planar substrate. Thereby, the combination of the intrinsic hydrophilicity of CuO and hierarchical structures provides the hydrophilicity of CuO nanocactuses, enabling capillary wicking performances.
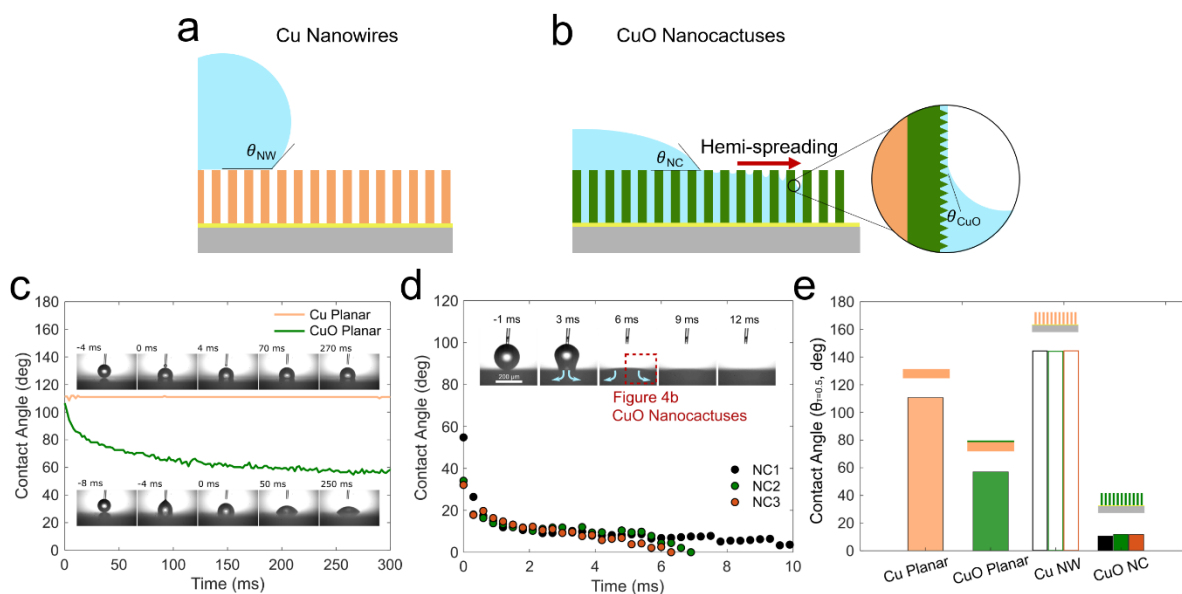
Figure 2.8. Surface properties of Cu nanowires and CuO nanocactuses. (a, b) Illustrations show that the water droplet on CuO nanocactuses begins to spread out with the liquid front propagating beyond the textured surface by hemi-spreading, while the water droplet on nanowires is static. € The time-dependent contact angles and captures (inset) on the Cu and CuO planar substrates confirm the nanotextures' effect on wettability. The droplet on the CuO planar plate decreases to 53° within 250 ms. (d) The time-dependent contact angles and captures (inset) on nanocactuses (NC1, NC2, and NC3) show the hemi-spreading through hierarchical nanocactuses. € Contact angles at $\tau = 0.5$ are plotted for the Cu or CuO planar substrates, Cu nanowires, and CuO nanocactuses, which confirms the effects of surface oxidation and morphological change on their dynamic wettability.

2.3.4. Capillary Performance Parameters of Nanocactuses

We examine the capillary performance parameters of CuO nanocactuses by conducting capillary rate-of-rise experiments. Once the sample's bottom line touches the water surface, a meniscus is formed, and the meniscus front propagates through hydrophilic nanotextures in order to minimize the surface energy. The differences in initial meniscus shapes for the Cu nanowires (Figure 2.9a) and CuO nanocactuses (Figure 2.9b) clearly show the capillary performance enhancement through the surface modification. In this process,

34

the capillary rise of the liquids through the porous wick is determined by the surface tension of the liquid and interfacial interaction between liquid-vapor, expressed with the Laplace-Young equation. The capillary pressure equation can present the Lucas-Washburn correlation.[72,73] The capillary pressure through the porous media is dictated by the surface tension of the liquid and interfacial interaction between liquid-vapor. The relation of the capillary pressure P_{cap} can be expressed with the Laplace-Young equation (equation 1.5) where σ is the surface tension of the liquid, and R_p is the static pore radius. During the wicking process, the capillary pressure should be equal to the summation of the viscous friction, gravity, and evaporation for momentum balance as given by:

$$\frac{2\sigma cos\theta_s}{R_p} = \frac{\phi}{K}\mu h v + \frac{\dot{m}_{evp}\mu}{2d_{film}\rho K}h^2 + \rho g h \tag{2.2}$$

where K is permeability, μ is the liquid viscosity, d_{film} is film thickness, and ρ is the liquid density. The mass evaporation rate $\dot{m}_{evp}$ is assumed to be zero in the vapor saturation condition in the chamber. The gravitational term including the gravitational acceleration g is negligible in the condition of such a low wicking height (< 10 mm) at the permeability over 1×10^{-20} m² (Figure 2.10). Therefore, the equation 2.2 can be reduced to the Lucas-Washburn equation[3,4]:

$$h^2 = \frac{4\sigma}{\phi\mu}\frac{K}{R_{eff}}t \tag{2.3}$$

where R_{eff} is the effective radius $R_{eff} = R_p/\cos\theta_s$. The eq (2.3) can be simplified to $h^2 = Dt$, with the coefficient $D = 4\sigma K/\phi\mu R_{eff}$. Therefore, we measure the capillary performance parameters of three sets of the CuO nanocactuses. The wicking height h is plotted against $t^{1/2}$,

allowing us to calculate D_{NC1} = 2.01×10^{-6}, D_{NC2} = 5.77×10^{-6}, and D_{NC3} = 1.13×10^{-5} m^2/s based on eq (2.3) in Figure 2.11a. Then, the capillary performance parameter can be defined as:

$$\frac{K}{R_{eff}} = \frac{\phi \mu}{4\sigma} \frac{h^2}{t} \tag{2.4}$$

Capillary performance parameters K/R_{eff} are measured for varying hydraulic diameters $D_h = 4A/P$, where A is cross-sectional area and P is perimeter. As the pore radius varies along the liquid propagation direction, the average D_h and other parameters in a unit cell are related by an expression of the form

$$D_h = \frac{2}{L}\left(\int_0^{d/2} \frac{Xh}{(X+h)}dy + \int_{d/2}^{L} \frac{Xh}{(X+h)}dy\right) \tag{2.5}$$

where X is defined as

$$X = \begin{cases} p - d\cos\left(\mathrm{asin}\left(\frac{2y}{d}\right)\right) & 0 \le y < d/2 \\ p & d/2 \le y < L \end{cases} \tag{2.6}$$

Therefore, the capillary performance parameters K/R_{eff} determined by the computation models are shown with measurement values in Figure 2.11b. The capillary performance parameters K/R_{eff} are mainly governed by the increase in effective inter-nanowire pore sizes or porosity rather than other parameters such as nanowire height. The resulting capillary performance parameter of the nanocactuses with large diameters is increased by six times owing to the large effective pore size while most of nanocactuses possesses the same range of porosity.
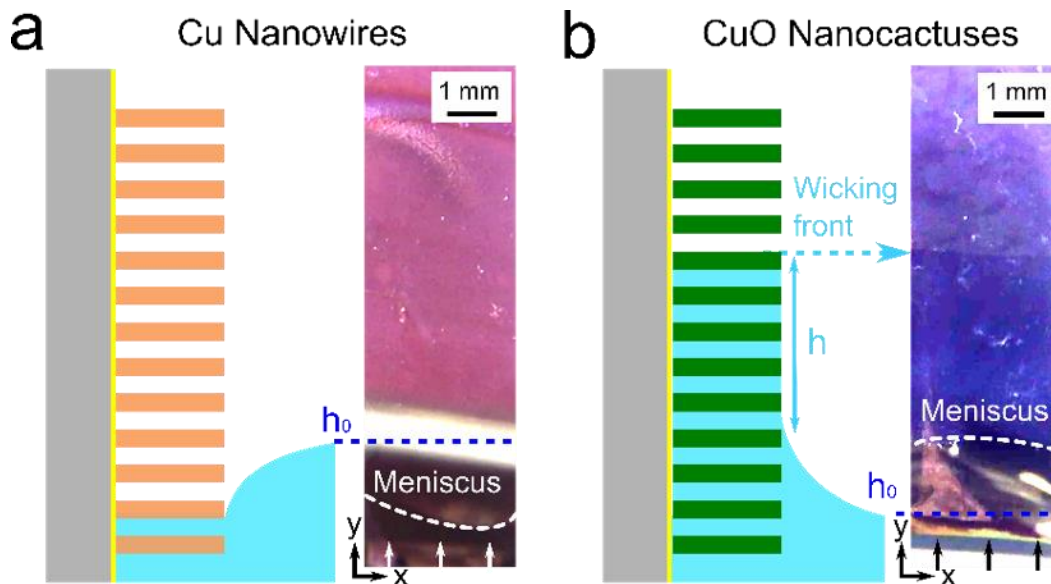
Figure 2.9. Illustrations and optical images comparing the wickability between (a) Cu nanowires and (b) CuO nanocactuses. The meniscus on the nanowires is formed below the water level because the hydrophobic Cu nanowires repel water. The meniscus forms along hydrophilic and hierarchically textured CuO nanocactuses. The wickability is quantified by measuring the liquid-rise-height h from the meniscus.
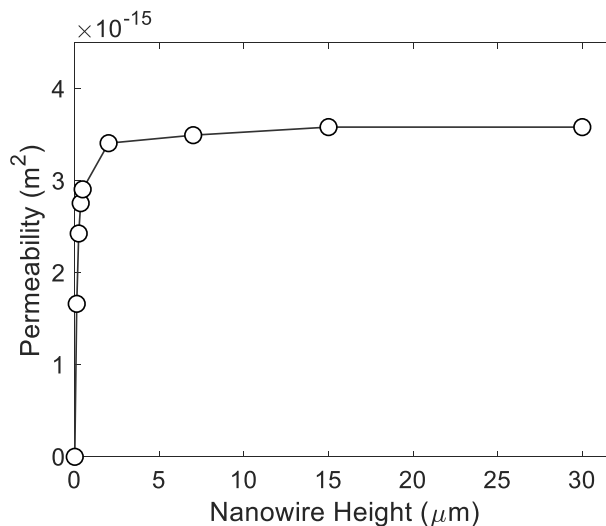
Figure 2.10. Permeability calculation with various nanowire heights. The permeability is calculated by simulation models for various nanowire heights. The nanowires' pitch and diameter used in the simulation models are p = 0.64 μm and d = 467.1 nm, and heights are varying from 116.7 nm to 30 μm. The permeability rapidly increases when nanowire structure shows a low aspect ratio. The sudden change is attributed to the viscous forces

exerted by the bottom surface. Therefore, the diminishing influence of the viscous force due to the increase in the aspect ratio results in constant permeability regardless of nanowire height. The permeability results show a matching trend with the previous studies.

The deviation of experimental values of K/R_{eff} from the theoretical calculations might be attributed to the nanowire disorderness while the computational models assume ideal hexagonal packing configurations. The nanowire geometry in the different types of disorders includes (1) nonuniform diameter distributions that are used to calculate the error bars of K/R_{eff}; (2) pitch distributions between nanowires as explained in morphological details section; and (3) alignment variations represented by tilting structures or entanglements with adjacent nanowires. For example, the past study explained that 70% of nanowire angles is distributed within 10°, whereas the vertical nanowires show 0°.[22–24]
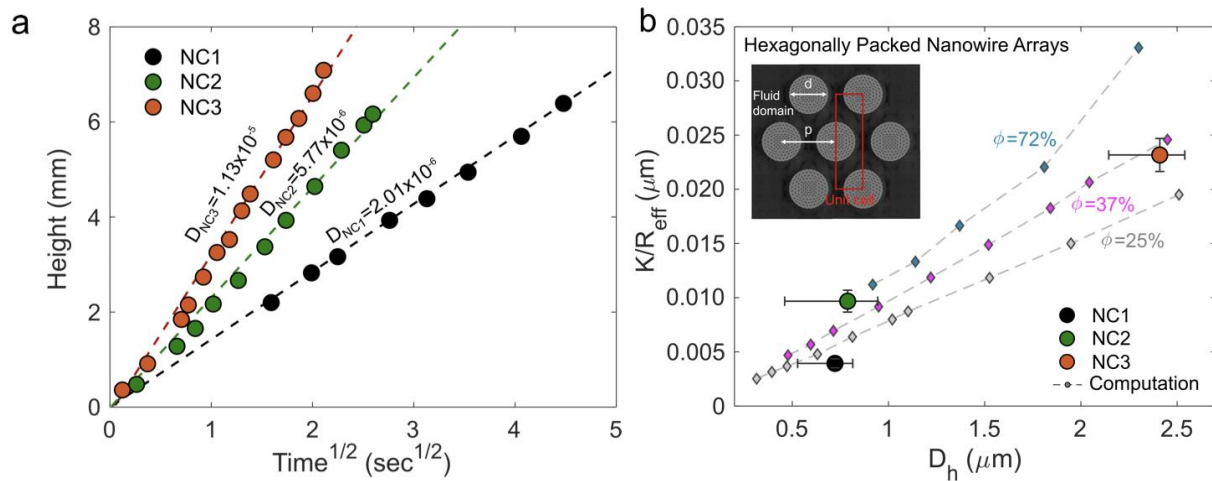
Figure 2.11. Capillary-driven liquid transport and capillary performance parameter of the nanocactuses. (a) The wicking height is plotted for $t^{1/2}$ to show the wickability coefficient D. The error bar represents the standard deviation of the averaged wicking height at different locations. (b) Capillary performance parameters K/R_{eff} of the CuO nanocactuses are plotted for different hydraulic diameters. Inset image shows the unit cell consisting of hexagonally packed nanowire arrays and fluid domain for computational fluidic dynamics calculations. The error bars represent the standard deviation of the diameter and the uncertainty in the capillary performance parameter.

2.4. Summary of the Chapter

In this study, we demonstrate the hierarchically textured, vertically aligned nanowire arrays or CuO nanocactuses that contain submicron nanowires (~100-1000 nm length scale) with a high density of sharp nanoscale oxide features (~10-100 nm length scale). The installation of nanoscale features through the surface oxidization makes CuO nanocactuses become hydrophilic, enabling the hemi-spreading phenomena. The combined experimental measurements and computations explain how the capillary performance parameters improve in relation to the inter-nanowire pores as well as the structural porosity. Thereby, the nanocactuses increase the wicking capabilities with larger diameters that provide larger inter-nanowire pore sizes. The insights from this study help engineer next-generation materials for thermal devices such as microfluidic channels, heat pipes, and flexible cooling system.

CHAPTER 3: Liquid Transport in Hierarchical Surfaces with Heterogeneous Properties

Enhancement of boiling two-phase heat transfer has drawn great interest due to its importance in various applications such as desalination, power generation, and electronics cooling. In a past decade, various engineering surfaces have been suggested to improve boiling heat transfer limit, such as microscale porous media and microposts that offers efficient capillary-driven liquid transport. Although those surfaces successfully enhance critical heat flux (CHF), it has been limited to enhance heat transfer coefficient (HTC) simultaneously due to the conflict effect of wettability on boiling each boiling parameter. In this chapter, we suggest segmented nanowires (NWs) offering heterogeneous wettability to improve CHF and HTC at the same time. We examine the liquid transport through the nanowires with heterogeneous properties such as surface wettability and morphology by evaluating the capillary performance parameter (K/R_{eff}). The K/R_{eff} of NWs with bottom hydrophilic portion is independent to ratio of Cu portion about K/R_{eff} = 0.025 μm. On the other hand, K/R_{eff} for NWs with Ni on top increases as ratio of Ni portion decreases because of the hydraulic resistance produced by hydrophobic Ni portion. The two-step wicking is observed on the segmented NWs with Ni on top and CuO at bottom, which indicates the liquid transport in radial direction through the CuO portion as well as liquid infiltration into Ni portion to out-of-plane direction. As a result, Ni/CuO NWs with heterogeneous wetting properties successfully enhance HTC by 270 % and CHF by 250% owing to the hydrophobic property on top Ni portion, and liquid replenish through capillary wicking on the bottom CuO portion.

3.1. Background

Boiling two-phase heat transfer has been studied intensively in past decades due to its importance on a variety of industrial applications such as desalination, power plants, and electronics cooling devices.[14,18,37,74–76] Performance of the boiling heat transfer is typically quantified by two parameters: heat transfer coefficient (HTC) and critical heat flux (CHF).[7,10,13,77–82] The HTC is a parameter of the heat transfer efficiency as a function of the heat transferred in unit area per superheat, and the CHF is a maximum heat flux on nucleation boiling regime. Therefore, improvement of HTC at low superheat is important for low-heat flux applications to reduce operating temperature, while CHF is salient for high heat flux applications such as high-power density electronics or nuclear reactors. In order to improve heat transfer performance, many studies have been conducted by employing microscale porous structures such as sintered metal particles,[35–37] microgrooves[83–85], and meshes.[86] The use of microscale porous structures significantly improve boiling heat transfer limit *via* extended surface area and liquid transport through them resulting in preventing dry-out of the heating region.

Previous studies successfully reveal that surface wettability determines HTC and CHF on the boiling heat transfer.[10,87–89] On the hydrophobic surface, the HTC in nucleation boiling regime at low superheat is improved by promoted bubble nucleation, whereas the HTC is retarded by late onset of boiling and low bubble nucleation on hydrophilic surfaces.[90–92] In contrast, the CHF decreases on the hydrophobic surfaces in high superheat conditions because the hydrophobic property of the boiling surface hinders rewetting and promotes the formation of the vapor film. When the surface is hydrophilic, CHF is significantly enhanced owing to the efficient rewetting of the boiling surface. Recently,

41

engineering surfaces with a variety of micro- or nanostructures have been reported such as Si nanowires,[38] Cu microposts,[61] hierarchical surfaces,[60,93] and well-ordered inverse opals.[94] Those microporous engineering surfaces achieve enormous enhancement of boiling performance by introducing desirable wettability and wickability.[22,23,30–34] The porous surfaces with hydrophilic property can deliver liquid into the boiling region,[50–55] so that the capillary-fed wicking surface breaks the limit of CHF of the plain hydrophilic surfaces. Note that an increase in roughness of the engineering surfaces allows magnifying hydrophilic or hydrophobic property based on Wenzel and Cassie-Baxter mode of wetting resulting in enhancement of capillary wicking.[72,73] However, those hydrophilic porous media still suffer from low HTC with late onset of boiling the nucleation boiling regime at low superheat.

To address this issue, heterogeneous surfaces such as mixed wettability or hierarchical surfaces have been proposed to enhance HTC and CHF simultaneously.[6,89,95] By employing heterogeneous wettability, the boiling surface could offer both desirable interfacial phenomena including efficient bubble nucleation at the nucleation boiling regime from the hydrophobic region and high CHF from the hydrophilic region.[96] For example, plain surfaces with mixed wettability reported enhancement of both HTC and CHF by 65% and 100%, respectively.[97] In addition, bi-conductive surfaces with embedded epoxy resin improves HTC and CHF greater than 500% and 200%, respectively, by imparting in-plain variations in surface temperature.[83] However, understanding the heterogeneous wettability on boiling heat transfer is still daunting because of the complexity of boiling behavior such as bubble dynamics and capillary-driven liquid transport. In addition, previous studies mainly have focused on the heterogeneous wettability on the plain surface

in which capillary-driven liquid transport is not considered despite the importance of capillary wicking on CHF.

In this study, we suggest vertically aligned segmented nanowires with heterogeneous properties to the out-of-plain direction to create hydrophobic surface in conjunction with capillary wicking. The metals for electrodeposition are selected based on thermal conductivity (398 W/m·K for Cu and 106 W/m·K for Ni), easiness of the electrochemical deposition process, and corrosion resistance. The segmented nanowire delivers heterogeneous characteristics as Ni portion remains intact against oxidation process while Cu portion is oxidized and decorated by CuO nanofeatures. Corresponding surface wettability is modulated to be hydrophilic on the rough CuO portion and hydrophobic with plain surface of the Ni portion. We closely investigate the capillary wicking through segmented nanowire with heterogeneous wettability *via* liquid spreading observation and vertical liquid rate-of-rise test. Furthermore, boiling heat transfer and bubble dynamics are explored on segmented nanowires, which is expected to improve CHF and HTC simultaneously attributed to the hydrophobic surface property that is capable of liquid replenish.

3.2. Experimental Method

3.2.1. Fabrication and Surface Modification

Fabrication of the segmented nanowires is composed of four steps: 1) substrate preparation, 2) templated electrodeposition of metals, 3) surface modifications. Firstly, silicon substrate is prepared with a 12 mm × 12 mm by patterning the Ti/Au (5/50 nm) evaporation with a shadow mask at polished side. Then, copper layer is deposited at the backside of the substrate by E-beam evaporator. The nanowires are fabricated by electrodeposition method with a sacrificial template. Track-etched polycarbonate membrane with pores of 1,000 nm in diameter is used as the template. Metals (Cu and Ni) are electrodeposited in the electrolyte that is confined by an equally sized aperture in the electrochemical cell. For deposition, constant voltage is applied at V = 320 mV (Ag/AgCl). Then, nanowires are further treated by surface oxidation after resolving the sacrificial template in Dichloromethane (Sigma Aldrich, >99%) for 1.5 hrs at 40 °C on the hot plate. The surface oxidation is treated by immersing nanowires in the preheated alkaline solution that is composed of a 1.7M $NaClO_2$ (Sigma Aldrich, > 99%) and a 0.25M NaOH (Sigma Aldrich, > 98% pellet) for 2 min. Then nanowires are cleaned by using deionized water, isopropyl alcohol, and acetone in order.

3.2.2. Surface Characterization

Morphological details of the nanowires are investigated using FEI Magellan 400 SEM at a 15 kV of accelerating voltage for both measurement from top view and cross-sectional view. To capture the cross-sectional images, the nanowires are cleaved and mounted on

vertical sample mount. Surface wetting properties are investigated by the contact angle measurement using a sessile droplet method with a goniometer (MCA-3, Kyowa, Interface Sciences). The goniometer dispenses a 15 nL of deionized water from capillary tip with 30 μm in diameter assisted by constant air pressure (12 kPa). The droplet behavior during contact angle measurement is captured by high-speed microscopic camera from the side to measure contact angle (5,000 fps), and optical microscope from the top to record droplet infiltration and spreading dynamics (30 fps). The contact angle is evaluated by averaging results from three individual measurement in different location at the surface.

3.2.3. Liquid Rate-of-rise Test

Capillary wicking performance is evaluated by the liquid rate-of-rise test, which allows obtaining capillary performance parameters from the Lucas-Washburn equation. The liquid rate-of-rise test is performed in the saturated chamber with water reservoir to prevent undesired evaporation during the test. The chamber is prepared by sealing it using a parafilm with water reservoir at least one week ahead of the test. The liquid rise is captured by optical microscopic camera with LED lighting source at 60 fps as shown in Figure 3.1.
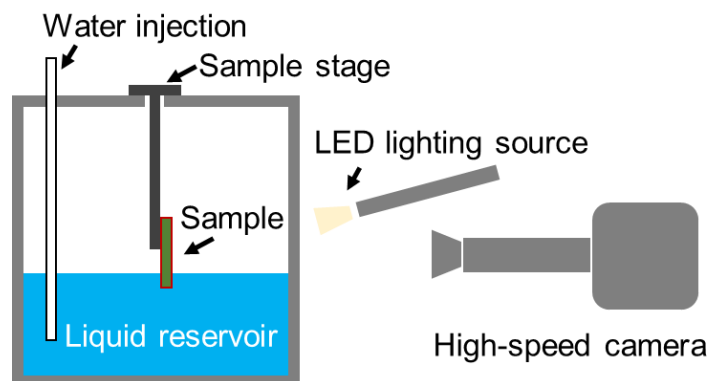
Figure 3.1. Schematic illustration of experimental setup for liquid rate-of-rise test. The setup is composed of the liquid chamber, water injection system, sample stage, and CCD camera. The water is injected gradually to control water height to initiate capillary rise. The test is performed in the saturated chamber to prevent evaporation during the liquid rise.

3.2.4. Pool Boiling Test

Pool boiling heat transfer of the nanowires is experimentally investigated using a custom-built pool boiling experimental setup (Figure 3.2). The pool boiling setup is composed of chamber, data acquisition system, copper block and heaters. The boiling chamber is composed of lid and transparent polycarbonate wall to capture the bubble dynamics using the high-speed camera (FASTCAM Mini AX50) at 2000 fps with LED lighting source. Heat flux and surface temperature in boiling test are calculated from the temperature results obtained from data acquisition system (LabJack U6) connected to four K-type thermocouples to read temperatures of the copper block. Thermal energy is generated from the four cylindrical cartridge heaters (Omega, CIR-20191) that are inserted at the bottom of the copper block. The heat flux is controlled by slowing increasing power using voltage transformer (Variac AC variable voltage converter). Before the boiling test, sample is placed and attached on the 1 cm $\times$ 1 cm copper block through soldering. Once the sample is firmly fixed on the copper block with proper PDMS sealing, the chamber is filled with working fluid (DI water). To maintain the water temperature close to saturation temperature, a guard heater that is connected to proportional integral derivative controller is used and immersed in the water.
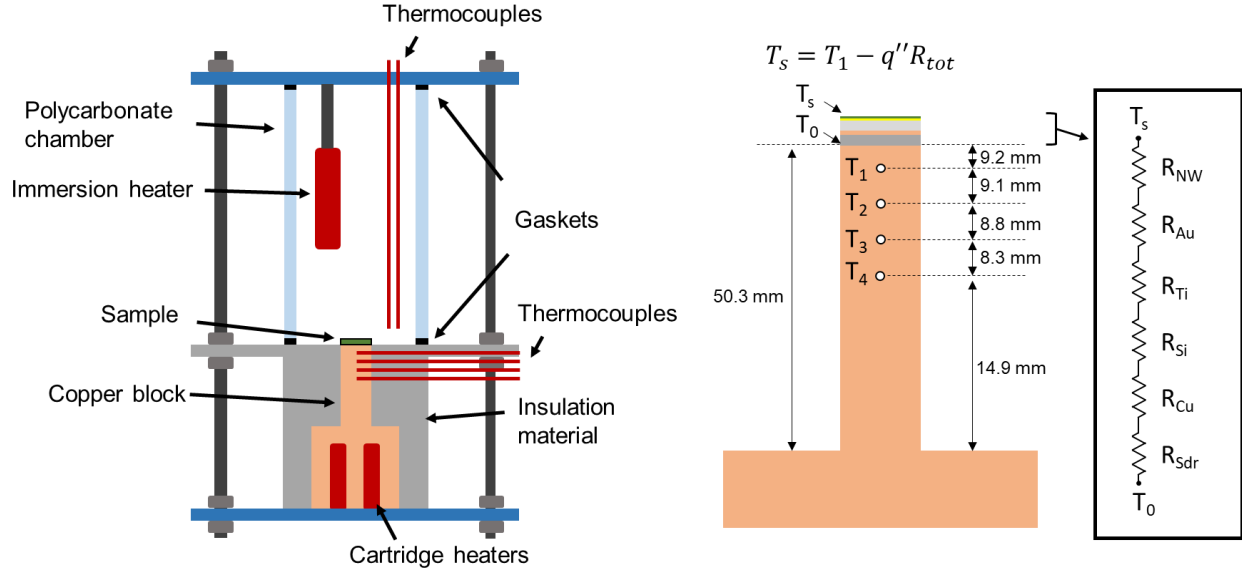
Figure 3.2. Schematic illustration of pool boiling experimental setup. The experimental setup is composed of a clear polycarbonate chamber, data acquisition system connected to thermocouples that are inserted in a copper block, proportional integral derivative (PID) controller connected to immersion heater and thermocouples, and cartridge heaters. The heat flux and the surface temperature (T_s) are calculated based on the temperature of the copper block (T1, T2, T3, and T4) by assuming one-dimensional heat conduction. The power of the cartridge heat is controlled by an AC power supply to heat up the copper block.

Heat flux and heat transfer coefficient are calculated based on the temperature difference at T1, T2, T3, and T4 of the copper block by following equation:

$$q'' = \frac{1}{3} k_{Cu} \left[\frac{T2 - T1}{t_{2-1}} + \frac{T3 - T2}{t_{3-2}} + \frac{T4 - T3}{t_{4-3}} \right] \tag{3.1}$$

where k is the thermal conductivity, t is the thickness of Cu block between thermocouples, and q'' is the heat flux. To calculate surface temperature T_s, total thermal resistance is evaluated considering all layers listed in Table 3.1.

$$R_{tot} = \frac{t_{Sdr}}{k_{Sdr}} + \frac{t_{Cu}}{k_{Cu}} + \frac{t_{Si}}{k_{Si}} + \frac{t_{Ti}}{k_{Ti}} + \frac{t_{Au}}{k_{Au}} + \frac{t_{NW}}{k_{NW}} \tag{3.2}$$

Then, T_s and heat transfer coefficient h can be obtained by following equations:

$$T_s = T_1 - q'' \frac{t_{1-0}}{k_{Cu}} - q'' R_{tot} \tag{3.3}$$

$$h = q''/(T_s - T_{sat}) \tag{3.4}$$

where T_{sat} is the saturation temperature of the water.

Table 3.1. Thickness and thermal conductivity for consideration of effective thermal resistance

Material	Subscript Notation	Thickness t (nm)	Thermal Conductivity k (W/mK)
Copper	Cu	1000	398
Titanium	Ti	5	16
Gold	Au	50	314
Silicon	Si	300000	130
Solder	Sdr	100000	55
Cu Nanowires	NW	20000	40

3.3. Results and Discussion
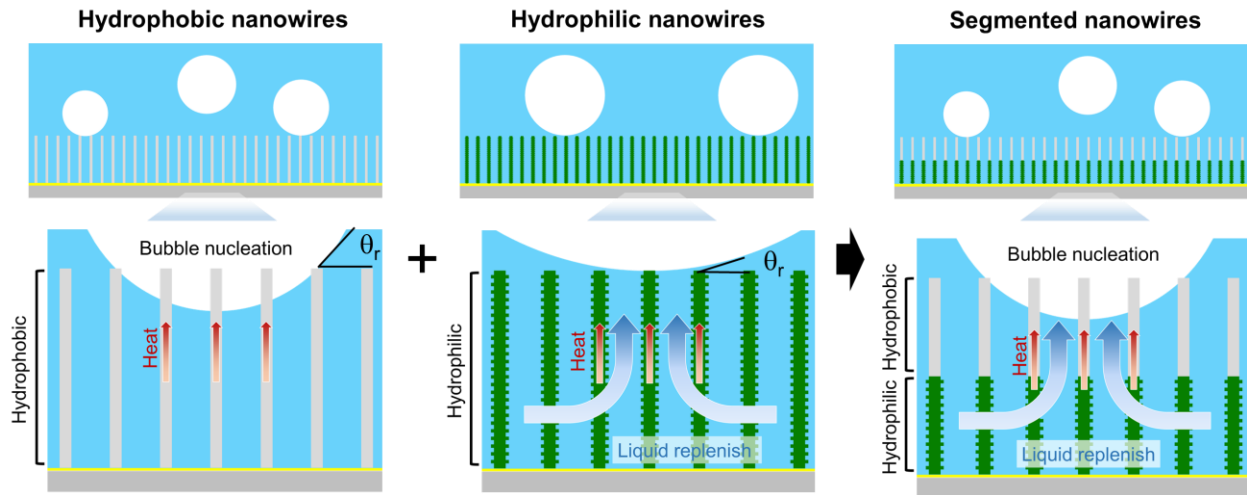
Figure 3.3. Schematic illustrations of pool boiling on segmented nanowires. Illustrations depict bubble nucleation and liquid replenish in the nanowires (NWs) with homogeneous hydrophobic, hydrophilic wettability, and segmented NWs with heterogeneous wettability. For NWs with top Ni and bottom Cu decorated with CuO nanofeatures (Ni/CuO NWs), top hydrophobic Ni portion offer efficient bubble dynamics resulting in enhancement of HTC at low superheat conditions. In addition, CHF can be improved by capillary-driven liquid replenish from bottom CuO portion that provides desirable surface porosity and hydrophilic property for capillary wicking.

To systematically investigate liquid transport and boiling heat transfer on the surfaces with heterogeneous wettability, we design the nanowires composed of two different type of metals (Cu and Ni) with distinct surface roughness and wettability. Our previous study showed that wicking enhancement can be achieved using hierarchical nanowires with submicron diameter (200 nm – 1000 nm) by installing uniform CuO nanofeatures offering enormous surface roughness and hydrophilic property.[93] Then, Ni is employed to provide hydrophobic wettability via hydrophobic intrinsic wettability and corrosion resistance. We select the template with pores of 1000 nm in diameter that showed the significant enhancement in capillary wicking owing to their large permeability and

49

capillary pressure to investigate the liquid transport in hierarchical surfaces in presence of heterogeneous property. Through this experimental observation, two main parameters can be demonstrated: 1) effect of intrinsic wettability of metal component on the surface wetting property, and 2) liquid transport phenomena through capillary wicking with the existence of hydrophobic layer to out-of-plane direction. Boiling heat transfer is further examined to explain how heterogeneous wettability impacts boiling heat transfer such as HTC and CHF. As shown in Figure 3.3., high nucleation density is expected in low supersaturation condition leading to high HTC. In high superheat condition near boiling heat flux limit, superhydrophilic CuO portion is expected to improve CHF through continuous capillary wicking to prevent dry-out of the boiling surfaces.
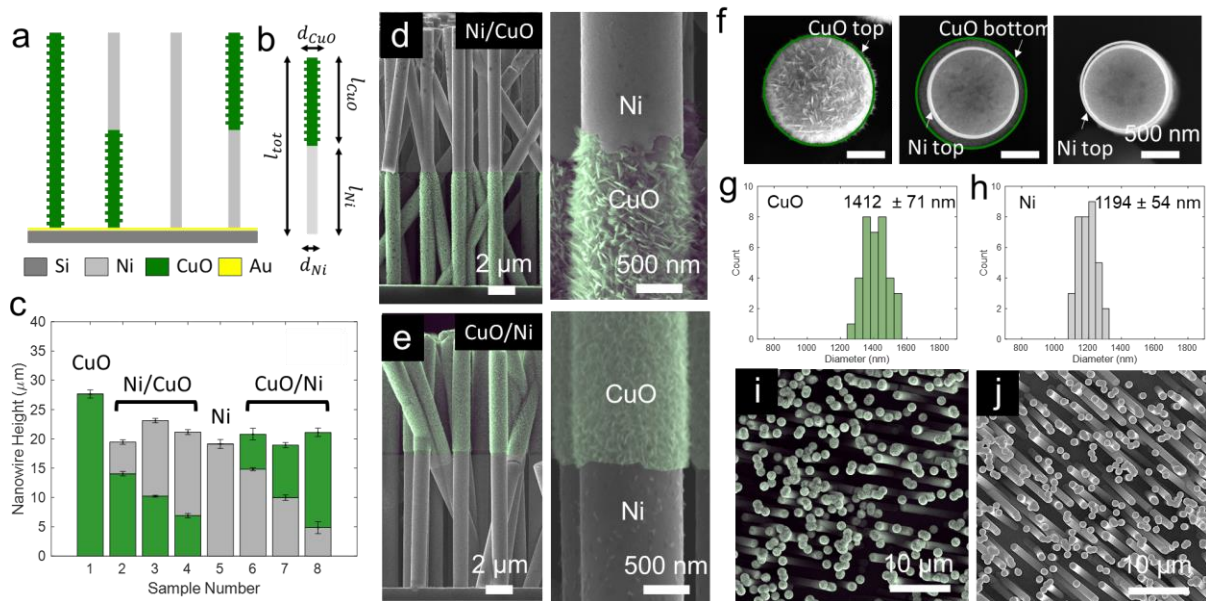
Figure 3.4. Morphological details of segmented NWs composed of Cu and Ni. (a) Schematic illustration shows the type of the nanowires with homogeneous Cu (green color) or Ni (gray color), and heterogenous NWs with combination of both Cu and Ni. After oxidation, Cu portion is oxidized and decorated with high dense and sharp CuO nanofeatures, while Ni portion remains intact due to high corrosion resistance of Ni. (b) The level of

segmentation is controlled by ratio of length of CuO (l_{CuO}) and Ni (l_{Ni}). (c) All of the NWs is fabricated to have constant total length of the NWs ($l_{tot}\approx$20 μm). The green and grey color represents CuO portion and Ni portion, respectively. Cross-sectional SEM images show morphology of segmented (d) Ni/CuO NWs (sample 3) and (e) CuO/Ni NWs (sample 7), which clearly display vertically aligned nanowires without broken after oxidation. (f) SEM images show the top of individual nanowire for Ni, Ni/CuO and CuO/Ni NWs. Diameter of NWs increases after oxidation due to the additional CuO layer around the Cu portion, while Ni portion remains intact. The histograms show the distribution of nanowires' diameter of the (g) CuO portion and (h) Ni portion. SEM images show morphologies of segmented nanowires NWs with (i) CuO on the top and (j) Ni on the top from top-view measurement. The quantification of the overall porosity is calculated from the solid fraction of the NWs, $\varepsilon = \pi d^2 N/4$,where d and N is the diameter and number density of the NWs, respectively. The number density N of NWs are measured by counting number of NWs divided by area. The scale bar is 10 μm.

3.3.1. Morphology of Segmented Nanowires and Surface Modification

We prepare the segmented nanowires *via* electrodeposition using porous sacrificial templates (see Experimental section for details).[64,69] The templated electrodeposition method allows deposition of various types of metal through additional deposition with accurately controlled nanowires' length. In this study, we prepare four types of nanowires, which is homogeneous nanowires (Cu NWs, Ni NWs) and segmented nanowires (Cu/Ni NWs, Ni/Cu NWs). Cu/Ni represents that the Cu and Ni portions are placed on the top and the bottom, respectively, and vise versa (Figure 3.4a). The segmented nanowires are fabricated to have constant total length $l_{tot} \simeq$ 20 μm with different ratio of Cu portion (l_{Cu}/l_{tot}) and ratio of Ni portion (l_{Ni}/l_{tot}) where the total length is $l_{tot} = l_{Cu} + l_{Ni}$ (Figure 3.4b). Figure 3.4c and Table 3.2. show the details of nanowires. The average l_{Cu}/l_{tot} is 0.72, 0.44, and 0.33 for Ni/Cu NWs, and 0.29, 0.47, and 0.84 of Cu/Ni NWs.

The as-fabricated nanowires are oxidized via chemical immersion method leading to desirable surface wettability at Cu and Ni portion separately. Due to the corrosion resistance

of Ni, the Cu portion is selectively oxidized and decorated by CuO nanofeatures as shown in Figure 3.4d-e. The CuO nanofeatures offer enormous surface roughness on the nanowire surface owing to the high density of sharp nanoscale features. In addition, diameter of nanowires changes as CuO nanofeatures add extra diameter for Cu portion. SEM images (Figure 3.4f) clearly show that Ni portion sustains smooth surface without changes in surface roughness and diameter, while roughness and diameter of CuO portion increase. Note that Ni can react with NaOH resulting in the formation of Ni(OH)$_2$ film. But EDS results show the atomic concentration of Ni (~85%) and oxygen (<10%) indicating the neat Ni surface. The nanowires' diameter is measured from cross-sectional images as shown in Figure 3.4g-h. The average diameter of Ni NWs and CuO NWs is d_{Ni}=1194 nm and d_{CuO}=1412 nm, respectively, which impacts porosity ϕ of the nanowires after oxidation.
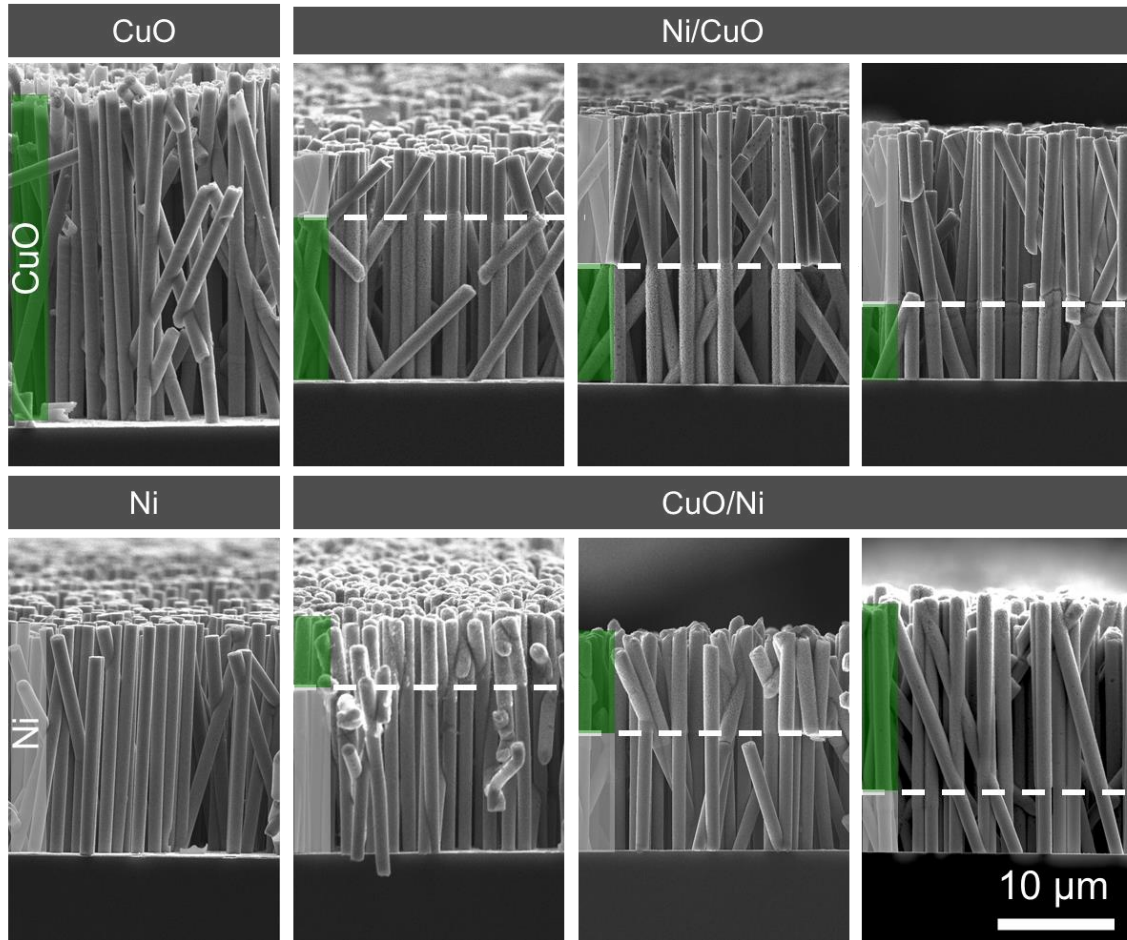
Figure 3.5. Cross-sectional SEM images of the nanowires. The green and gray color bars represent CuO and Ni portion, respectively. The white dashed line shows the boundary between CuO and Ni portion.

We calculate the overall porosity of the nanowire based on the nanowires' number density and solid fraction ε, where porosity is determined as a void fraction of the material system $\phi = 1 - \varepsilon$. Solid fraction of nanowires is evaluated by the portion of nanowires divided by total surface, $\varepsilon = \pi d^2 N / 4$. As shown in Figure 3.5, the chemical oxidation is only attributed to the oxidation of Cu surface and does not influence the nanowires' geometry such as misalignment and cleaving. The number density of nanowires is $N = 0.23$ μm^{-2} obtained from the top-view SEM images, which is constant for all the nanowires in this study.

In addition, the overall porosity of segmented nanowires is impacted by ratio of the segmented Cu and Ni portions owing to the difference in diameter between two metal segments. Therefore, the porosity of the segmented nanowire after oxidation can be calculated by equation 3.5:

$$\phi = 1 - \frac{\pi N}{4l_{tot}}(d_{Ni}^2 l_{Ni} + d_{CuO}^2 l_{CuO}) \tag{3.5}$$

The calculation results are listed in the Table 3.2 and the porosity of the segmented nanowires is ranging from 64% to 74%, which is not significantly different. Note that the areal loss from entanglement of the nanowires is evaluated as 0.2% from our previous study and considered to evaluate the porosity in this study.[93]

Table 3.2. Summary of sample details for segmented nanowires after oxidation.

Sample number	Segment type	l_{Cu}/l_{tot}	ϕ	θ_{app} (°)
Sample 1	CuO	1.00	0.64	23.7
Sample 2	Ni/CuO	0.72	0.67	60.4
Sample 3	Ni/CuO	0.44	0.70	55.8
Sample 4	Ni/CuO	0.33	0.71	48.3
Sample 5	Ni	0	0.74	103.5
Sample 6	CuO/Ni	0.29	0.71	25.7
Sample 7	CuO/Ni	0.47	0.69	26.6
Sample 8	CuO/Ni	0.84	0.66	25.8
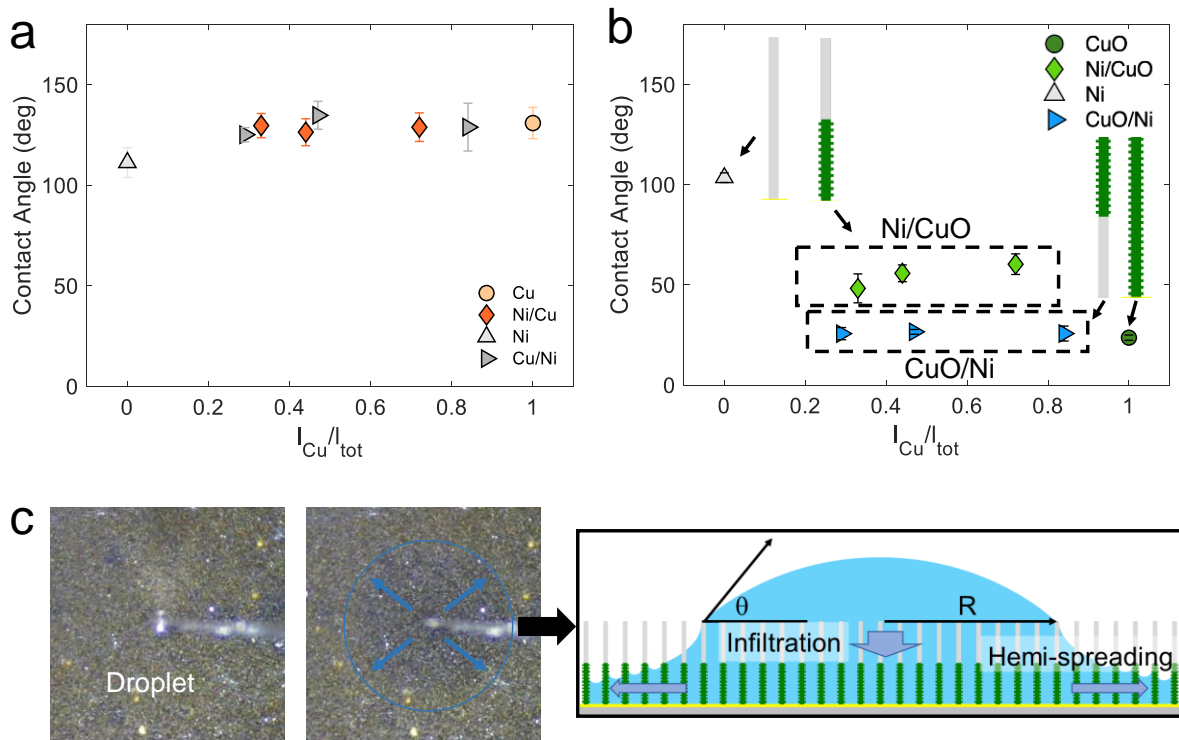
Figure 3.6. Wettability of the segmented NWs before and after oxidation. Contact angle of segmented NWs is evaluated by sessile drop method (a) before and (b) after oxidation process. (c) Photograph images and illustration show droplet imbibition during contact angle measurement, so-called "hemi-spreading". Due to the hemi-spreading, droplets imbibition into nanowire arrays and then are fully absorbed. Therefore, the contact angle of the NWs is investigated by measuring the angle when the sessile drop becomes stable before absorption.

3.3.2. Wettability of Segmented Nanowires

We characterize the interfacial phenomena such as wetting and spreading by performing contact angle measurement of the segmented nanowires, which is directly related to boiling heat transfer. The wetting property of the segmented NWs before oxidation is generally hydrophobic due to the intrinsic hydrophobic property of Cu and Ni. For direct comparison with nanowire arrays that is prepared by electrodeposition method, plain Ni and Cu surfaces are prepared on the same substrate in which the contact angle of plain Cu and Ni

surfaces are 101° and 68°, respectively. (see Figure 3.9 for details). Due to the roughness from nanowire arrays comparing to plain surface, the contact angles of nanowires are more hydrophobic than plain surface about 130° for Cu NWs, Cu/Ni NWs, Ni/Cu NWs, and 110° for Ni NWs (Figure 3.6a). After the chemical oxidation, the hydrophilicity of Cu portion is significantly improved by the installation of hydrophilic CuO nanofeatures, which eventually allows superhydrophilic property about 20° of contact angle (Figure 3.6b). The CuO NWs and CuO/Ni NWs provides the surface hydrophilic property and surface roughness (Figure 3.4i) in the three-phase contact line. We further observe that the NWs with Ni portion on top (Ni/CuO NWs) become hydrophobic with contact angle over 50°, and the Ni NWs maintains its hydrophobic wettability about 120° as Ni resists corrosion. The contact angle of the porous media is inevitably affected by the liquid spreading behavior because droplet eventually interacts with surfaces filled with liquid that provides more hydrophilic property than the surfaces filled with air.
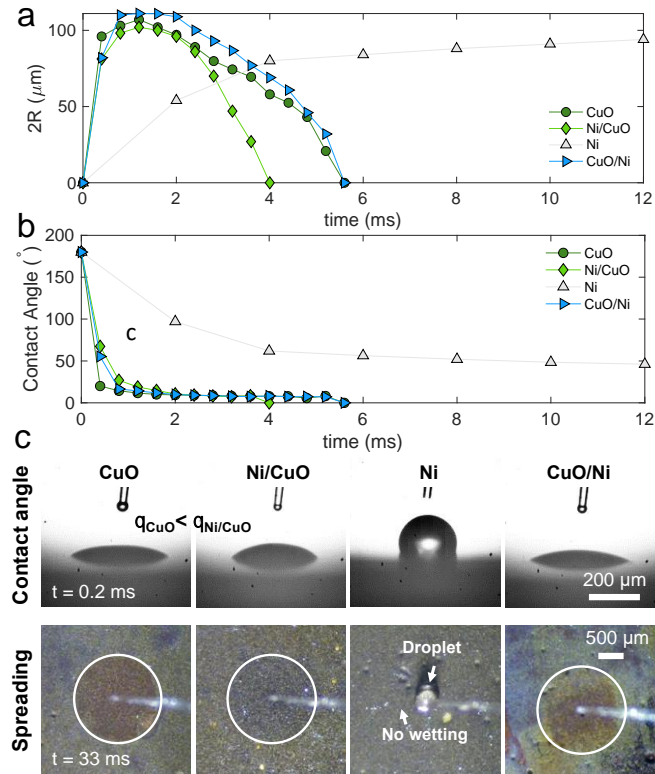
Figure 3.7. Droplet imbibition process. (a) Contact area and (b) dynamic contact angle analysis show droplet imbibition process in segmented nanowires including CuO NWs, Ni/CuO (50/50) NWs, Ni NWs, and CuO/Ni (50/50) NWs over time. Nanowire arrays with hydrophilic CuO portion fully absorb droplets within 10 ms through capillary wicking, whereas nanowires with only hydrophobic Ni takes 250 ms. (c) The CuO NWs and the CuO/Ni NWs initially show superhydrophilic property (~20°), whereas the Ni/CuO NWs initially show hydrophobic (~56°) property due to the top hydrophobic Ni portion.
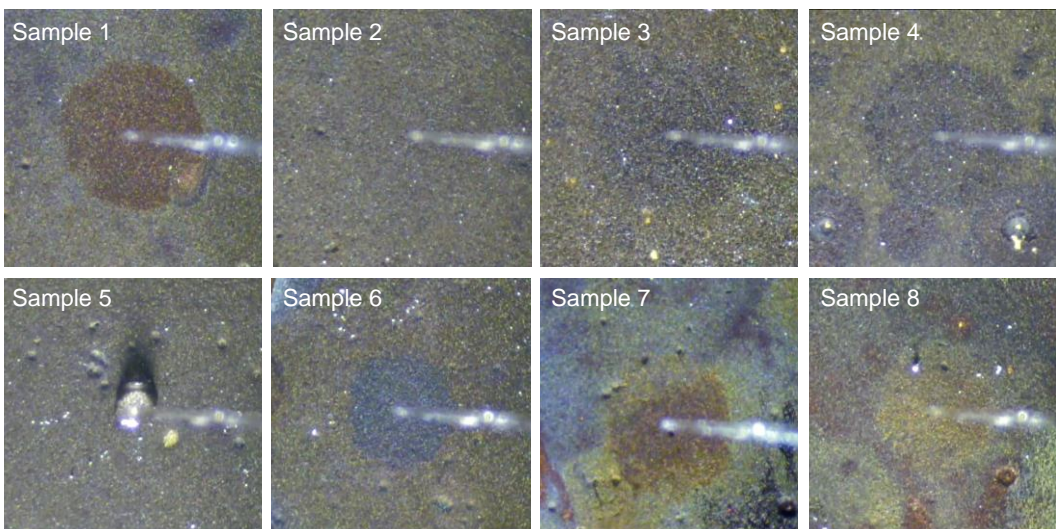
Figure 3.8. Droplet imbibition and radial spreading during contact angle measurement of nanowires after oxidation. The top-view microscopic images are captured by the optical microscope at 30 fps. The images show the droplet imbibition and spreading at t = 33ms. The droplet on NWs with CuO portion is fully imbibed and finally spread through nanowires as shown in white circles. On the other hand, the Ni NWs (sample 5) do not show distinct wetting through spreading that indicates a lack of capillary wicking to lateral direction of nanowires, whereas the droplet is imbibed into out-of-plain direction by interacting with hydrophilic Au layer placed at the bottom of nanowires.

The contact angle measurement is also impacted by capillary action through the pores, so-called "hemi-spreading".[70,71] Once the sessile drop is placed on the porous media, the droplet is imbibed into the pores and spreads to a radial direction as shown in Figure 3.6c and Figure 3.7. This hemi-spreading behavior results from Cassie to Wenzel transition.[72,73] To quantify criteria for the wetting transition, critical contact angle is suggested as $\theta_c = cos^{-1}(1 - \varepsilon)/(r - \varepsilon)$, where r is the roughness. We assume nanowire arrays are aligned as a hexagonal array, which gives $r = 1 + 2\pi d l_{tot}/\sqrt{3}p^2$ where the pitch between nanowires is $p = (2/\sqrt{3}N)^{0.5}$. We obtain the critical contact angle is θ_c=87° from r_{NW} = 21 and p = 2240 nm indicating that hemi-spreading can occur for all nanowires because intrinsic contact angle of Ni and CuO is lower than θ_c. Our results agree well with the expectation that the sessile drop infiltrates into the pores for all nanowire arrays. However, changes in color due to the wetting are not observed in Ni NWs as shown in Figure 3.8, which indicates that capillary pressure is applied at the bottom due to the hydrophilic Au layer under the nanowire arrays. Therefore, it is reasonable speculation that the droplet infiltrates vertically followed by radial spreading through capillary pressure caused by hydrophilic Au layer underneath hydrophobic nanowires.
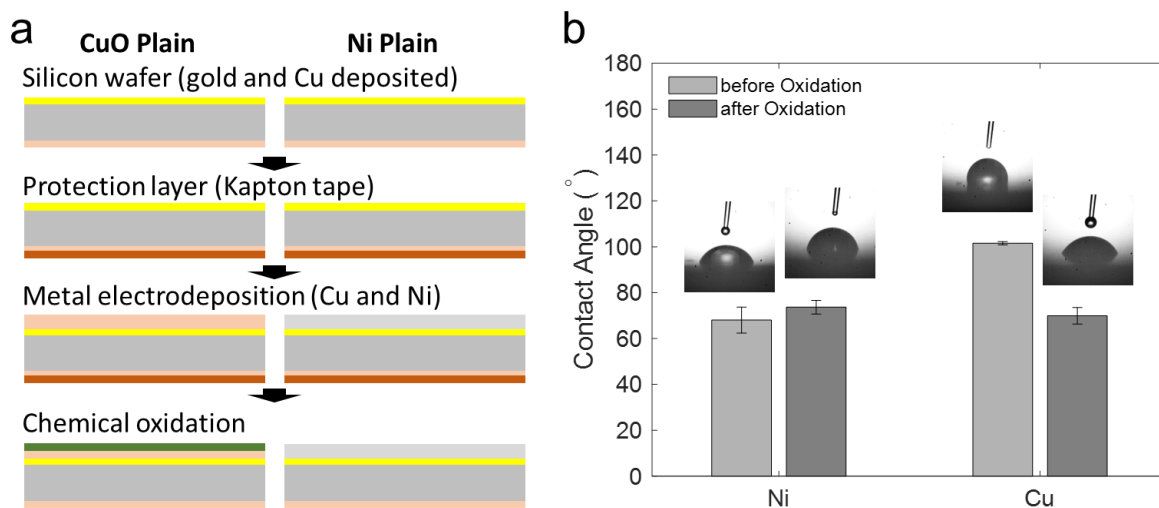
Figure 3.9. Fabrication and contact angle results of the plain metal surface before and after oxidation. (a) The silicon wafer is formerly coated by Au and Cu layer on bottom and top side of the wafer, respectively. The plain and structured metal surfaces are fabricated on Au layer by electrodeposition method. Cu layer on the silicon backside is coated *via* E-beam evaporator for proper soldering to attach on the stage of the boiling measurement setup. Plain surface is fabricated on the gold-deposited silicon wafer. (b) Intrinsic contact angle of Cu decreases after oxidation while Ni maintains original wettability.

Droplet imbibition into porous media can be analyzed by liquid infiltration theory that shows three phases of droplet absorption.[98–101] The three phases of the infiltration are increasing drawing area (IDA), constant drawing area (CDA), and decreasing drawing area (DDA). Each phase explains absorption behavior of the droplet by diameter (2R) of contact area and dynamic contact angle. After a droplet is placed on the porous surfaces, the droplet forms spherical cap by increasing 2R and decreasing contact angle in IDA phase (Figure 3.7). Then, the droplet is absorbed into the porous surface with constant 2R and decrease in contact angle in CDA phase. Once contact angle reaches to receding contact angle, the droplet is absorbed by decreasing both 2R and contact angle in DDA phase. Changes in 2R does not show significant difference among the nanowires. On the other hand, dynamic contact angle clearly shows that the nanowire arrays with CuO portion on top allows

hydrophilic property in IDA phase as shown in Figure 3c Ni/CuO NWs shows initially hydrophobic property than CuO NWs or CuO/Ni NWs in IDA phase. The droplet is eventually imbibed with a decrease in contact angle below 25° during CDA phase (Figure 3d). On the other hand, Ni NWs takes 500 ms to fully absorb the droplet into the surface with hydrophobic property with initial contact angle over 100°. In addition, we do not observe the color changes of the surface by wetting that indicates the radial spreading while droplet is imbibed, which show non-wicking property of Ni NWs to the lateral direction.
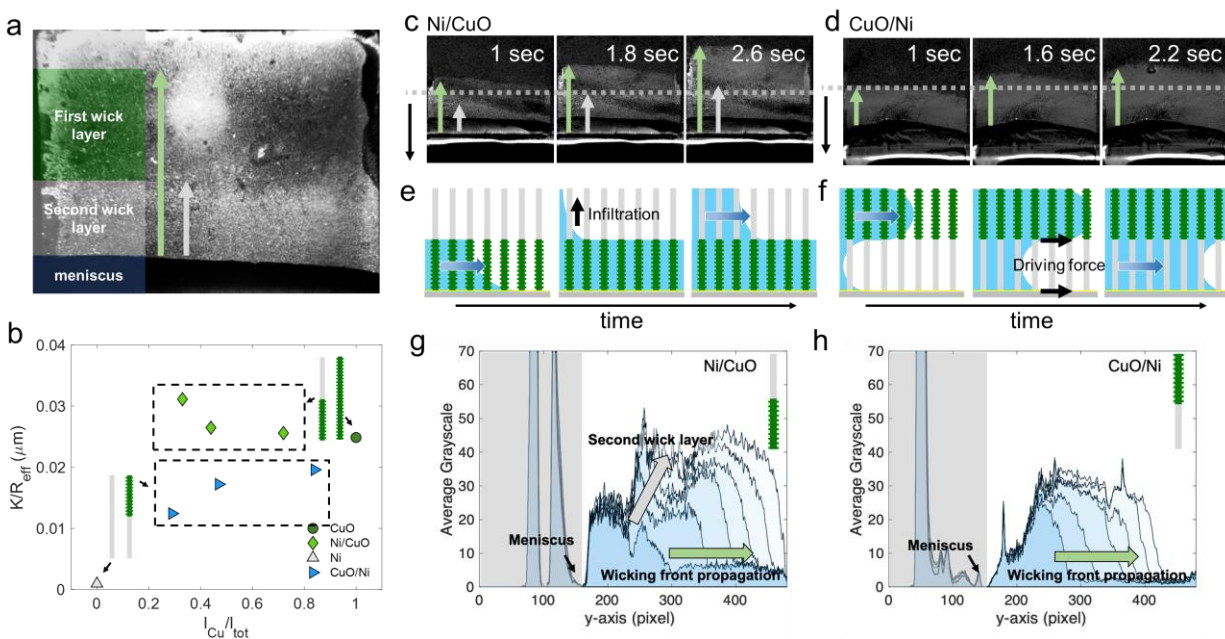
Figure 3.10. Capillary-driven liquid transport into segmented NWs. (a) A microscopic image of Ni/CuO NWs shows a two-step liquid rise due to the heterogeneous wettability. The captured images of liquid rise are processed by subtracting the first images from the other images to examine changes in grayscale. (b) Capillary performance parameter (K/R_{eff}) of the segmented NWs is obtained from the Lucas-Washburn equation. The nanowire arrays with CuO portion at the bottom show around constant wicking performance ($K/R_{eff} \simeq 0.025$ µm). Liquid rise is captured by a microscopic optical camera at 60 fps. The images show changes in grayscale when wicking front propagates on (c) Ni/CuO NWs and (d) CuO/Ni NWs. Schematic illustrations show wicking mechanism through (e) Ni/CuO NWs and (f) CuO/Ni

60

NWs. It shows the wicking status in the gray dashed line in the images. The average grayscale shows the liquid rise of (g) Ni/CuO NWs and (h) CuO/Ni NWs. As wicking front propagates, location of average grayscale greater than plateau region propagate toward higher height. In addition to this, second greyscale picks are only observed in Ni/CuO NWs.

3.3.3. Capillary Wicking through Segmented Nanowires

To systematically investigate the liquid transport performance through porous surfaces with heterogeneous wettability, we measure capillary performance parameters through liquid rate-of-rise test. The capillary performance parameter defined by permeability over effective pore radius (K/R_{eff}) is obtained from Lucas-Washburn equation[22–24]

$$h^2 = \frac{4\sigma}{\phi\mu}\frac{K}{R_{eff}}t \tag{3.6}$$

where h is the liquid height, t is the time, μ is the liquid viscosity, σ is the surface tension of the liquid. The effective pore radius is $R_{eff} = R_p/\cos\theta_s$ where R_p is the pore radius and θ_s is the static contact angle. We observe that the K/R_{eff} significantly increases as Cu portion increases for CuO/Ni NWs from 0.001 μm to 0.025 μm as shown in Figure 3.10. On the other hand, Ni/CuO NWs generally maintain higher level of K/R_{eff} than CuO/Ni NWs regardless of l_{Cu}/l_{tot}. This is because higher capillary pressure is applied by interaction with bottom hydrophilic layer for Ni/CuO NWs, whereas capillary pressure is applied through pores without assist from top and bottom of the CuO portion for CuO/Ni NWs. The Ni NWs does not show distinct capillary rise even though the droplet is imbibed during the contact angle measurement (Figure 3.8), which indicates that Ni portion does not contribute to either capillary rise or spreading except vertical infiltration.

The heterogeneous wettability of the segmented NWs results in unique two-step liquid transport behavior. The two-step liquid transport means wicking front, the first wick layer, is followed by the second wick layer as shown in Figure 3.10a. The two-step liquid transport behavior is observed only in Ni/CuO NWs (Figure 3.10c), while the CuO NWs and the CuO/Ni NWs show traditional capillary rise behavior (Figure 3.10d). To quantify the two-step liquid rise, average grayscale is calculated from the processed images for Ni/CuO NWs (Figure 3.10e) and CuO/Ni NWs (Figure 3.10f). During the traditional capillary rise, grayscale increases and propagates. On the other hand, secondary grayscale peaks are clearly seen during the two-step liquid transport for Ni/CuO NWs in addition to the typical wicking front propagation. This two-step liquid transport can be described by the heterogeneous wetting of the CuO and Ni portion. The first wick layer from the captured images is observed from the wicking front in CuO portion, and then the second wick layer is observed by the infiltration through the Ni portion (Figure 3.10g). Note that the infiltration of droplet to vertical direction of nanowires is demonstrated in the wettability section. However, bottom Ni portion of the CuO/Ni NWs cannot be observed by the optical observation from the liquid rate-of-rise test (Figure 3.12). As so, we speculate the liquid transport behavior in CuO/Ni NWs based on the K/R_{eff} results that is dependent to the l_{Cu} (Figure 3.10h). In contrast, the K/R_{eff} increases as l_{Cu} increases for CuO/Ni NWs, which indicates the liquid transport in Ni portion occurs simultaneously so that the capillary wicking is obstructed due to the hydraulic resistance from the hydrophobic Ni portion (Figure 3.11).
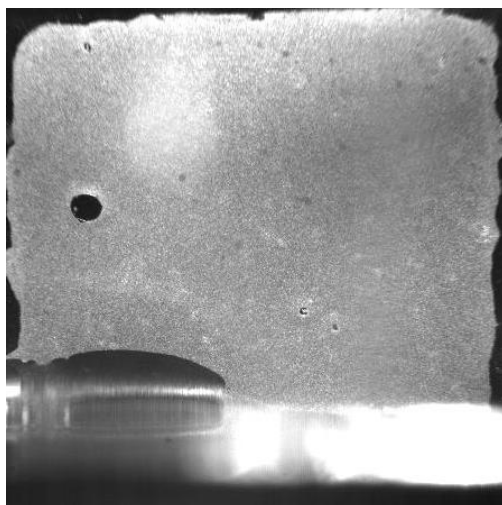
Figure 3.11. Liquid rise on Ni NWs at 10sec. Capillary wicking is not observed on the Ni NWs due to the hydrophobic property. The meniscus that is formed partially on the edge of the sample might be due to the exposure of the hydrophilic Au bottom layer.
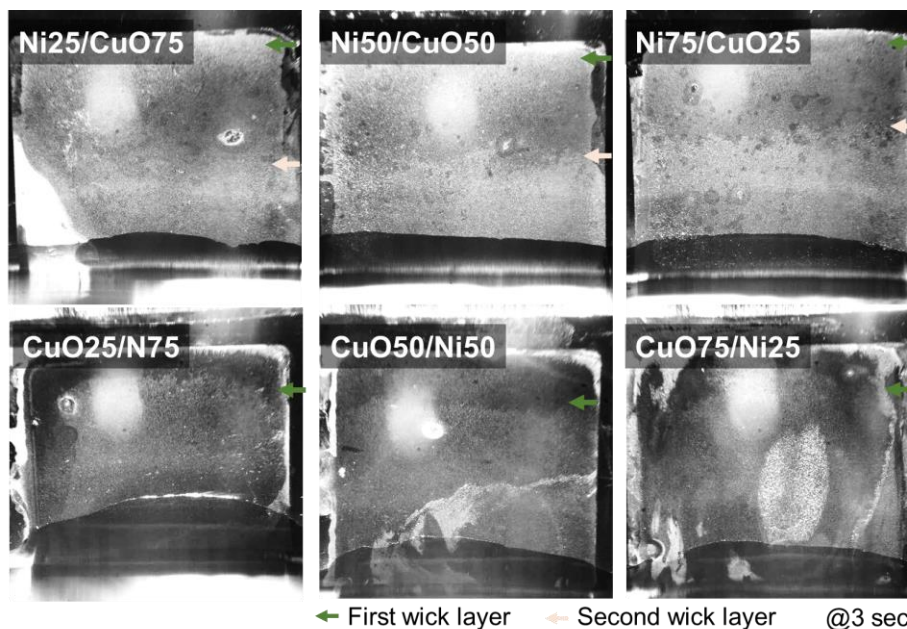
Figure 3.12. Two-step capillary wicking on segmented nanowires. The second wick layer is observed during the wicking process on Ni/CuO NWs in which the hydrophilic portion is placed at the bottom portion and hydrophobic non-wicking layer is placed on top. On the other hand, traditional capillary rise is observed with dragging by the hydrophobic layer instead of separated capillary rise between two Cu and Ni portion.

63

3.3.4. Boiling Two-Phase Heat Transfer

Pool boiling experiment is performed using four types of nanowires (Cu NWs, Ni/CuO NWs, Ni NWs, CuO/Ni NWs) to investigate how the heterogeneous wetting property enhances two-phase heat transfer. The two-phase heat transfer performance is analyzed by investigating HTC and CHF during pool boiling experiment, which is obtained from $q'' = h(T_s - T_{sat})$ where q'' is the heat flux, h is the HTC, T_s is surface temperature, and T_{sat} is the saturation temperature of the water, and superheat is $\Delta T = T_s - T_{sat}$. As shown in Figure 3.13a, nanowire arrays with CuO portion show enhancement of CHF up to 270% comparing to the plain hydrophilic surface. The CHF is 128.1 W/cm² and 122.9 W/cm² for CuO NWs and Ni/CuO NWs, respectively. We also observe that CHF of the CuO/Ni NWs and Ni NWs is significantly reduced by 20% and 33% comparing to that of CuO NWs. The CHF results agree well with a previous study that explains CHF is dictated by the capillary wicking for superhydrophilic engineering surfaces.[60] Importantly, our results show that CHF is determined by wickability of superhydrophilic porous surface rather than dynamic wetting on the surface. In addition, the heat flux at ΔT = 10 K confirm that the HTC of the hydrophobic surface show higher than hydrophilic surface in nucleation boiling regime at low superheat condition. The HTC is 14.5 W/cm²·K and 16.8 W/cm²·K for the Ni/CuO NWs and Ni NWs, respectively, which achieves 250% and 290% enhancement comparing to plain Si surface. Furthermore, the HTC of CuO/Ni NWs is 10% higher than that of CuO NWs at ΔT = 10K. Therefore, the boiling results proves our concept that segmented nanowires with heterogeneous wetting property to in-plane direction enhances CHF and HTC simultaneously.

The bubble dynamics further confirm how surface wettability impacts boiling heat transfer at low superheat conditions by facilitating bubble generation. As shown in Figure 3.13b, bubbles are rigorously generated and departed from the Ni/CuO NWs due to the surface hydrophobic property of the Ni portion. On the other hand, the CuO NWs and CuO/Ni NWs show similar bubble dynamics with lower number of bubbles nucleated on the surface. This result shows that bubble generation at low superheat condition is strongly determined by the wettability of the surface that directly contacts to liquid. In contrast, the bubble dynamics at CHF does not show significant difference for all nanowires, which shows transition to film boiling where the surface is fully covered by vapor as shown in Figure 3.13b. Even though bubble dynamics at CHF is currently challenging due to the similarity of bubble behavior at the CHF and at high superheat condition, advancement in computer vision technique through machine learning will allow handling the image to predict the CHF.[102] Furthermore, the heterogeneous property to in-plane direction could be combined with heterogeneous property to out-of-plane direction in order to separate liquid-vapor pathway.
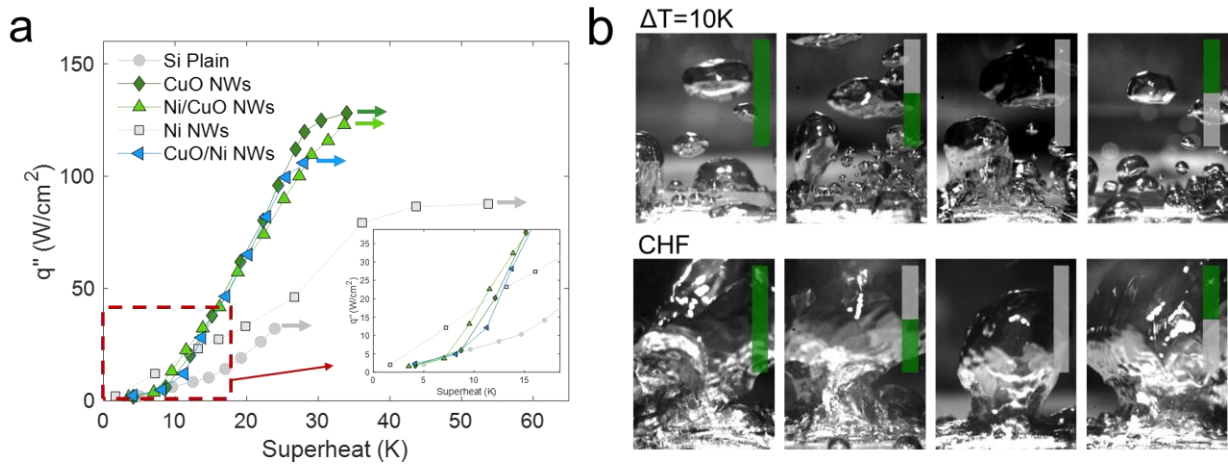
Figure 3.13. Pool boiling heat transfer of the segmented NWs. (a) The boiling curve shows heat fluxes of the segmented NWs and plain Si surface. The inset boiling curves shows a magnified view of the boiling curve at the superheat from 0 K to 17 K. The HTC is defined by $h = q''/\Delta T$ where q'' is the heat flux and ΔT is the superheat. The Ni/CuO NWs clearly exhibits as large CHF as CuO NWs with enhanced HTC at ΔT=10K. (b) Bubble dynamics are captured by high-speed camera at 2,000 fps. The images show bubble dynamics at ΔT=10 K and CHF for CuO NWs, Ni/CuO NWs, Ni NWs, and CuO/Ni NWs, respectively. At ΔT=10 K, bubbles are not rigorously generated for CuO NWs and CuO/Ni NWs due to the hydrophilic property of top CuO portion. In contrast, bubble is rigorously generated on Ni/CuO NWs with smaller departure droplet radius at ΔT=10 K. Correspondingly, nanowire arrays with hydrophobic top Ni shows higher heat fluxes at low superheat condition as we expected.

3.4. Summary of the Chapter

In this study, we demonstrate the design of vertically aligned NWs with heterogeneous property to improve both CHF and HTC simultaneously for boiling two-phase heat transfer. The heterogeneous properties successfully realize the hydrophobic surface wettability while maintaining efficient capillary-driven liquid transport by the design of segmented NWs. As a result, segmented NWs with hydrophobic portion over hydrophilic portion offer 250% enhancement of HTC comparing to plain Si *via* efficient bubble dynamics in nucleation boiling regime at low superheat (ΔT = 10K). Furthermore, the CHF is achieved to be q''_{CHF} =122.9 W/cm^2 for the segmented NWs owing to the efficient capillary-driven liquid transport through bottom hydrophilic portion. We observe that segmented NWs with hydrophobic portion on top (Ni/CuO NWs) show about 50° of contact angle, which is between pure hydrophilic CuO NWs (~20°) and hydrophobic Ni NWs (~110°) due to the hemi-spreading behavior. Wicking performance is significantly improved for Ni/CuO NWs comparing to CuO/Ni NWs and Ni NWs because bottom hydrophilic portion interacts with bottom layer that create large capillary pressure. Furthermore, two-step liquid transport is observed on Ni/CuO NWs owing to the heterogeneous wettability, which indicates efficient capillary-driven liquid replenish and liquid transport to hydrophobic layer placed above. We anticipate that the understanding the liquid transport and two-phase heat transfer on the engineering surfaces with heterogeneous properties elucidated in this study can provide design rule of the advanced thermal management system.

CHAPTER 4: Liquid Transport through Hierarchically Porous Constructs

Designing optimum porous structures for efficient liquid transport has been challenging due to two competing factors that are permeability and capillarity. This issue might be addressed by the rational design of hierarchically porous constructs that suggest sufficiently large liquid pathways from the upper-level hierarchy as well as capillary pressure enabled by the lower hierarchy. In this paper, we demonstrate hierarchically porous copper scaffolds utilizing a new class of self-assembled soft materials, called bicontinuous interfacially jammed emulsion gels (bijel). The use of bijel as a sacrificial template enables the unique combination of unprecedented control over both micropores and nanopores in a regular, uniform, and continuous arrangement, which promises efficient liquid transport through them. The optical experimental measurements about dynamic droplet topologies confirm that the hierarchically structured copper scaffold with nanoscale pores showing a superior wicking performance to the copper scaffolds with plain surface or commercially available sintered copper particles. The role of nanoscale morphology in liquid infiltration mechanisms is further investigated through microscopic optical observations via environmental scanning electron microscopy, in which the wetting through the nanopores occurs at the beginning followed by the liquid transport through the micropores. The use of hierarchically porous media will enable performance breakthroughs in interfacial applications ranging from battery electrodes, cell delivery in biomedical devices, to capillary-fed thermal management systems.

4.1. Background

Liquid transport through porous media has drawn great interest in the scientific community due to its importance in diverse applications such as oil separation,[103,104] battery technologies,[105–109] catalysis,[110,111] and thermal management.[85,112–114] Especially, microscale porous metals have been featured due to their unusual combination of high specific surface area, thermal conductivity and liquid permeability. Among multiple properties, liquid transport through porous media by capillary action is crucial to improve two-phase heat transfer performance.[6,94,115] The continuous liquid replenish driven by the capillary action prevents surface dry-out resulting in enhancement of two-phase heat transfer. For example, various types of porous structures, such as microposts, copper inverse opals, and vertically aligned nanowires, have been suggested and studied to optimize the liquid permeability along with their surface geometry and morphology.[3,5,6,8,18,37,116] However, the liquid transport properties of the engineering surfaces with homogeneous morphology have been limited because of two competing factors at play in capillary wicking: permeability and capillarity.[14,15] When a liquid percolates through the void matrix of porous structures, larger pores can provide permeabilities with smaller hydraulic resistances, whereas smaller pores may increase capillary-driven transport.[22,23,30–34]

The liquid transport in porous media can be much improved by the spatial optimization of multiscale transport mechanisms using hierarchical surfaces. For example, microscale pores can be utilized to provide a large permeability for the liquid transport, while nanoscale pores or surface roughness can serve to enhance capillarity, which is inversely proportional to the pore size.[93] Due to the potential of hierarchically structured surfaces to overcome the competing effect of the permeability and capillarity, different types

69

of hierarchical porous media have been suggested where the examples include the combination of metal particle sintering, multiple dealloying of metallic mixtures, and chemical oxidation.[50,51,117] However, most of the previous fabrication methods could not succeed in independently engineering pore size, arrangements or their hierarchy.[40,43–49,118] The irregularity of pore morphology often deteriorates fluid permeability through the hierarchical morphology.[31,119,120]

Recent advances in templated fabrication of materials using bicontinuous interfacially jammed emulsion gels (bijels) have opened new means toward hierarchically porous media with highly tunable, regular, and continuous pore structure.[121–124] Bijels are a novel type of soft material formed by arresting spinodal decomposition of two immiscible fluids using neutrally wetting colloidal particles. Using standard processing techniques, bijels can be converted to composite and porous materials with microstructure akin to a morphology of spinodal decomposition.[125,126] Due to the unique bicontinuous morphology of bijels derived from the spinodal decomposition, they have been suggested to be used in various applications such as hydrogels for cell delivery, electrodes for a capacitor, sensors and solid catalysts.[125,127,128] First, porous materials derived from bijels enjoy a fully interconnected pore phase with uniform domain size and low structural tortuosity, resulting in the large permeability.[31,128–130] Importantly, the hierarchy of the bijel-templated porous scaffold could be engineered easily by manipulating the pores in different length scales independently. The pore size in bijel-templated porous scaffolds can be controlled ranging from ten micrometers to hundreds of micrometers by simply changing colloidal volume fraction, which will eventually determine the 1st order microscale pores of the bijel-templated porous metal.[125] Despite the promising capability of the bijel-

templated porous metals in terms of permeability, liquid transport behavior through the porous metals is not yet explored. In addition, systematic investigation of liquid transport through hierarchically porous metal has been limited due to the difficulties in fabrication of the porous metals with precisely controlled 2nd order morphology (such as pores and roughness) while maintaining morphology of 1st order pores determining permeability. Thus, liquid transport has been mainly explored in terms of liquid permeability by controlling surface geometry such as micropillars' distance, density, or height.[61,131,132]

In this study, we demonstrate three-dimensional (3D) hierarchically porous metal scaffolds derived from bijels, with the aim of investigating how hierarchical porosity affects liquid infiltration through these materials. Importantly, the bijel-templated metal scaffolds offer two unique characteristics salient to liquid infiltration: 1) regular and continuous liquid pathways offering large permeability, and 2) capability to independently control the size of micropores while maintaining a uniform size distribution within each set. These unique characteristics allow us to systematically design hierarchical porous media and investigate their liquid imbibition characteristics by performing dynamic droplet imbibition process into bijel-derived copper scaffolds with precisely controlled nanoscale morphology while the micropores remain unchanged.[133] This information will be further explained by using a capillary penetration model that categorizes the droplet imbibition process with increasing, constant, and decreasing contact area of droplets with dynamic contact angle. In addition, we use digital imaging with micrometer resolution to directly visualize the dynamics of liquid wicking through the hierarchically porous copper scaffolds in a saturated environment and better understand the liquid transport mechanisms at play.

4.2. Experimental Method

4.2.1. Silica Nanoparticles Preparation

Fluorescent modified silica nanoparticles with neutral wettability are prepared by modified Stöber process. 12.5 mg of Rhodamine B Isothiocyanate (RITC, Sigma Aldrich) dye is first conjugated with 26.3 μl Aminopropylthirethyloxisilane (APTES, Sigma Aldrich) in 10 ml of anhydrous ethanol (EtOH, Sigma Aldrich) under mixing for 24 hours. Then the silica nanoparticles are synthesized by Stöber process using dye conjugated APTES and tetraethyl orthosilicate (TEOS, Sigma Aldrich). 10 ml of strong ammonia (Sigma Aldrich), 4180 μl of TEOS, and 5 ml of prepared dye conjugated APTES are mixed in anhydrous EtOH for 24 hours. The synthesized silica nanoparticles are washed with deionized water repeatedly for three times by centrifuge for 12 min at 2500 rpm followed by drying in vacuum oven at 120 °C for 24 hours. The size of the silica nanoparticles is 760 nm with narrow size distribution as shown in Figure 4.1.

759 ± 25 nm

Figure 4.1. Silica nanoparticles fabricated *via* modified Stöber process. The silica nanoparticles are around 760 nm in diameter with narrow size distribution.

4.2.2. Fabrication of Bijel-Templated Polymer Scaffolds

Bijels are formed by phase separation of two immiscible liquid above the LCST and are used as a template for the polymer scaffold. Bijels are prepared by following four steps: 1) mixture preparation, 2) phase separation, 3) monomer exchange, and 4) UV curing. The colloidal solution is prepared by mixing DI water (milli-Q water) and 2,6-Lutidine (99%, Sigma Aldrich) in near critical composition ($\chi_{Lut} \approx 0.064$) with 10% (v/v) of silica nanoparticles. The silica nanoparticles are dispersed in the solution through both ultrasonic horn for 10 sec and an ultrasonic bath for 5 min (Branson Sonifier 250, USA) for three cycles. To form the film-like polymer scaffold, 100 μl of mixture is dispensed in a vertical square mold (1.5 cm × 1 cm × 1 mm). Once the mixture is placed in the mold without any trapped gas, the phase separation is performed in two steps using microwave and oven. For the instant phase separation, the mixture is first heated up by microwave for 20 sec and then moved to the oven to prevent remixing of the fluids and dwell until the spinodal decomposition is stabilized. In the monomer exchange step, 20 μl of poly(ethylene glycol) diacrylate (PEGDA, Mw= 258 g mol^{-1}, Sigma Aldrich) is carefully added at the top of the bijel and rest for 2 hours until the monomer fully diffuses into the oil phase exclusively. The monomer is premixed with photoinitiator, 2-hydroxy-2-methylpropiophenone (Darocur 1173, Ciba Specialty Chemicals). The exchanged monomer is cured by a spot cure system (Omnicure S1, Lumen Dynamics, Canada) for 5 min, which will be later removed. Bijels are washed by water and isopropyl alcohol are dried in atmospheric condition for overnight. The silica nanoparticles on the polymer scaffold are removed by HF etching.

4.2.3. Fabrication of Bijel-Templated Copper Scaffolds

The copper deposition is performed by using electroless deposition method. Before this, the scaffold is activated by catalyst deposition. The polymer scaffold is immersed in the sensitizer solution which composed of the tin (II) chloride salt ($SnCl_2$, 98%, Sigma Aldrich), hydrochloric acid (HCl, 37%, Sigma Aldrich) and DI water and rinsed by DI water. Then, the polymer scaffold is transferred to the activator solution which composed of palladium (II) chloride salt ($PdCl_2$, 99%, Sigma Aldrich), hydrochloric acid (HCl, 37%, Sigma Aldrich) and DI water. The immersion time into the sensitizer and activator solution is varied from 30 min to 90 min. The solution of copper electroless plating is prepared by adding 120 mg of copper (II) sulfate pentahydrate (99%, Alfa Aesar), 540 mg of ethylenediaminetetraacetic acid tetrasodium salt (EDTA, Alfa Aesar), 0.2 mg of 2,2'-dipyridyl (99%, Alfa Aesar), 1 mg of poly(ethylene) glycol (M_n=1000 g mol^{-1}, Sigma Aldrich), and 60 mg of sodium hydroxide (NaOH, Alfa Aesar) into 10 ml of DI water. The temperature of the solution is set to 70 °C and the activated polymer scaffold and 400 μl of formaldehyde (HCHO, 37 w/w%, Alfa Aesar) is added to the solution to initiate the electroless plating. The reaction is carried out under stirring for 1 hour.

During the calcination process in the furnace, the polymer scaffold is removed as a sacrificial template and the metal nanoparticles deposited on the scaffold are interconnected. The calcination process is stabilized at 300 °C for 60 min in air condition. After stabilization, the temperature increases to 500 °C and isothermal for 120 min in air condition. The minimum sintering temperature is set to be above 420 °C for the copper scaffold without

carbon residue from the polymer template.[128] All temperature ramp is 10 °C/min. For the copper scaffold calcination, the temperature is changed and maintained to 470 °C or 600 °C for 120 min in Ar condition and another 120 min in a forming gas (5% of H_2 and 95% Ar). For the nickel scaffold calcination, the temperature is changed and maintained to 470 °C for 60 min in Ar condition and 120 min in the forming gas. Once the calcination is finished, the copper scaffold is removed from the furnace after the tube temperature is naturally cooled down to room temperature.

Table 4.1. Fabrication details of bijel-derived metal scaffolds.

Sample names	Activation time (min)	Deposition temperature (°C)	HCHO concentration (M)	Calcination temperature (°C)
$CuPP_n$	30	85	0.5	450
$CuPP_m$	90	75	1	600
$CuPR_h$	60	75	1	600
$CuPR_l$	90	75	0.5	600
CuPS	60	75	0.5	600

4.2.4. Liquid Infiltration Test

Wetting property and liquid infiltration is investigated via a sessile droplet method with a goniometer (MCA-3, Kyowa Interface Sciences). The goniometer with 75 μm diameter dispenses 10 nl of DI water by 10 kPa of air pressure. The droplet imbibition is captured by a high-speed camera with 5,000 fps. The diameter and contact angle are analyzed for every frame (0.2 ms) before the droplet is fully depleted.

4.2.5. Environmental Scanning Electron Microscopy

Surface morphology is investigated by a scanning electron microscopy (SEM) using FEI Magellan 400 at 15 kV of accelerating voltage. The water wetting of the hierarchically structured copper scaffold is captured by environmental SEM (ESEM) using Quanta 3D at 30 kV of accelerating voltage. The copper scaffold is mounted on the stage and maintain the spacing by carbon tape to prevent direct condensation on the copper scaffold. The Peltier cold stage temperature is set to 3.8 °C at P_v=8 mbar. Then the vapor pressure in the chamber increases to P_v=11 mbar to initiate the condensation on the stage. The neutral wettability of the silica nanoparticles is checked by using confocal microscope (VisiTech International, UK).

4.3. Results and Discussion

4.3.1. Design of Hierarchical Morphology and Structural Characteristics

Bijel-templated, hierarchically designed copper scaffolds are fabricated using established bijel processing protocols the entail the preparation and subsequent metallization of a microporous polymer scaffold from a bijel. The polymer scaffold preparation steps are illustrated in Figure 4.2a, and include mixture preparation, phase separation, monomer exchange, and UV curing in series. Figure 4.2b schematically shows the corresponding microstructures after each fabrication step. We use a critical mixture of two immiscible liquids (water and 2,6-lutidine) for phase separation at lower critical solution temperature (LCST), as indicated in Figure 4.2c.[134] Then the silica nanoparticles which have near-neutral wettability with respect to a water and 2,6-Lutidine are dispersed into the mixture. As shown in Figure 4.2d, the false-colored confocal microscope image confirms the spinodal-like microstructure of the resulting mixture, arrested by nanoparticle jamming at the liquid interfaces. After this, the bijel is templated *via* monomer exchange and selective curing for the polymer scaffold fabrication, where the crosslinking density of the polymer scaffold is controlled by how many times the monomer exchange process is repeated.[135] Note that the crosslinking density of the polymer scaffold determines the morphology and quality of metal scaffolds. A high crosslinking density is used to create shell-like structures by preventing the penetration of the ion into the polymer scaffolds elsewhere.[135] On the other hand, a low crosslinking density makes it possible to metal particles to nucleate through the polymer template (Figure 4.4h). As a result, nucleation seeds on the low crosslinking polymer scaffolds enable metal deposition as particle form afterward. Figure 4.2e shows a SEM image of the resultant scaffold after UV curing, confirming its overall

spinodal-like morphology with microscale pores. See Experimental section for the details about fabrication steps and synthesis of silica nanoparticles (Stöber method).
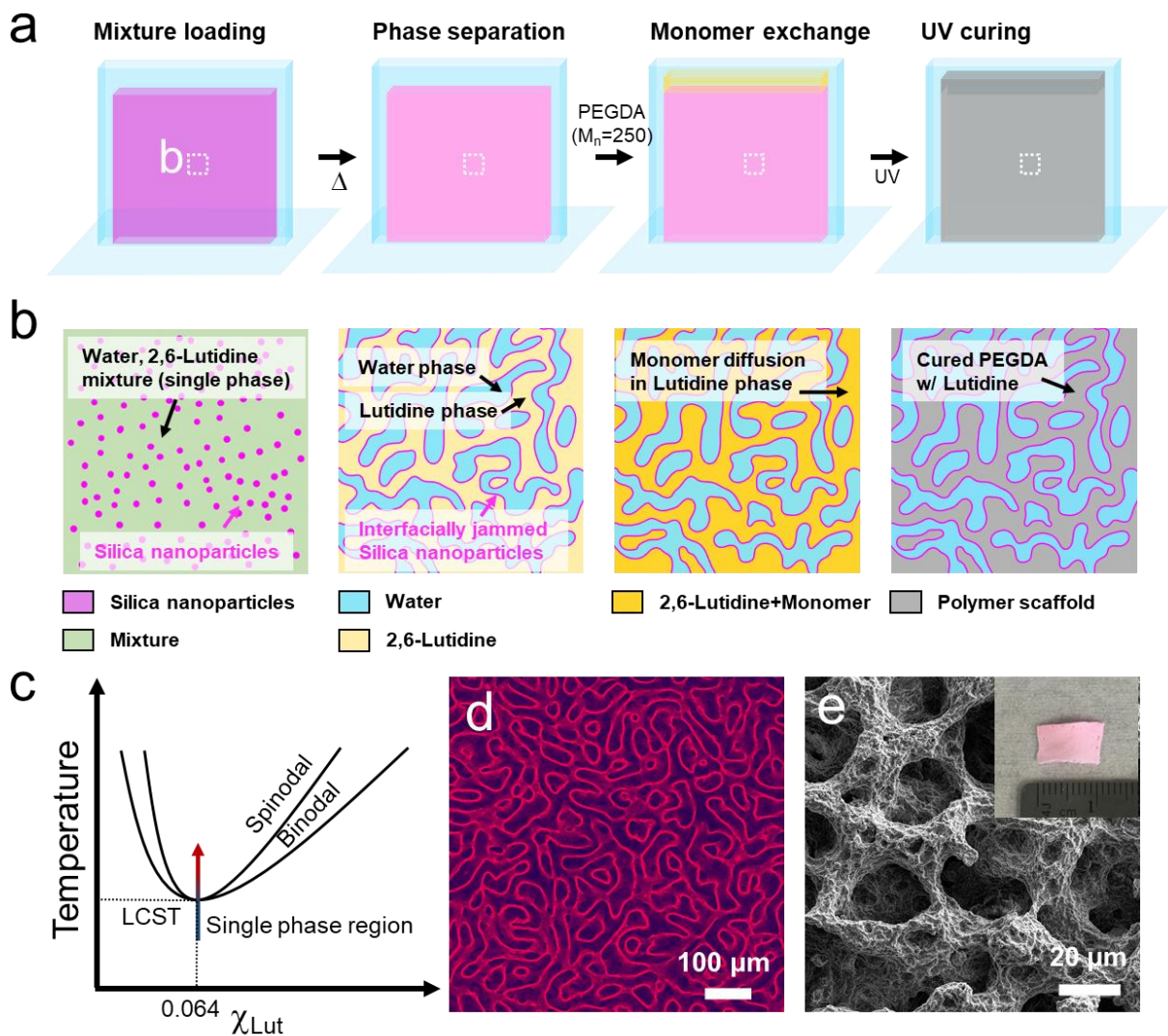
Figure 4.2. Preparation of bijel-templated polymer scaffold. (a) The fabrication steps for creating the polymer scaffold: mixture preparation, phase separation, monomer exchange, and UV curing using a vertically placed glass cuvette mold. (b) The illustrations show the corresponding detailed morphology of the structure after each step. (c) The water-lutidine mixture is separated at a lower critical solution temperature (LCST) with the critical composition where the mole fraction of 2,6-lutidine χ_{Lut} =0.064. (d) The false-colored confocal microscopic image confirms the arrested spinodal decomposition. The pink and black region represents water and oil phase, respectively. (e) The scanning electron

microscope (SEM) image shows the spinodal-like morphology of the polymer scaffold after the UV curing. The inset shows the photograph of a sheet-shaped polymer scaffold.
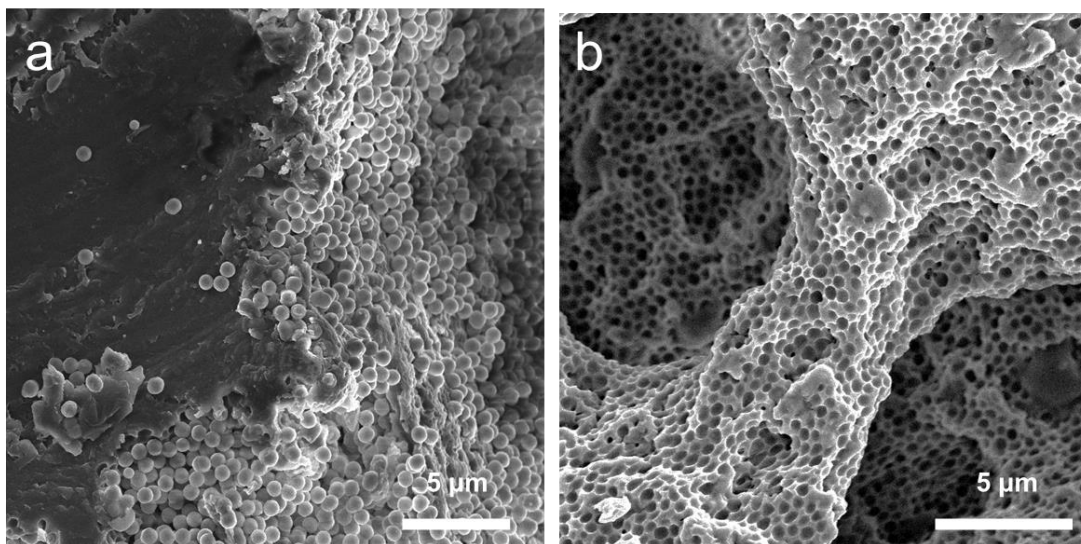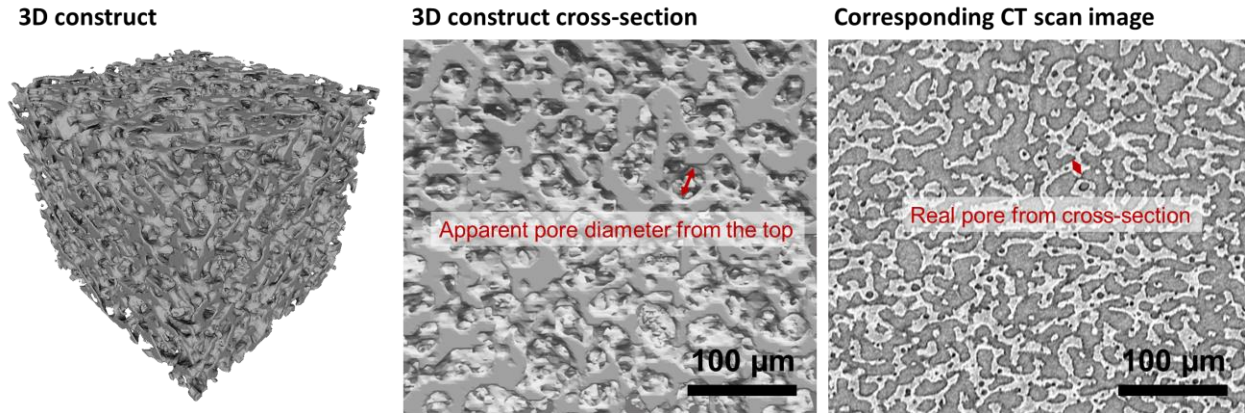

Figure 4.3. Cross-sectional SEM image of the polymer scaffold before and after HF etching. (a) The SEM image clearly shows the alignment of the silica nanoparticles in between the polymer region and void region. (b) Silica nanoparticles are removed by HF etching resulting in rough surface on polymer scaffolds.

The polymer scaffolds are further used to create hierarchically porous copper scaffolds at two widely separated length scales by following established protocols. As shown in Figure 4.6a, after the silica nanoparticles are removed, the polymer scaffold maintains its original morphology consisting of the continuous domain with a micropore diameter of approximately 16 μm, as determined by confocal microscope and CT-scan as shown in Figure 4.2d and Figure 4.4. When the polymer scaffold is activated by sensitizer solution ($SnCl_2$) and activator solution ($PdCl_2$), we observe that the polymer scaffold is swollen, which enables the metal to be deposited within the polymer phase (Figure 4.2b). After electroless deposition, the pore size of the copper scaffold increases due to the metal deposition into the polymer phase, which is maintained during the following drying process (Figure 4.2e). The

copper scaffold shrinks back to the original size by removing the polymer template during the calcination process (Figure 4.2c), leading to the original size of micropores (Figure 4.2f).

Figure 4.4. 3D construct of bijel-templated polymer scaffolds. A cross-sectional image of the 3D construct shows apparent pore size as the same way to measure pore size from SEM images. Corresponding cross-sectional image obtained from CT-scan shows uniform domain size.
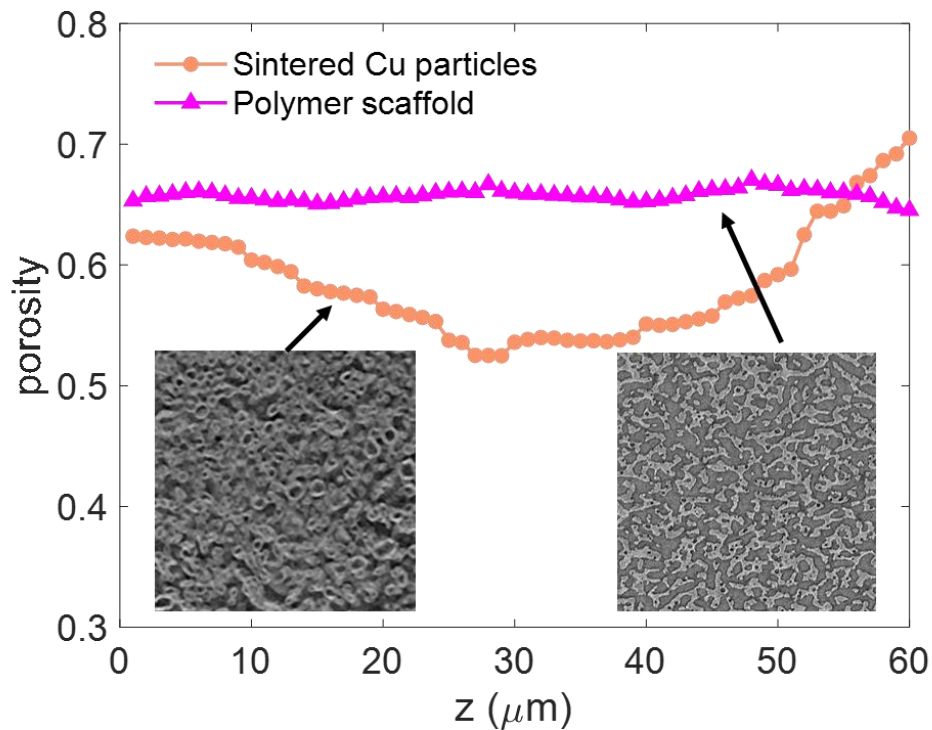
Figure 4.5. Porosity comparison between sintered Cu particles and bijel-templated polymer scaffold. Inset CT-scan images show a cross-section of the sintered copper

particles (left) and the polymer scaffold (right). The bijel-templated polymer scaffolds offer uniform porosity over the sample height.

The 2nd order nanoscale morphology before and after the metal deposition is demonstrated by the presence of the silica nanoparticles arrested and copper nanoparticle nucleation. Figure 4.6g shows the polymer scaffold surface after the silica nanoparticles are fully removed, which confirms the location where the silica nanoparticles are arrested between water and lutidine phases (Figure 4.4). The rough surface might impact the electroless metal deposition in the following step by facilitating catalyst-surface interaction through an extended surface area. During this electroless metal deposition, copper nanoparticles are formed, as evident in Figure 4.6h where the nanoparticle morphology (e.g., size or distribution) is influenced by the combination of precursor deposition time and agent concentration (see Experimental section for details). Eventually, the copper nanoparticle morphology impacts the level of hierarchy of bijel-derived porous media after calcination step. The calcination process removes the polymer scaffold and sinters copper particles to be interconnected, which alters the 2nd order morphology (Figure 4.6i). In this process, a lower calcination temperature can produce smaller 2nd order pores. This is because elevated temperatures accelerate the coarsening and merging of copper nanoparticle clusters into dense filaments, eventually forming larger 2nd order pores. This observation is fully consistent with previous studies that explain the creation of the 2nd order pore size ranging from sub-micrometers to micrometers by changing the calcination temperature and duration from 470°C to 600°C .[126,128]
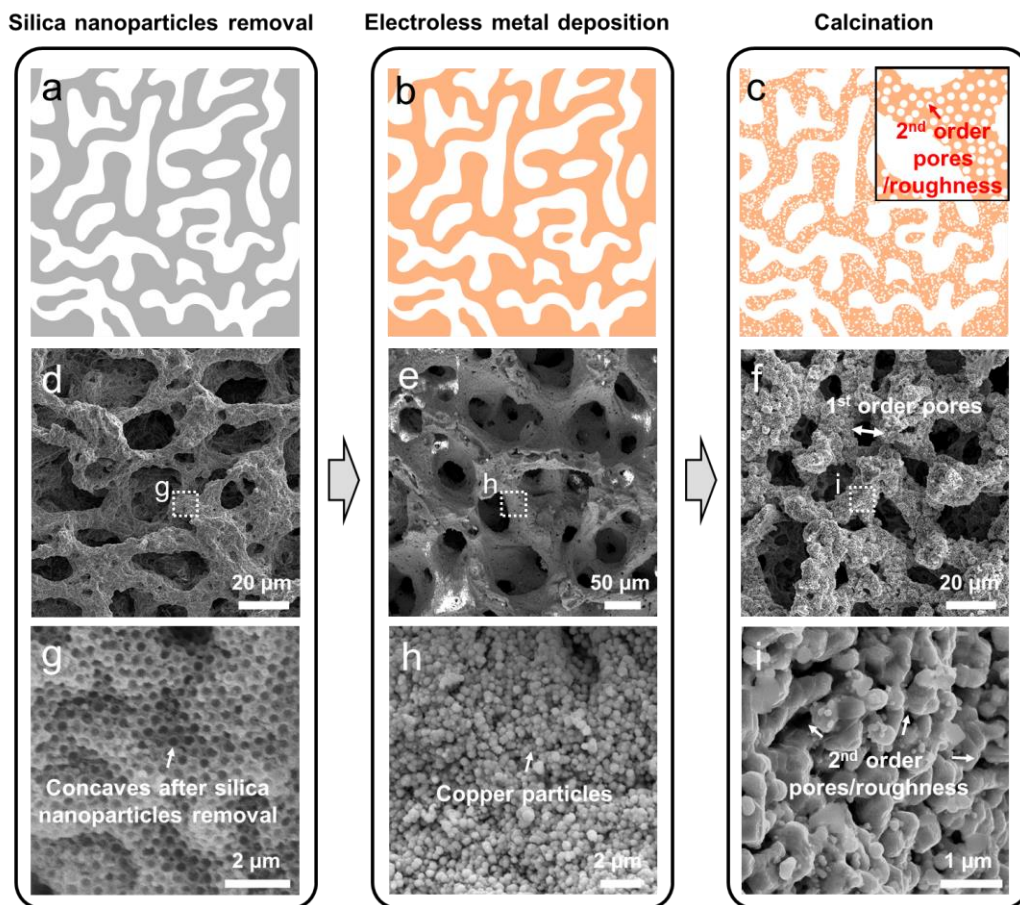
Figure 4.6. Preparation of bijel-templated copper scaffolds. (a) The silica nanoparticles arrested between water-rich and lutidine-rich phases are dissolved by using HF solution. (b) The polymer scaffold is templated by using electroless deposition method. (c) The calcination process removes the polymer template and sinters copper particles. The representative SEM images (d-f) and close-up images (g-i) show the corresponding detailed morphology of the copper scaffold after each step. The microscope details confirm the formation of hierarchical morphology, which consists of 1st order micropores and 2nd order nanopores or roughness.

To investigate the role of the structural hierarchy in capillary wicking, we create the copper scaffolds by independently manipulating the 2nd order structure (see Experimental for details), while the 1st order pores derived from our bijel-templating technique possess the uniformity and continuity of their bijel parents. Therefore, the tunable descriptor in this study is 2nd order structure that includes pores, roughness, and smooth surface, represented by P, R, and S respectively. The subscript n, m, h, and l denote nanoscale, microscale, high, and low, respectively, in Table 4.2 and Figure 4.7. For example, the copper scaffold with 2nd order nanoscale pores (CuPP$_n$) is created by the low temperature calcination process at 470 °C that partially interconnect copper nanoparticles, as shown in Figure 4.7a and 4.7f. On the other hand, copper nanoparticles are fully interconnected or integrated during the calcination process at a high temperature at 600 °C, resulting in the copper scaffold with microscale pores, surface roughness and smooth surface. As shown in Figures 4.7b and 4.7g, the copper scaffold with microscale pores (CuPP$_m$) composed of 2nd order microscale pores (~5 µm) that is distinctively distinguished to the 1st order microscale pores (~20 µm). The copper scaffolds with surface roughness are named CuPR$_h$ (Figures 4.7c and 4.7h) and CuPR$_l$ (Figures 4.7d and 4.7i) where the R$_h$ and R$_l$ represent high and low roughness, respectively. Finally, the sample CuPS is the copper scaffold with a smooth surface (Figures 4.7e and 4.7j).

Table 4.2. Details of the bijel-templated copper scaffolds with varying morphology.

Sample names	1st order structure	1st order pore size (µm)	2nd order structure	2nd order pore size (µm)
CuPP$_n$	Spinodal-like	21±7	Nanoscale pores	0.2
CuPP$_m$	Spinodal-like	20±6	Microscale pores	5.1
CuPR$_h$	Spinodal-like	22±5	High roughness	-
CuPR$_l$	Spinodal-like	23±6	Low roughness	-
CuPS	Spinodal-like	21±4	Smooth surface	-
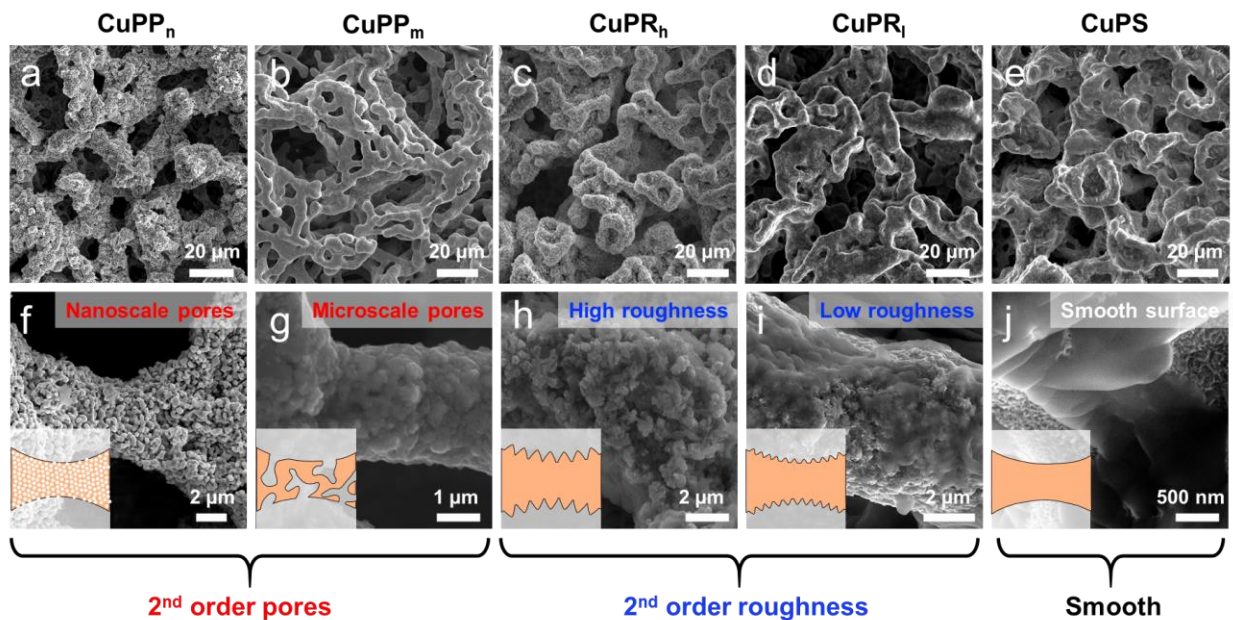
Figure4.7. Representative images of the bijel-templated copper scaffolds with varying morphology. The 1st order pores with spinodal structures are reserved for the copper scaffolds with the 2nd order (a, f) nanoscale pores (CuPP$_n$), (b, g) microscale pores (CuPP$_m$), (c, h) high roughness (CuPR$_h$), (d, i) low roughness (CuPR$_l$), and (e, j) smooth surface (CuPS). Inset illustrations show the structural details for the 2nd order morphology of the copper scaffolds.

4.3.2. Droplet Imbibition and Liquid Infiltration

We analyze capillary wicking through the copper scaffolds by studying the capillary penetration model that explains droplet imbibition into porous media.[98–101] The model by Hilpert and Ben-David[133] explains the imbibition of small droplets into a porous medium consisting of parallel cylindrical capillary tubes, by identifying three different phases: increasing drawing area (IDA), constant drawing area (CDA), and decreasing drawing area (DDA). As shown in Figure 4.8a, the droplet first spreads over the surface with an increase in contact radius R_d until the contact angle reaches advancing contact angle θ_a, called the IDA phase. Then, R_d remains constant while the contact angle decreases in the

84

second phase, referred to as the CDA phase. The contact angle of the droplet in the CDA phase decreases until it becomes equal to the receding contact angle, θ_r, for the system studied. Lastly, the droplet is fully infiltrated into the porous medium, and both the radius and contact angle of the droplet accordingly decrease, in the DDA phase.
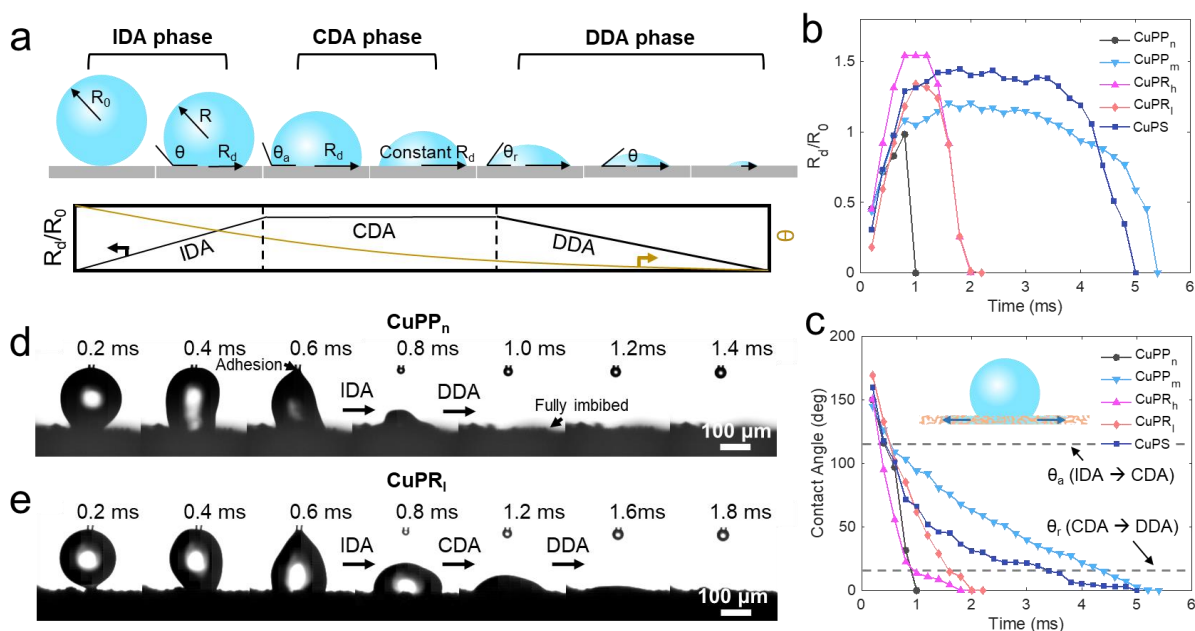
Figure 4.8. Droplet imbibition phenomena into bijel copper scaffolds. (a) Schematic illustrations show three liquid infiltration phases: 1) increasing drawing area (IDA) phase, 2) constant drawing area (CDA) phase, and 3) decreasing drawing area (DDA) phase. This droplet imbibition phenomena into the copper scaffold are analyzed by (b) the contact radius R_d normalized by the initial droplet radius R_0 and (c) contact angle θ as a function of time. The representative images of sessile drops captured by a high-speed camera show the infiltration behaviors by using (d) CuPP$_n$ and (e) CuPR$_l$.

We test the library of copper scaffolds to understand the relationship between morphological hierarchy and droplet imbibition behavior. In our experiments, the normalized contact radius R_d/R_0 is monitored as a function of time to identify the three phases of the capillary penetration model, where R_0 is the initial droplet radius. The plot in

Figure 4.8b shows that R_d/R_0 behaves as expected from the model, increasing in the IDA phase, remaining constant in the CDA phase, and decreasing in the DDA phase. The IDA phase for most of the copper scaffolds lasts for approximately the same duration ($\sim$ 1.0 ms), regardless of the 2nd order pore morphology. For the CuPP$_n$ with 2nd order nanopores, the CDA phase is not clearly observed, showing a nearly instant transition from the IDA to the DDA phase. In the DDA phase for the CuPP$_n$, the droplet is imbibed into the porous structure within 0.2 ms. The 2nd order roughness group (CuPR$_h$ and CuPR$_l$) show that the CDA phase lasts for 0.6 ms, indicating slower liquid imbibition than the bi-porous structures with 2nd order pores (CuPP$_n$ and CuPP$_m$). For the copper scaffold with smooth surface (CuPS), the CDA phase duration or droplet depletion time increases up to $\sim$ 3.6 ms or 5.0 ms, respectively, which is five times larger than those of the CuPP$_n$. Even though our experiments show an evidence of the three capillary infiltration phases from the theoretical model, CuPP$_n$ does not show CDA phase because of superior liquid infiltration performance magnifying effect of adhesion against capillary tip (Figures 4.8d-e). Furthermore, inherent to all materials derived from spinodal decomposition, the pores of the copper scaffolds in this work are interconnected in all directions, resulting in both vertical liquid transport and radial wicking through the structure. It should be noted that, as the sample thickness (<70 μm) is thinner than droplet diameter, radial wicking may be a more important mechanism of liquid transport than vertical infiltration in our systems.

The real-time contact angles are also recorded during the droplet imbibition, as plotted in Figure 4.8c. Based on the theoretical model, the transitions from the IDA to the CDA phase and from the CDA to the DDA phase occur when the contact angles become θ_a and θ_r, respectively. Our experimental results show that the θ of the copper scaffolds

decreases once the droplet contacts to the surface and then is separated when the contact angle becomes θ_a = 118°, which agrees well with the imbibition model. In addition, for all copper scaffolds, the decrease in the contact angle slows down once θ reaches θ_r = 15° until the droplet is fully depleted. This means that the dynamic contact angle is insensitive to the 2nd order porosity or surface roughness in our system. A possible explanation for this behavior would be that the copper scaffold becomes saturated by the liquid before the CDA phase. The wicked volume that is greater than the required volume to fill the porous structure underneath the droplet indicates the prewetting state (Figure 4.10a). Therefore, the dynamic contact angle is determined by the spinodal morphology of the microscale 1st order pores leading to the constant θ_a and θ_r in our experiments.
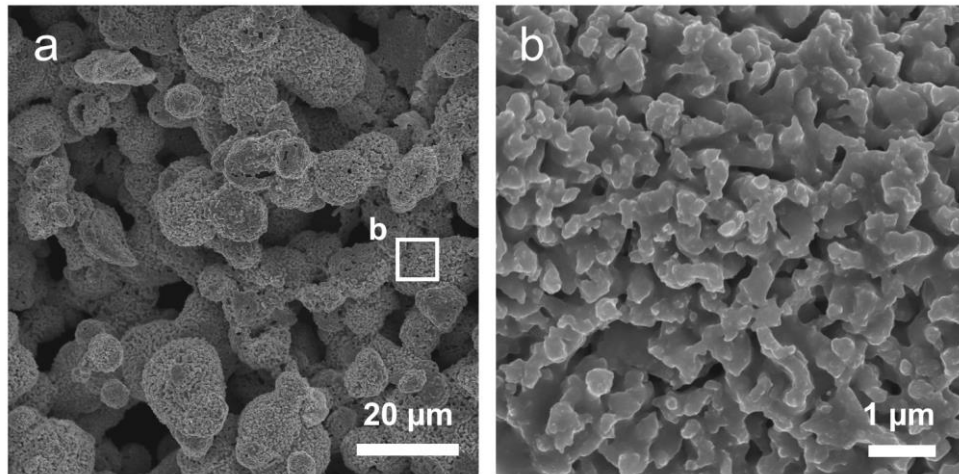
Figure 4.9. SEM images of the sintered copper particles. The sintered copper particles are prepared by sintering process in the furnace at 800 °C. The sintered copper particles are well interconnected allowing high permeability. The sintered copper particles possess the 2nd order nanoscale pores.

4.3.3. Wicked Volume Flux

To examine the liquid transport rate into the metal scaffold during droplet imbibition, the volumetric flow rate of the droplets is investigated by calculating the wicked volume flux $\dot{V}''$ this descriptor shows how porous media can be effective under two phase environments. Upper limit of heat flux of boiling heat transfer or critical heat flux is directly related to $\dot{V}''$ as capillary-driven liquid transport replenish liquid into boiling surfaces preventing dry-out.[60] Once the droplet is stabilized without vibration after it detached from the capillary tip, the volume of the spherical cap V_f is calculated by the following equation:

$$V_f = \frac{\pi}{3} \left(\frac{R_d}{\sin \theta} \right)^3 (2 + cos\theta)(1 - \cos \theta)^2 \qquad (4.1)$$

where V_f is related to the original volume of the droplet V_0, the droplet volume above the surface V_f, and the wicked volume into the porous structures V_p through $V_0 = V_f + V_p$. Then the wicked volume flux $\dot{V}''$ is calculated as

$$\dot{V}'' = \frac{1}{A_d} \left(\frac{dV}{dt} \right) \qquad (4.2)$$

where $A_d = \pi R_d^2$ is the drawing area. We calculate the $\dot{V}''$ from the results during the CDA phase because the $\dot{V}''$ increases before 0.8 ms as R_d increases in the IDA phase (Figure 4.10). The copper scaffold with nanoscale 2nd order pores (CuPP$_n$) shows three times larger $\dot{V}''$ than the scaffold with 2nd order roughness (CuPR$_h$ and CuPR$_l$) and at least four times larger than the copper scaffold with micropores (CuPP$_m$) and plane surface (CuPS), which suggests greater boiling performances in these materials. As a reference to this measurement, we also prepared sintered copper particles that are commercially used for boiling surfaces (Figure 4.9 and Figure 4.11). The hierarchical bi-porous scaffold shows higher $\dot{V}''$ than the sintered

copper wick by 191%, suggesting promising performances in two-phase applications.[6,114]

The higher $\dot{V}''$ of the bijel-templated scaffolds could be explained by the unique characteristics of the spinodal morphology, leading to constant pore size distributions and interconnecting pathways.[136,137] These characteristics result in low tortuosity ($\tau \sim 1.30$) for the morphology derived from spinodal decomposition, whereas τ can be as high as 1.73 for randomly porous scaffolds such as the sintered copper wick used here.[136] This suggests two times higher permeability K based on the modified Kozeny-Carman equation ($K \sim \tau^{-2}$).[138,139]
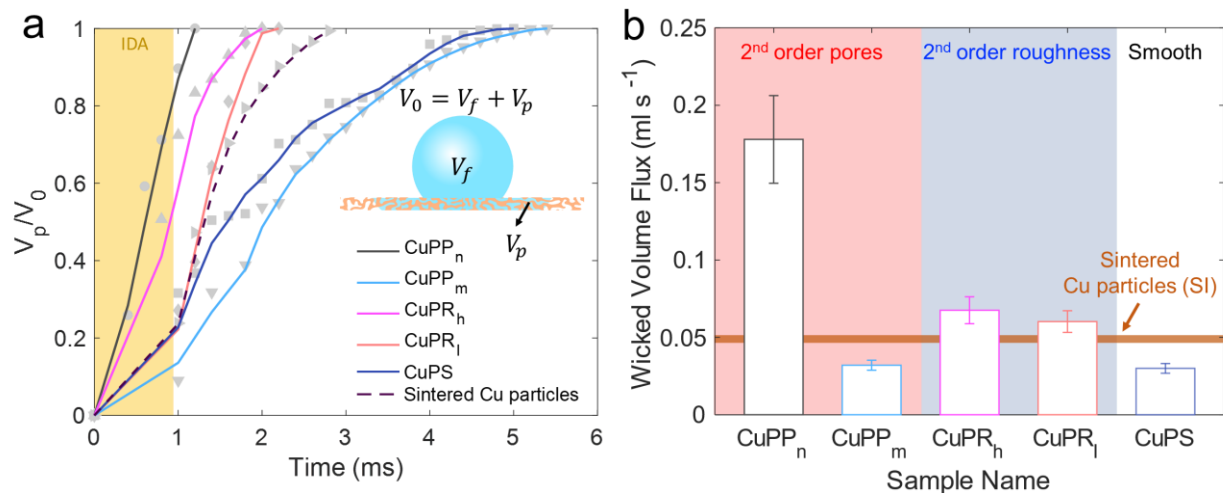
Figure 4.10. Normalized wicked volume V_p/V_o and wicked volume flux $\dot{V}''$. (a) Time-dependent normalized wicked volume V_p with respect to original droplet volume V_o is calculated by measuring changes in droplet volume V_f based on spherical cap assumption. (b) The wicked volume flux is calculated based on the V_p and A_d for the copper scaffolds. The $\dot{V}''$ of the CuPPn and the CuPRh clearly show that the hierarchically structured surface improves liquid infiltration performance. In contrast, the copper scaffolds with plain surface show the $\dot{V}''$ less than 50 % of the scaffolds with nanoscale pores or roughness. The brown line indicates the wicked volume flux through the reference sample consisting of sintered Cu particles.
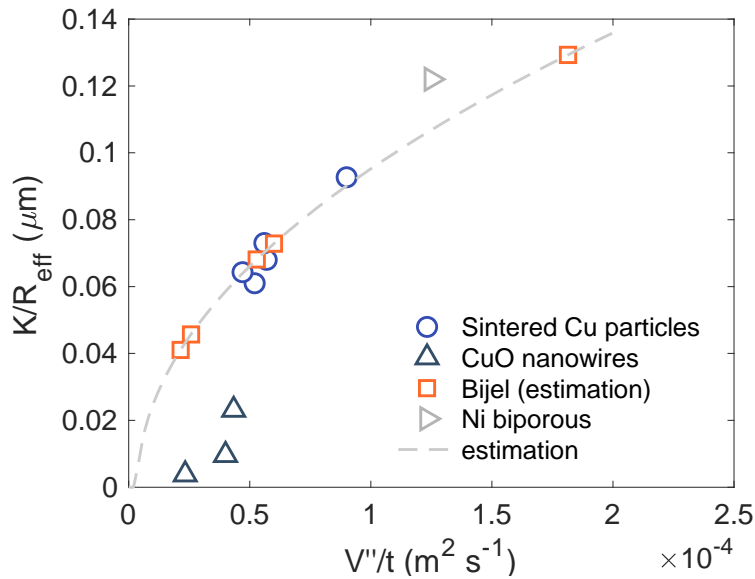
Figure 4.11. Empirical correlation of the wicked volume flux and capillary performance parameter (K/R_{eff}). The wicked volume flux is divided by the thickness of the porous media, and the K/R_{eff} is calculated based on the equation S1. Estimation is calculated by a linear least-square fitting model from the experimental results of hierarchical nanowires,[93] bi-porous sintered copper wick and bijel-derived copper scaffolds. Second degree polynomial is used for the linear fitting because wicked volume flux is radial spreading of the liquid while capillary performance parameter is measured by vertical liquid rate-of-rise test.

4.3.4. Two-Step Liquid Infiltration Mechanisms

To understand the capillary wicking mechanisms through the hierarchically structured scaffolds, we observe microscopic capillary wicking behaviors through environmental scanning electron microscopy (ESEM). As shown in Figure 4.12a, the copper scaffold is mounted on the cold stage with carbon tape to separate the sample from direct contact with the stage where the temperature and pressure are controlled to provide liquid into the structures. Due to the spacing between the mounted sample and the cold stage, direct condensation can be prevented ahead of capillary wicking. Temperature of the sample

mount is set to 4°C with the saturation condition of 100 RH% at 8 mbar of chamber pressure.

The water feeding under the sample is initiated by gradually increasing the chamber pressure from 8 mbar to 11.5 mbar since sudden pressure change might cause direct condensation to the sample (Figure 4.12b-d). Then, the condensed water at the sample stage infiltrates the copper scaffold by covering the 2nd order roughness first followed by filling of 1st order pores (Figure 4.12e-f). This microscopic observation indicates the nanoscale morphology leads to the initial prewetting of the copper scaffold allowing the enhancement of capillary wicking. The early liquid spreading through 2nd order morphology decreases contact angle θ, resulting in the increase in capillary pressure $\Delta P = 2\sigma/R_{eff}$, where effective pore radius is $R_{eff} = R_p \times \cos\theta$, σ is the surface tension, and R_p is the pore radius. Thereby, the high capillary pressure leads to the increase in the $\dot{V}''$ through the hierarchically structured copper scaffold. Therefore, the observation through ESEM indicate that the capillary wicking and thus liquid infiltration through porous media can be enhanced by implementing 2nd order structures resulting in large capillary pressure. This fundamental understanding of liquid transport through hierarchically designed porous media can significantly contribute to the design of porous structured for the advanced thermal management systems. Furthermore, studying how wettability and capillary wicking through nanostructures is attributed to the micro or macroscale transport phenomena will be critical for many aspects such as energy storage devices, energy conversion, or desalinations.
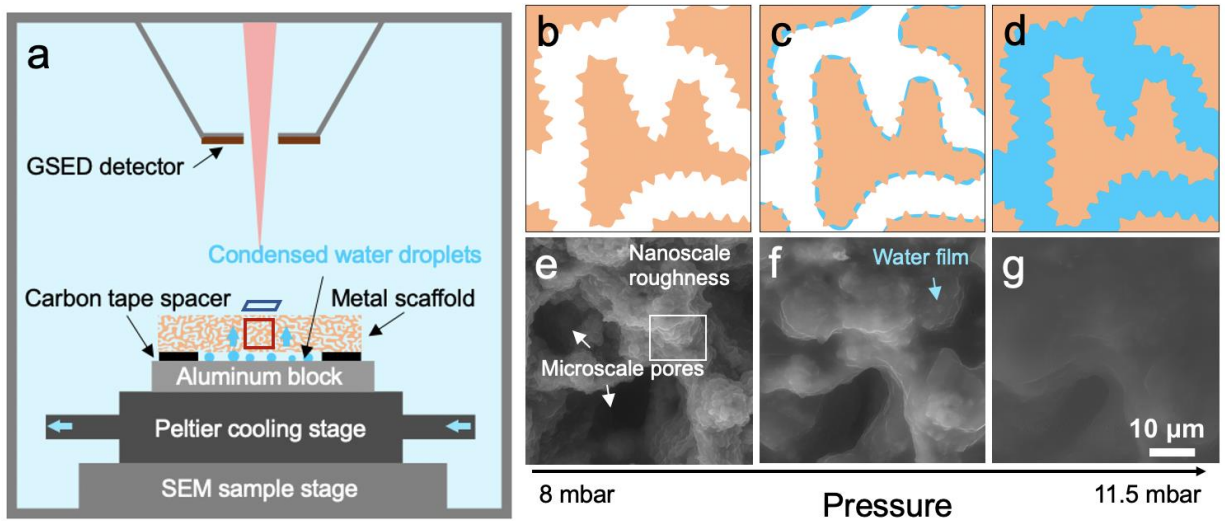
Figure 4.12. Microscale optical observation of two-step capillary wicking mechanisms by using environmental SEM. (a) Schematic illustration shows the experimental setup that measures capillary wicking behavior from the bottom to the top condensing surface. The illustrations and microscopic images show the copper scaffold (b, e) before water infiltration at T=4 °C and P=8 mbar. As the chamber environment become saturated with a high pressure, the water (c, f) first infiltrates through the surface roughness and (d, g) fills the microscale pores, which suggests that the use of hierarchical structure promotes the capillary-driven liquid filtration.

4.4. Summary of the Chapter

In conclusion, we demonstrate the liquid transport behavior on the hierarchically designed copper scaffolds with controlled nanoscale morphology assisted by templating soft materials, bijel. The bijel-templated metal scaffolds offer two unique capabilities to independently control the size of micropores with varying surface nanostructures, and to offer regular and continuous liquid pathways. The rational design of hierarchically porous copper scaffolds with spinodal morphology suggest the superior capability for wicking and wicking-assisted two-phase change performance. The role of the nanoscale morphology in the liquid infiltration is investigated by testing transient and dynamic droplet topologies comparing to the liquid infiltration model. We found that the droplet depletion time through the copper scaffolds is mostly determined in the CDA phase and the dynamic contact angle is independent of the nanoscale morphology. Furthermore, the hierarchically designed copper scaffolds achieve an enhancement of the wicked volume flux by 191% and by 163% compared to the commercially available sintered copper particles or the copper scaffold without nanoscale structures, suggesting the potential use of two-phase heat transfer application. In addition, it is elucidated that enhancement of wicking performance is attributed to the wetting mechanism, where the liquid first wets nanoscale structures and fills in the liquid pathways originated from micropores.

CHAPTER 5: Conclusions and Suggestions

In summary, this dissertation aims to elucidate liquid transport in hierarchically structured surfaces that are composed of multiple length scale features. The understanding of liquid transport and capillary effect can be used to design proper engineering surfaces with desirable surface properties for advanced thermal management systems. In addition to the summary, the future direction of the research that can be extended from this dissertation study is provided.

5.1. Summary

We demonstrate that the hierarchically structured surfaces have the potential to overcome the tradeoff between two transport parameters: permeability and capillary pressure. This tradeoff is successfully mitigated by using hierarchical design of engineering surfaces to optimize the individual transport phenomena in different length scales. The ability to deliver liquid through hierarchical structured surfaces pushes the fundamental liquid transport limits in porous media by providing additional capillary pressure to the lower-level hierarchy such as nanoscale pores and nanoscale roughness as well as minimizing hydraulic resistance through the upper-level hierarchy.

Firstly, we investigate the role of liquid permeability in hierarchically structured surfaces with uniform nanofeatures. To manipulate the permeability, we design the vertically aligned hierarchical nanowires contain submicron nanowires (200, 400, and 1000 nm in diameter) with sharp copper oxide nanofeatures. We carefully characterize dynamic wettability and spreading on the plain CuO nanofeatures to explain the role of those features

in liquid transport in hierarchical surfaces. The combined experimental measurements and computations explain how the wicking performance is improved regarding the inter-nanowire pores as well as the structural porosity. The hierarchical nanowires possess enhanced capillary performance parameter ranging K/R_{eff} = 0.004-0.023 μm depending on the hydraulic diameter of the nanowires. We found that permeability is the dominant factor for capillary wicking of the hierarchical nanowires with the constant porosity and nanoscale feature sizes. (Chapter 2)

Based on the understanding of liquid transport in hierarchical nanowires, we explore capillary-driven liquid transport in hierarchical surfaces with complex heterogeneous properties. The heterogeneous properties can be achieved by using Cu and Ni as segmentation components of the nanowires where Cu portion is modified by hydrophilic CuO nanofeatures and Ni portion remains intact due to the corrosion resistance. The experimental results show that liquid transport in segmented nanowires with a hydrophilic portion at the bottom is not impacted by the existence of hydrophobic. Through the hierarchical design of surfaces with heterogeneous properties, CHF and HTC in boiling heat transfer are improved simultaneously because the hydrophobic wettability promotes bubble dynamics in the nucleation boiling region, and liquid is replenished through capillary wicking leading to the prevention of transition to film boiling. (Chapter 3)

Lastly, we explore the role of nanoscale morphology in liquid transport using the hierarchically designed copper scaffolds assisted by Bijel. The Bijel-templated porous media can provide superior liquid permeability due to its large connectivity, uniform domain size, and low tortuosity with spinodal-like morphology. The nanoscale morphologies with varying

surface roughness and pores are successfully installed on the copper scaffolds *via* electroless metal deposition and calcination steps. The liquid transport is significantly improved for the copper scaffold with nanoscale pores about 190% and 160% comparing to the commercial sintered copper particles and the copper scaffold with nanoscale roughness. The wicking mechanism through hierarchically structured surfaces is confirmed by Environment SEM observation, where the liquid film is formed on the nanoscale structures resulting in enhancement of capillary pressure applied to microscale pores. (Chapter 4)
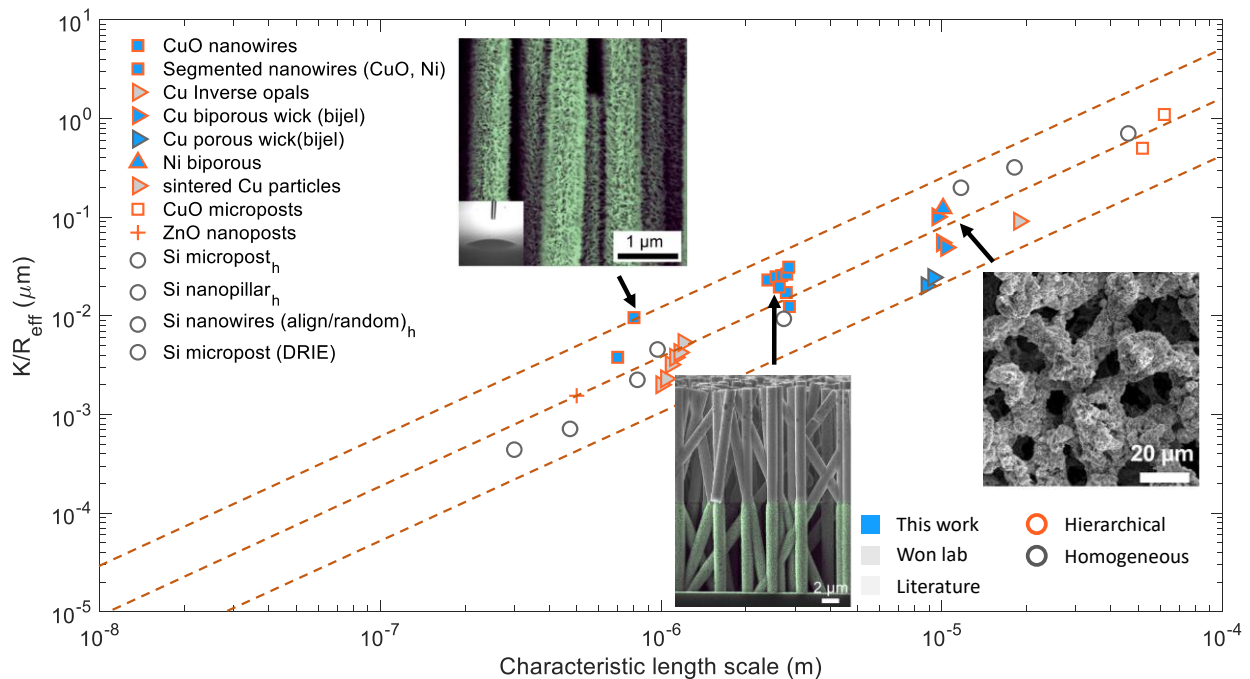
Figure 5.1. Capillary performance parameters of various porous media.

5.2. Suggestions for Future Works

5.2.1. Flexible Nanowire Arrays

The research presented in this dissertation can be extended to future work such as flexible wicking materials. The thermal management of electronics can be even more challenging as electronic devices become thinner, flexible, and higher power dense. To address the cooling problem of such electronics, ultrathin heat pipes (UTHPs) have been proposed and investigated. The heat dissipation performance of the UTHPs is highly dependent on the wicking performance of the porous wick due to the capillary limit. Furthermore, the flexible property can be combined in UTHPs by using proper substrate and porous wick with flexibility and wicking performance.
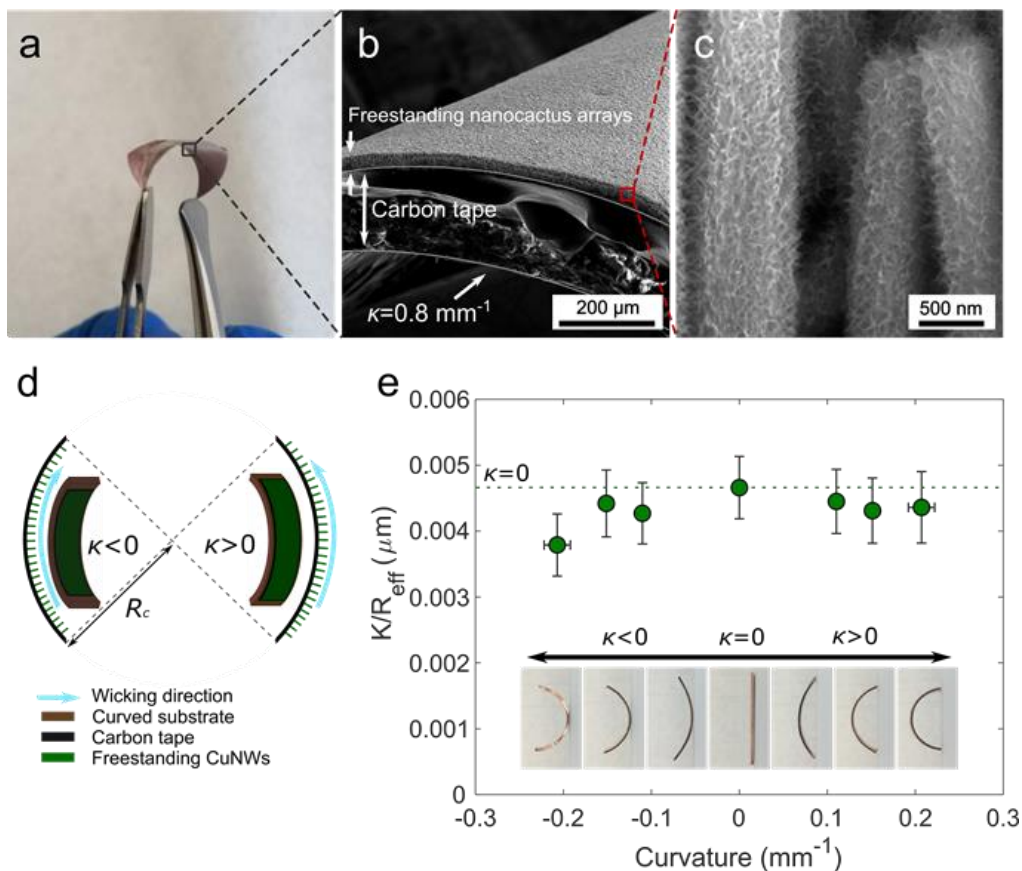
Figure 5.2. Wicking performances of the freestanding CuO nanocactus arrays. (a) A photograph image shows the freestanding CuO nanocactuses fabricated on a flexible copper layer. SEM images in (b) and (c) confirm the CuO nanocactuses' vertical alignment despite the curvature. (d) The CuO nanocactus array is mounted on the 0.5 mm-thick copper substrate with a predefined curvature by using a double-sided carbon tape, where the curvature κ is defined as the inverse of the radius of curvature $|\kappa| = 1/R_c$. The κ has positive and negative signs for convex- and concave-shaped curved surfaces, respectively. € Capillary performance parameters K/R_{eff} are plotted for different substrate curvatures, showing relatively small decreases. The radius of curvature of each substrate is R_c = ∞, 9.07, 6.61, and 4.83 mm, and the corresponding curvature is κ = 0, ±0.11, ±0.15, and ±0.21 mm^{-1}, respectively. The error bars represent the uncertainty in the curvature and capillary performance parameter due to the nonuniform thickness of copper substrate.

As an effort to introduce flexible wicking material, we introduce the vertically aligned nanowire arrays on flexible substrates or "freestanding nanowire arrays" with various curvatures as shown in Figure 5.2. For this, a 3.5 μm-thin copper layer is first grown on the backside of the sacrificial template with 400 nm of nominal pore diameter by the electrodeposition method. The removal of a sacrificial template remains freestanding Cu nanowire arrays on the 3.5 μm-thin copper layer that provides structural flexibility. The liquid-rise measurements indicate that freestanding nanowire arrays can maintain the comparable wicking performance during the bending for the range of curvature κ from -0.21 to 0.21 mm^{-1}, which leads to relatively small decreases (10% - 20%) in wicking performance compared to the K/R_{eff} at κ = 0 mm^{-1}. Despite the highly curved state at the macroscale, the changes of aligned nanowires at the microscale are negligible, as represented by the changes in the hydraulic diameter of less than 1% for all curvature conditions. For example, the effective height theoretically differs by < 0.0001% with the given radius of curvature at the extreme tilting angle of 50°,[64] which agrees with the investigation through multiple SEM measurements as shown in Figure 5.3.

This direct electrodeposition method to the sacrificial template offers plenty of opportunities to develop flexible porous wick for advanced thermal management systems. However, understanding of flexible porous wick is still lacking such as mechanical requirements to resist inner pressure or to mitigate gap of the radius of curvature. Therefore, mechanical properties and two-phase heat transfer in the closed system should be studied in the future for the development of flexible porous wick. Those advanced designs of nanowires such as flexible or segmented nanowires introduced in this dissertation can be further used in sensor or energy storage devices.
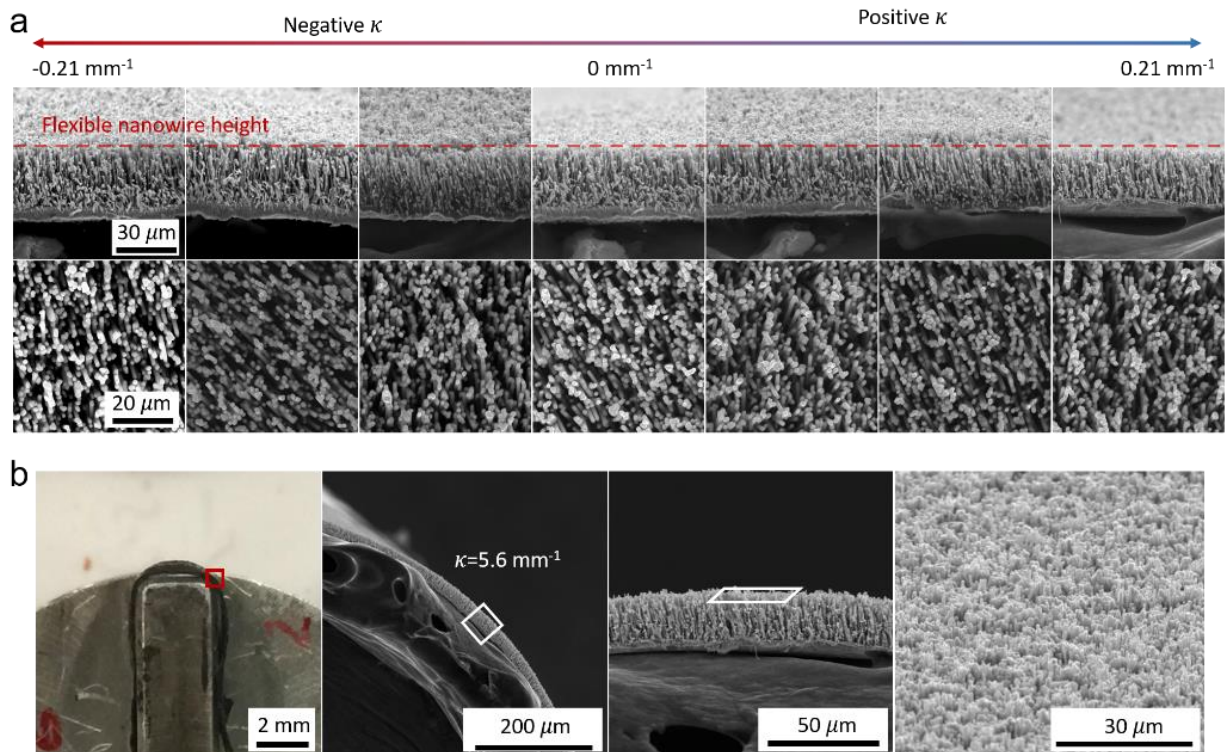
Figure 5.3. SEM images and photograph of the flexible freestanding nanowires with various curvature. (a) SEM images show the cross-sectional and top view morphology of the freestanding nanowire arrays during bending where the κ = 0, ±0.11, ±0.15, and ±0.21. The changes in nanowire alignments and thickness can be negligible. (b) The photograph and corresponding SEM images show the freestanding nanowires at an extreme bending with κ = 5.6mm^{-1}, confirming the nanowire alignments.

5.2.2. Scalable Fabrication of Bijel

Recent advancements of the fabrication method of bijel allow creating biporous structures to improve liquid transport by controlling features in different length scale independently as well as maintaining unique spinodal-like morphology. Despite the potential of the bijel-derived metal scaffolds on the interphase liquid transport or liquid percolation, it has not yet been studied due to its difficulty of fabrication for large scaffolds to investigate the capillary rise. The challanges of large-scale fabrication in the current method result from the monomer exchange process that requires a vertical type of mold, which limits the increase in the size. To address this issue, we introduce a scalable fabrication method of the bijel by the direct phase separation of the monomers without needing the monomer exchange step.
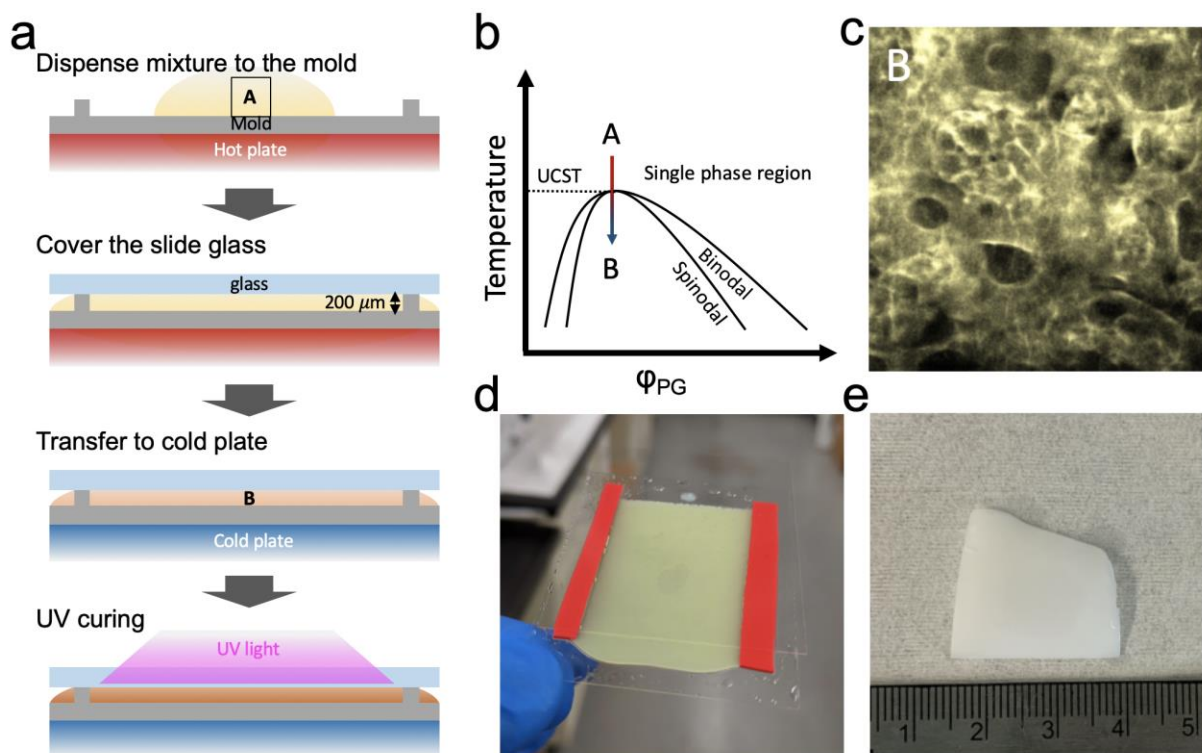
Figure 5.4. Fabrication of bijel-derived polymer scaffold by the scalable method. (a) Schematic illustration shows the fabrication steps. (b) The PG and TMPTA show a phase separation under the UCST. The PG and TMPTA is mixed at critical point to attest spinodal decomposition. (c) Confocal microscope image shows the spinodal decomposition of the mixture after the phase separation. Photographs show the bijel-derived polymer scaffold after (d) UV curing and (e) HF etching.
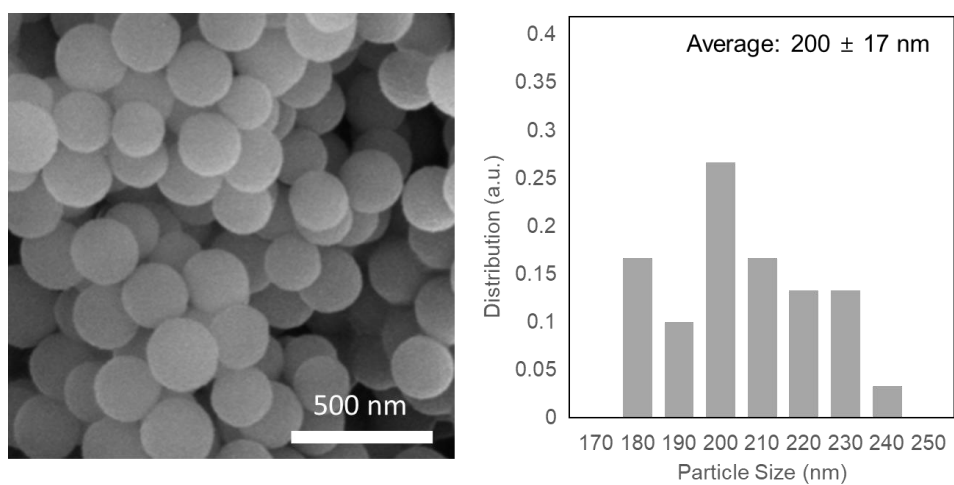
Figure 5.5. Silica nanoparticles prepared by modified Stöber method. The nanoparticle is modified with FITC to obtain neural wettability of PG and TMPTA. The nanoparticles' diameter is about 200 nm with narrow size distribution.

For large-scale fabrication of bijel, we introduce a propylene glycol (PG) and trimethylolpropane ethoxylate triacrylate (TMPTA) system (P/T system) with fluorescein sodium salt (FITC) modified silica nanoparticles. The FITC modified silica nanoparticles are synthesized by the modified Stöber method (~200 nm) as shown in Figure 5.5. Comparing to the conventional fabrication method (W/L system), the P/T system could overcome the size limitation of the bijel-derived polymer scaffold since the UV curable monomer is directly mixed with the PG. The scalable fabrication method could utilize the horizontal mold due to the absence of the monomer exchange step as shown in Figure 5.4. Furthermore, the phase separation is initiated around 10°C and finished within 5 min, which shows the potential for a scalable and continuous fabrication. The capillary performance parameter obtained by using the biporous scaffolds prepared by scalable method K/R_{eff} = 0.122 μm with ϕ=0.89 as shown in Figure 5.6.
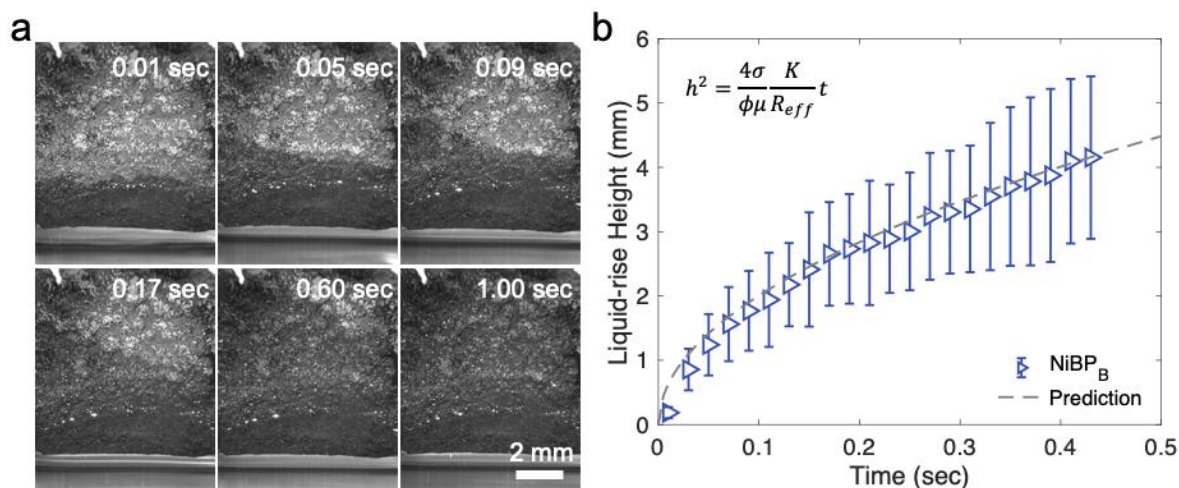
Figure 5.6. Capillary-driven liquid rise in biporous nickel scaffold prepared by the scalable fabrication method. (a) The images captured by high-speed camera show the liquid rise over time through the metal scaffold. (b) Liquid rise trend follows the Lucas-Washburn equation with h^2 and t.

However, a lack of understanding of the metal deposition and calcination processes hinders the creation of nanoscale features using polymer scaffolds with high crosslinking density. Also, metal deposition is more challenging than conventional bijel-template polymer scaffolds due to the hydrophobic property resulting from the TMPTA scaffolds. Therefore, those issues mentioned above should be addressed to employ in industrial applications such as porous wick, battery electrode, or membrane. This suggests that the fabrication techniques of bijel are still needed to be studied and have opportunities to be improved for developing multiscale structures.

Bibliography

[1] E. Pop, Energy dissipation and transport in nanoscale devices, Nano Res. 3 (2010) 147–169. https://doi.org/10.1007/s12274-010-1019-z.

[2] S.M. Sohel Murshed, C.A. Nieto de Castro, A critical review of traditional and emerging techniques and fluids for electronics cooling, Renew. Sustain. Energy Rev. 78 (2017) 821–833. https://doi.org/10.1016/j.rser.2017.04.112.

[3] B.S. Kim, G. Choi, D. Il Shim, K.M. Kim, H.H. Cho, Surface roughening for hemi-wicking and its impact on convective boiling heat transfer, Int. J. Heat Mass Transf. 102 (2016) 1100–1107. https://doi.org/10.1016/j.ijheatmasstransfer.2016.07.008.

[4] C.K. Guan, B. Bon, J. Klausner, R. Mei, Comparison of CHF enhancement on microstructured surfaces with a predictive model, Heat Transf. Eng. 35 (2014) 452–460. https://doi.org/10.1080/01457632.2013.833043.

[5] B. Bon, J.F. Klausner, E. Mckenna, The Hoodoo: A New Surface Structure for Enhanced Boiling Heat Transfer, J. Therm. Sci. Eng. Appl. 5 (2013) 011003. https://doi.org/10.1115/1.4007439.

[6] R. Wen, Q. Li, W. Wang, B. Latour, C.H. Li, C. Li, Y.C. Lee, R. Yang, Enhanced bubble nucleation and liquid rewetting for highly efficient boiling heat transfer on two-level hierarchical surfaces with patterned copper nanowire arrays, Nano Energy. 38 (2017) 59–65. https://doi.org/10.1016/j.nanoen.2017.05.028.

[7] K.H. Chu, Y.S. Joung, R. Enright, C.R. Buie, E.N. Wang, Hierarchically structured surfaces for boiling critical heat flux enhancement, Appl. Phys. Lett. 102 (2013). https://doi.org/10.1063/1.4801811.

[8] H.S. Ahn, G. Park, J.M. Kim, J. Kim, M.H. Kim, The effect of water absorption on critical heat flux enhancement during pool boiling, Exp. Therm. Fluid Sci. 42 (2012) 187–195. https://doi.org/10.1016/j.expthermflusci.2012.05.005.

[9] S. Bhavnani, V. Narayanan, W. Qu, M. Jensen, S. Kandlikar, J. Kim, J. Thome, Boiling augmentation with Micro/Nanostructured surfaces: Current status and research outlook, Nanoscale Microscale Thermophys. Eng. 18 (2014) 197–222. https://doi.org/10.1080/15567265.2014.923074.

[10] H. O'Hanley, C. Coyle, J. Buongiorno, T. McKrell, L.-W. Hu, M. Rubner, R. Cohen, Separate effects of surface roughness, wettability, and porosity on the boiling critical heat flux, Appl. Phys. Lett. 103 (2013) 24102. https://doi.org/10.1063/1.4813450.

[11] Z. Yao, Y.W. Lu, S.G. Kandlikar, Effects of nanowire height on pool boiling performance of water on silicon chips, Int. J. Therm. Sci. 50 (2011) 2084–2090. https://doi.org/10.1016/j.ijthermalsci.2011.06.009.

[12] F. Wu, H. Ze, S. Chen, X. Gao, High-Efficiency Boiling Heat Transfer Interfaces Composed of Electroplated Copper Nanocone Cores and Low-Thermal-Conductivity

Nickel Nanocone Coverings, ACS Appl. Mater. Interfaces. 12 (2020) 39902–39909. https://doi.org/10.1021/acsami.0c10761.

[13] S.G. Kandlikar, A Theoretical Model to Predict Pool Boiling CHF Incorporating Effects of Contact Angle and Orientation, J. Heat Transfer. 123 (2001) 1071. https://doi.org/10.1115/1.1409265.

[14] J.L. Plawsky, A.G. Fedorov, S. V. Garimella, H.B. Ma, S.C. Maroo, L. Chen, Y. Nam, Nano- and microstructures for thin-film evaporation-A review, Nanoscale Microscale Thermophys. Eng. 18 (2014) 251–269. https://doi.org/10.1080/15567265.2013.878419.

[15] S. Ridwan, M. McCarthy, Nanostructure-Supported Evaporation Underneath a Growing Bubble, ACS Appl. Mater. Interfaces. (2019) acsami.8b21260. https://doi.org/10.1021/acsami.8b21260.

[16] K.L. Wilke, B. Barabadi, Z. Lu, T. Zhang, E.N. Wang, Parametric study of thin film evaporation from nanoporous membranes, Appl. Phys. Lett. 111 (2017) 171603. https://doi.org/10.1063/1.4997945.

[17] X. Dai, Boiling and Evaporation on Micro/nanoengineered Surfaces, 2013.

[18] A. Brautsch, P.A. Kew, Examination and visualisation of heat transfer processes during evaporation in capillary porous structures, in: Appl. Therm. Eng., 2002: pp. 815–824. https://doi.org/10.1016/S1359-4311(02)00027-3.

[19] C.K. Wemp, V.P. Carey, Water Wicking and Droplet Spreading on Randomly Structured Thin Nanoporous Layers, Langmuir. 33 (2017) 14513–14525. https://doi.org/10.1021/acs.langmuir.7b03687.

[20] D. Zheng, C.H. Choi, G. Sun, X. Zhao, Superwicking on Nanoporous Micropillared Surfaces, ACS Appl. Mater. Interfaces. 12 (2020) 30925–30931. https://doi.org/10.1021/acsami.0c04366.

[21] Q.N. Pham, M.T. Barako, J. Tice, Y. Won, Microscale Liquid Transport in Polycrystalline Inverse Opals across Grain Boundaries, Sci Rep. 7 (2017) 10465. https://doi.org/10.1038/s41598-017-10791-3.

[22] E.W. Washburn, The dynamics of capillary flow, Phys. Rev. 17 (1921) 273–283. https://doi.org/10.1103/PhysRev.17.273.

[23] R. Lucas, Ueber das Zeitgesetz des kapillaren Aufstiegs von Flüssigkeiten, Kolloid-Zeitschrift. 23 (1918) 15–22. https://doi.org/10.1007/BF01461107.

[24] N. Fries, M. Dreyer, The transition from inertial to viscous flow in capillary rise, J. Colloid Interface Sci. 327 (2008) 125–128. https://doi.org/10.1016/j.jcis.2008.08.018.

[25] R.N. Wenzel, Resistance of solid surfaces to wetting by water, Ind. Eng. Chem. 28 (1936) 988–994.

[26] B.D. Cassie, Wettability of porous surfaces, Physics (College. Park. Md). 40 (1944) 546–551. http://pubs.rsc.org/en/content/articlepdf/1944/tf/tf9444000546.

[27] Z. Yao, Y.-W. Lu, S.G. Kandlikar, Pool Boiling Heat Transfer Enhancement Through Nanostructures on Silicon Microchannels, J. Nanotechnol. Eng. Med. 3 (2013) 031002. https://doi.org/10.1115/1.4007425.

[28] K.-H. Chu, Y. Soo Joung, R. Enright, C.R. Buie, E.N. Wang, Hierarchically structured surfaces for boiling critical heat flux enhancement, Appl. Phys. Lett. 102 (2013) 151602. https://doi.org/10.1063/1.4801811.

[29] N. Miljkovic, R. Enright, E.N. Wang, Modeling and Optimization of Superhydrophobic Condensation, J. Heat Transfer. 135 (2013) 111004. https://doi.org/10.1115/1.4024597.

[30] N. Fries, M. Dreyer, An analytic solution of capillary rise restrained by gravity, J. Colloid Interface Sci. 320 (2008) 259–263. https://doi.org/10.1016/j.jcis.2008.01.009.

[31] S. Levine, G.H. Neale, Theory of the rate of wetting of a porous medium, J. Chem. Soc. Faraday Trans. 2. 71 (1975) 12. https://doi.org/10.1039/f29757100012.

[32] D.W. Guillaume, D. DeVries, Improving the pneumatic nebulizer by shaping the discharge of the capillary wick, J. Biomed. Eng. 13 (1991) 526–528. https://doi.org/10.1016/0141-5425(91)90103-E.

[33] J. Bico, C. Tordeux, D. Quéré, Rough wetting, Europhys. Lett. 55 (2001) 214–220. https://doi.org/10.1209/epl/i2001-00402-x.

[34] K.H. Chu, R. Enright, E.N. Wang, Structured surfaces for enhanced pool boiling heat transfer, Appl. Phys. Lett. 100 (2012) 161605–241603. https://doi.org/10.1063/1.4724190.

[35] C. Byon, S.J. Kim, Capillary performance of bi-porous sintered metal wicks, Int. J. Heat Mass Transf. 55 (2012) 4096–4103. https://doi.org/10.1016/j.ijheatmasstransfer.2012.03.051.

[36] J.A. Weibel, S.S. Kim, T.S. Fisher, S. V Garimella, Carbon nanotube coatings for enhanced capillary-fed boiling from porous microstructures, Nanoscale Microscale Thermophys. Eng. 16 (2012) 1–17. https://doi.org/10.1080/15567265.2011.646000.

[37] W. Ling, W. Zhou, R. Liu, Q. Qiu, Y. Ke, Operational characteristics of loop heat pipes with porous copper fiber sintered sheet as wick, Appl. Therm. Eng. 122 (2017) 398–408. https://doi.org/10.1016/j.applthermaleng.2017.03.120.

[38] A. Rogacs, J.E. Steinbrenner, J.A. Rowlette, J.M. Weisse, X.L. Zheng, K.E. Goodson, Characterization of the wettability of thin nanostructured films in the presence of evaporation, J Colloid Interface Sci. 349 (2010) 354–360. https://doi.org/10.1016/j.jcis.2010.05.063.

[39] C.K. Wemp, V.P. Carey, Water Wicking and Droplet Spreading on Randomly Structured Thin Nanoporous Layers, Langmuir. 33 (2017) 14513–14525. https://doi.org/10.1021/acs.langmuir.7b03687.

[40] C. Byon, S.J. Kim, Study on the capillary performance of micro-post wicks with non-homogeneous configurations, Int. J. Heat Mass Transf. 68 (2014) 415–421. https://doi.org/10.1016/j.ijheatmasstransfer.2013.09.064.

[41] S. Ryu, W. Lee, Y. Nam, Heat transfer and capillary performance of dual-height superhydrophilic micropost wicks, Int. J. Heat Mass Transf. 73 (2014) 438–444. https://doi.org/10.1016/j.ijheatmasstransfer.2014.02.020.

[42] H.S. Ahn, G. Park, J. Kim, M.H. Kim, Wicking and spreading of water droplets on nanotubes, Langmuir. 28 (2012) 2614–2619. https://doi.org/10.1021/la204073n.

[43] M.C. Lu, R. Chen, V. Srinivasan, V.P. Carey, A. Majumdar, Critical heat flux of pool boiling on Si nanowire array-coated surfaces, Int. J. Heat Mass Transf. 54 (2011) 5359–5367. https://doi.org/10.1016/j.ijheatmasstransfer.2011.08.007.

[44] O. Assad, A.M. Leshansky, B. Wang, T. Stelzner, S. Christiansen, H. Haick, Spray-Coating Route for Highly Aligned and Large-Scale Arrays of Nanowires, ACS Nano. 6 (2012) 4702–4712. https://doi.org/10.1021/nn204513y.

[45] Z. Lao, Y. Hu, C. Zhang, L. Yang, J. Li, J. Chu, D. Wu, Capillary Force Driven Self-Assembly of Anisotropic Hierarchical Structures Prepared by Femtosecond Laser 3D Printing and Their Applications in Crystallizing Microparticles, ACS Nano. 9 (2015) 12060–12069. https://doi.org/10.1021/acsnano.5b04914.

[46] T.T. Mai, C.Q. Lai, H. Zheng, K. Balasubramanian, K.C. Leong, P.S. Lee, C. Lee, W.K. Choi, Dynamics of wicking in silicon nanopillars fabricated with interference lithography and metal-assisted chemical etching, Langmuir. 28 (2012) 11465–11471. https://doi.org/10.1021/la302262g.

[47] J. Liu, X. Chen, J. Kim, Q. Zheng, H. Ning, P. Sun, X. Huang, J. Liu, J. Niu, P. V Braun, High volumetric capacity three-dimensionally sphere-caged secondary battery anodes, Nano Lett. 16 (2016) 4501–4507. https://doi.org/10.1021/acs.nanolett.6b01711.

[48] S.C. O'Hern, D. Jang, S. Bose, J.C. Idrobo, Y. Song, T. Laoui, J. Kong, R. Karnik, Nanofiltration across defect-sealed nanoporous monolayer graphene, Nano Lett. 15 (2015) 3254–3260. https://doi.org/10.1021/acs.nanolett.5b00456.

[49] Z. Liang, G. Zheng, W. Li, Z.W. Seh, H. Yao, K. Yan, D. Kong, Y. Cui, Sulfur cathodes with hydrogen reduced titanium dioxide inverse opal structure, ACS Nano. 8 (2014) 5249–5256. https://doi.org/10.1021/nn501308m.

[50] Z. Wang, J. Zhao, A. Bagal, E.C. Dandley, C.J. Oldham, T. Fang, G.N. Parsons, C.H. Chang, Wicking Enhancement in Three-Dimensional Hierarchical Nanostructures, Langmuir. 32 (2016) 8029–8033. https://doi.org/10.1021/acs.langmuir.6b01864.

[51] S.M. Jung, D.J. Preston, H.Y. Jung, Z. Deng, E.N. Wang, J. Kong, Porous Cu Nanowire Aerosponges from One-Step Assembly and their Applications in Heat Dissipation, Adv. Mater. 28 (2016) 1413–1419. https://doi.org/10.1002/adma.201504774.

[52] R. Ranjan, A. Patel, S. V. Garimella, J.Y. Murthy, Wicking and thermal characteristics of micropillared structures for use in passive heat spreaders, Int. J. Heat Mass Transf. 55 (2012) 586–596. https://doi.org/10.1016/j.ijheatmasstransfer.2011.10.053.

[53] R. Masoodi, K.M. Pillai, P.P. Varanasi, Effect of Externally Applied Liquid Pressure on Wicking in Paper Wipes, J. Eng. Fibers Fabr. 5 (2010) 49–66. http://www.jeffjornal.org (accessed February 1, 2018).

[54] A.Y.Y. Ho, L.P. Yeo, Y.C. Lam, I. Rodríguez, Fabrication and analysis of gecko-inspired hierarchical polymer nanosetae, ACS Nano. 5 (2011) 1897–1906. https://doi.org/10.1021/nn103191q.

[55] K. Han, L. Heng, L. Jiang, Multiphase Media Antiadhesive Coatings: Hierarchical Self-Assembled Porous Materials Generated Using Breath Figure Patterns, ACS Nano. 10 (2016) 11087–11095. https://doi.org/10.1021/acsnano.6b05961.

[56] Q.N. Pham, B. Shao, Y. Kim, Y. Won, Hierarchical and Well-Ordered Porous Copper for Liquid Transport Properties Control, ACS Appl. Mater. Interfaces. 10 (2018) 16015–16023. https://doi.org/10.1021/acsami.8b02665.

[57] L. Petti, N. Münzenrieder, C. Vogt, H. Faber, L. Büthe, G. Cantarella, F. Bottacchi, T.D. Anthopoulos, G. Tröster, Metal oxide semiconductor thin-film transistors for flexible electronics, Appl. Phys. Rev. 3 (2016) 021303. https://doi.org/10.1063/1.4953034.

[58] T. Cheng, Y. Zhang, W.Y. Lai, W. Huang, Stretchable thin-film electrodes for flexible electronics with high deformability and stretchability, Adv. Mater. 27 (2015) 3349–3376. https://doi.org/10.1002/adma.201405864.

[59] J.G. Lee, Y. Kwon, J.Y. Ju, S. Choi, Y. Kang, W.R. Yu, D.W. Kim, Fiber electrode by one-pot wet-spinning of graphene and manganese oxide nanowires for wearable lithium-ion batteries, J. Appl. Electrochem. 47 (2017) 865–875. https://doi.org/10.1007/s10800-017-1085-y.

[60] M.M. Rahman, E. Olceroglu, M. McCarthy, Role of wickability on the critical heat flux of structured superhydrophilic surfaces, Langmuir. 30 (2014) 11225–11234. https://doi.org/10.1021/la5030923.

[61] N. Youngsuk, S. Sharratt, C. Byon, K. Sung Jin, Y.S. Ju, Fabrication and Characterization of the Capillary Performance of Superhydrophilic Cu Micropost Arrays, J. Microelectromechanical Syst. 19 (2010) 581–588. https://doi.org/10.1109/jmems.2010.2043922.

[62] K.-S. Yang, T.-Y. Yang, C.-W. Tu, C.-T. Yeh, M.-T. Lee, A novel flat polymer heat pipe with thermal via for cooling electronic devices, Energy Convers. Manag. 100 (2015) 37–44. https://doi.org/10.1016/j.enconman.2015.04.063.

[63] C. Yang, C. Chang, C. Song, W. Shang, J. Wu, P. Tao, T. Deng, Fabrication and performance evaluation of flexible heat pipes for potential thermal control of foldable electronics, Appl. Therm. Eng. 95 (2016) 445–453. https://doi.org/10.1016/j.applthermaleng.2015.11.078.

[64] M.T. Barako, S. Roy-Panzer, T.S. English, T. Kodama, M. Asheghi, T.W. Kenny, K.E. Goodson, Thermal Conduction in Vertically Aligned Copper Nanowire Arrays and Composites, ACS Appl Mater Interfaces. 7 (2015) 19251–19259. https://doi.org/10.1021/acsami.5b05147.

[65] N.S. Dhillon, J. Buongiorno, K.K. Varanasi, Critical heat flux maxima during boiling crisis on textured surfaces, Nat. Commun. 6 (2015) 1–12. https://doi.org/10.1038/ncomms9247.

[66] H. Jo, D.I. Yu, H. Noh, H.S. Park, M.H. Kim, Boiling on spatially controlled heterogeneous surfaces: Wettability patterns on microstructures, Appl. Phys. Lett. 106 (2015) 181602. https://doi.org/10.1063/1.4919916.

[67] S. Shin, G. Choi, B.S. Kim, H.H. Cho, Flow boiling heat transfer on nanowire-coated surfaces with highly wetting liquid, Energy. 76 (2014) 428–435. https://doi.org/10.1016/j.energy.2014.08.037.

[68] D. Li, G.S. Wu, W. Wang, Y.D. Wang, D. Liu, D.C. Zhang, Y.F. Chen, G.P. Peterson, R. Yang, Enhancing flow boiling heat transfer in microchannels for thermal management with monolithically-integrated silicon nanowires, Nano Lett. 12 (2012) 3385–3390. https://doi.org/10.1021/nl300049f.

[69] M.T. Barako, S.G. Isaacson, F. Lian, E. Pop, R.H. Dauskardt, K.E. Goodson, J. Tice, Dense Vertically Aligned Copper Nanowire Composites as High Performance Thermal Interface Materials, ACS Appl. Mater. Interfaces. 9 (2017) 42067–42074. https://doi.org/10.1021/acsami.7b12313.

[70] J. Bico, U. Thiele, D. Quéré, Wetting of textured surfaces, in: Colloids Surfaces A Physicochem. Eng. Asp., 2002: pp. 41–46. https://doi.org/10.1016/S0927-7757(02)00061-4.

[71] E.C. U, R. Perea-carpio, Problems of contact angle and solid surface free energy determination, Adv. Colloid Interface Sci. 98 (2002) 245–264. https://ac.els-cdn.com/S0001868601000975/1-s2.0-S0001868601000975-main.pdf?_tid=0518ff9c-82b9-4aef-9b44-26d36e0065d9&acdnat=1529540284_f49b9c9ec91b250dce771b6a70b39866 (accessed June 20, 2018).

[72] A.B.D. Cassie, S. Baxter, Wettability of porous surfaces, Trans. Faraday Soc. 40 (1944) 546. https://doi.org/10.1039/tf9444000546.

[73] R.N. WENZEL, Resistance of Solid surfaces to Wetting by Water, Ind. Eng. Chem. 28 (1936).

[74] P.D. Dongare, A. Alabastri, S. Pedersen, K.R. Zodrow, N.J. Hogan, O. Neumann, J. Wu, T. Wang, A. Deshmukh, M. Elimelech, Q. Li, P. Nordlander, N.J. Halas, Nanophotonics-enabled solar membrane distillation for off-grid water purification, Proc. Natl. Acad. Sci. 114 (2017) 6936–6941. https://doi.org/10.1073/pnas.1701835114.

[75] T. Humplik, J. Lee, S.C. O'Hern, B.A. Fellman, M.A. Baig, S.F. Hassan, M.A. Atieh, F. Rahman, T. Laoui, R. Karnik, E.N. Wang, Nanostructured materials for water desalination, Nanotechnology. 22 (2011). https://doi.org/10.1088/0957-4484/22/29/292001.

[76] D. González, J. Amigo, F. Suárez, Membrane distillation: Perspectives for sustainable and improved desalination, Renew. Sustain. Energy Rev. 80 (2017) 238–259. https://doi.org/10.1016/j.rser.2017.05.078.

[77] A.K. Rajvanshi, J.S. Saini, R. Prakash, Investigation of macrolayer thickness in nucleate pool boiling at high heat flux, Int. J. Heat Mass Transf. 35 (1992) 343–350. https://doi.org/10.1016/0017-9310(92)90272-T.

[78] R. Chen, M. Lu, V. Srinivasan, Z. Wang, H.H. Cho, A. Majumdar, Nanowires for Enhanced Boiling Heat Transfer, Nano Lett. 9 (2009) 548–553. https://doi.org/10.1021/nl8026857.

[79] T.J. Hendricks, S. Krishnan, C. Choi, C.H. Chang, B. Paul, Enhancement of pool-boiling heat transfer using nanostructured surfaces on aluminum and copper, Int. J. Heat Mass Transf. 53 (2010) 3357–3365. https://doi.org/10.1016/j.ijheatmasstransfer.2010.02.025.

[80] J. Kim, Review of nucleate pool boiling bubble heat transfer mechanisms, Int. J. Multiph. Flow. 35 (2009) 1067–1076. https://doi.org/10.1016/j.ijmultiphaseflow.2009.07.008.

[81] C. Li, G.P. Peterson, Parametric Study of Pool Boiling on Horizontal Highly Conductive Microporous Coated Surfaces, J. Heat Transfer. 129 (2007) 1465. https://doi.org/10.1115/1.2759969.

[82] C. Li, Z. Wang, P.I. Wang, Y. Peles, N. Koratkar, G.P. Peterson, Nanostructured copper interfaces for enhanced boiling, Small. 4 (2008) 1084–1088. https://doi.org/10.1002/smll.200700991.

[83] M.M. Rahman, J. Pollack, M. McCarthy, Increasing Boiling Heat Transfer using Low Conductivity Materials, Sci. Rep. 5 (2015) 13145. https://doi.org/10.1038/srep13145.

[84] N.A. Patankar, Supernucleating surfaces for nucleate boiling and dropwise condensation heat transfer, Soft Matter. 6 (2010) 1613. https://doi.org/10.1039/b923967g.

[85] R.L. Agapov, J.B. Boreyko, D.P. Briggs, B.R. Srijanto, S.T. Retterer, C.P. Collier, N. V Lavrik, Asymmetric wettability of nanostructures directs Leidenfrost droplets, ACS Nano. 8 (2014) 860–867. https://doi.org/10.1021/nn405585m.

[86] R. Pastuszko, Pool boiling on micro-fin array with wire mesh structures, Int. J. Therm. Sci. 49 (2010) 2289–2298. https://doi.org/10.1016/j.ijthermalsci.2010.07.016.

[87] H. O'Hanley, C. Coyle, J. Buongiorno, T. McKrell, L.W. Hu, M. Rubner, R. Cohen, Separate effects of surface roughness, wettability, and porosity on the boiling critical heat flux, Appl. Phys. Lett. 103 (2013). https://doi.org/10.1063/1.4813450.

[88] B. Bourdon, R. Rioboo, M. Marengo, E. Gosselin, J. De Coninck, Influence of the wettability on the boiling onset, Langmuir. 28 (2012) 1618–1624. https://doi.org/10.1021/la203636a.

[89] M.M. Rahman, M. McCarthy, Boiling Enhancement on Nanostructured Surfaces with Engineered Variations in Wettability and Thermal Conductivity, Heat Transf. Eng. 38 (2017) 1285–1295. https://doi.org/10.1080/01457632.2016.1242961.

[90] Y.-T. Mu, L. Chen, Y.-L. He, Q.-J. Kang, W.-Q. Tao, Nucleate boiling performance evaluation of cavities at mesoscale level, Int. J. Heat Mass Transf. 106 (2017) 708–719. https://doi.org/10.1016/j.ijheatmasstransfer.2016.09.058.

[91] A. Koşar, C.-J. Kuo, Y. Peles, Boiling heat transfer in rectangular microchannels with reentrant cavities, Int. J. Heat Mass Transf. 48 (2005) 4867–4886. https://doi.org/10.1016/j.ijheatmasstransfer.2005.06.003.

[92] H. Honda, J.J. Wei, Enhanced boiling heat transfer from electronic components by use of surface microstructures, Exp. Therm. Fluid Sci. 28 (2004) 159–169. https://doi.org/10.1016/S0894-1777(03)00035-9.

[93] J. Lee, Y. Suh, P.P. Dubey, M.T. Barako, Y. Won, Capillary Wicking in Hierarchically Textured Copper Nanowire Arrays, ACS Appl. Mater. Interfaces. 11 (2019) 1546–1554. https://doi.org/10.1021/acsami.8b14955.

[94] Q.N. Pham, S. Zhang, S. Hao, K. Montazeri, C.H. Lin, J. Lee, A. Mohraz, Y. Won, Boiling Heat Transfer with a Well-Ordered Microporous Architecture, ACS Appl. Mater. Interfaces. 12 (2020) 19174–19183. https://doi.org/10.1021/acsami.0c01113.

[95] H. Jo, H.S. Park, M.H. Kim, Single bubble dynamics on hydrophobic-hydrophilic mixed surfaces, Int. J. Heat Mass Transf. 93 (2016) 554–565. https://doi.org/10.1016/j.ijheatmasstransfer.2015.09.031.

[96] Y. Liu, J. Tang, L. Li, Y.N. Shek, D. Xu, Design of Cassie-wetting nucleation sites in pool boiling, Int. J. Heat Mass Transf. 132 (2019) 25–33. https://doi.org/10.1016/j.ijheatmasstransfer.2018.11.146.

[97] A.R. Betz, J. Jenkins, C.J. Kim, D. Attinger, Boiling heat transfer on superhydrophilic, superhydrophobic, and superbiphilic surfaces, Int. J. Heat Mass Transf. 57 (2013) 733–741. https://doi.org/10.1016/j.ijheatmasstransfer.2012.10.080.

[98] A.S. Kousalya, J.A. Weibel, S. V. Garimella, T.S. Fisher, Metal functionalization of carbon nanotubes for enhanced sintered powder wicks, Int. J. Heat Mass Transf. 59 (2013) 372–383. https://doi.org/10.1016/j.ijheatmasstransfer.2012.12.030.

[99]   L. Courbin, J.C. Bird, M. Reyssat, H.A. Stone, Dynamics of wetting: From inertial spreading to viscous imbibition, J. Phys. Condens. Matter. 21 (2009). https://doi.org/10.1088/0953-8984/21/46/464127.

[100]   F. Blanchette, T.P. Bigioni, Partial coalescence of drops at liquid interfaces, Nat. Phys. 2 (2006) 254–257. https://doi.org/10.1038/nphys268.

[101]   N. Contet-Audonneau, J.L. Schmutz, A.M. Basile, C. De Bièvre, A new agent of onychomycosis in the elderly: Onychocola canadensis, Eur. J. Dermatology. 7 (1997) 115–117.

[102]   Y. Suh, R. Bostanabad, Y. Won, Deep learning predicts boiling heat transfer, Sci. Rep. 11 (2021) 1–10. https://doi.org/10.1038/s41598-021-85150-4.

[103]   A.K. Sasmal, C. Mondal, A.K. Sinha, S.S. Gauri, J. Pal, T. Aditya, M. Ganguly, S. Dey, T. Pal, Fabrication of superhydrophobic copper surface on various substrates for roll-off, self-cleaning, and water/oil separation, ACS Appl. Mater. Interfaces. 6 (2014) 22034–22043. https://doi.org/10.1021/am5072892.

[104]   Y.H. Lo, C.Y. Yang, H.K. Chang, W.C. Hung, P.Y. Chen, Bioinspired Diatomite Membrane with Selective Superwettability for Oil/Water Separation, Sci Rep. 7 (2017) 1426. https://doi.org/10.1038/s41598-017-01642-2.

[105]   S. Chu, Y. Cui, N. Liu, The path towards sustainable energy, Nat. Mater. 16 (2016) 16–22. https://doi.org/10.1038/nmat4834.

[106]   Q. Huang, F. Kang, H. Liu, Q. Li, X. Xiao, Highly aligned Cu 2 O/CuO/TiO 2 core/shell nanowire arrays as photocathodes for water photoelectrolysis, J. Mater. Chem. A. 1 (2013) 2418–2425. https://doi.org/10.1039/C2TA00918H.

[107]   H. Zhang, X. Yu, P. V. Braun, Three-dimensional bicontinuous ultrafast-charge and-discharge bulk battery electrodes, Nat. Nanotechnol. 6 (2011) 277–281. https://doi.org/10.1038/nnano.2011.38.

[108]   W. Zhou, J. Zhu, C. Cheng, J. Liu, H. Yang, C. Cong, C. Guan, X. Jia, H.J. Fan, Q. Yan, C.M. Li, T. Yu, A general strategy toward graphene@metal oxide core–shell nanostructures for high-performance lithium storage, Energy Environ. Sci. 4 (2011) 4954. https://doi.org/10.1039/c1ee02168k.

[109]   P.L. Taberna, S. Mitra, P. Poizot, P. Simon, J.M. Tarascon, High rate capabilities Fe3O4-based Cu nano-architectured electrodes for lithium-ion battery applications, Nat. Mater. 5 (2006) 567–573. https://doi.org/10.1038/nmat1672.

[110]   G. GUAN, Preferential CO oxidation over catalysts with well-defined inverse opal structure in microchannels, Int. J. Hydrogen Energy. 33 (2008) 797–801. https://doi.org/10.1016/j.ijhydene.2007.10.054.

[111]   M. Ren, R. Ravikrishna, K.T. Valsaraj, Photocatalytic Degradation of Gaseous Organic Species on Photonic Band-Gap Titania, Environ. Sci. Technol. 40 (2006) 7029–7033. https://doi.org/10.1021/es061045o.

[112] R. Chen, M.C. Lu, V. Srinivasan, Z. Wang, H.H. Cho, A. Majumdar, Nanowires for enhanced boiling heat transfer, Nano Lett. 9 (2009) 548–553. https://doi.org/10.1021/nl8026857.

[113] S. Li, R. Furberg, M.S. Toprak, B. Palm, M. Muhammed, Nature-inspired boiling enhancement by novel nanostructured macroporous surfaces, Adv. Funct. Mater. 18 (2008) 2215–2220. https://doi.org/10.1002/adfm.200701405.

[114] D.I. Yu, H.J. Kwak, H. Noh, H.S. Park, K. Fezzaa, M.H. Kim, Synchrotron x-ray imaging visualization study of capillary-induced flow and critical heat flux on surfaces with engineered micropillars, Sci. Adv. 4 (2018). https://doi.org/10.1126/sciadv.1701571.

[115] C. Zhang, J.W. Palko, M.T. Barako, M. Asheghi, J.G. Santiago, K.E. Goodson, Enhanced Capillary-Fed Boiling in Copper Inverse Opals via Template Sintering, Adv. Funct. Mater. 28 (2018). https://doi.org/10.1002/adfm.201803689.

[116] Y. Nam, S. Sharratt, G. Cha, Y.S. Ju, Characterization and Modeling of the Heat Transfer Performance of Nanostructured Cu Micropost Wicks, J. Heat Transfer. 133 (2011) 101502. https://doi.org/10.1115/1.4004168.

[117] T. Semenic, I. Catton, Experimental study of biporous wicks for high heat flux applications, Int. J. Heat Mass Transf. 52 (2009) 5113–5121. https://doi.org/10.1016/j.ijheatmasstransfer.2009.05.005.

[118] H.S. Ahn, G. Park, J. Kim, M.H. Kim, Wicking and spreading of water droplets on nanotubes, Langmuir. 28 (2012) 2614–2619. https://doi.org/10.1021/la204073n.

[119] I.-L. Ngo, C. Byon, Permeability of microporous wicks with geometric inverse to sintered particles, Int. J. Heat Mass Transf. 92 (2016) 298–302. https://doi.org/10.1016/j.ijheatmasstransfer.2015.08.040.

[120] S. Ravi, D. Horner, S. Moghaddam, Monoporous micropillar wick structures, I-Mass transport characteristics, Appl. Therm. Eng. 73 (2014). https://doi.org/10.1016/j.applthermaleng.2014.04.057.

[121] R. Aveyard, B.P. Binks, J.H. Clint, Emulsions stabilised solely by colloidal particles, Adv. Colloid Interface Sci. 100 (2003) 503–546. https://doi.org/Pii S0001-8686(02)00069-6Doi 10.1016/S0001-8686(02)00069-6.

[122] K. Stratford, R. Adhikari, I. Pagonabarraga, J.C. Desplat, M.E. Cates, Colloidal jamming at interfaces: a route to fluid-bicontinuous gels, Science (80-.). 309 (2005) 2198–2201. https://doi.org/10.1126/science.1116589.

[123] E.M. Herzig, K.A. White, A.B. Schofield, W.C. Poon, P.S. Clegg, Bicontinuous emulsions stabilized solely by colloidal particles, Nat Mater. 6 (2007) 966–971. https://doi.org/10.1038/nmat2055.

[124] M.E. Cates, P.S. Clegg, Bijels: a new class of soft materials, Soft Matter. 4 (2008) 2132. https://doi.org/10.1039/b807312k.

[125] M.N. Lee, A. Mohraz, Bicontinuous macroporous materials from bijel templates, Adv Mater. 22 (2010) 4836–4841. https://doi.org/10.1002/adma.201001696.

[126] M.N. Lee, A. Mohraz, Hierarchically Porous Silver Monoliths from Colloidal Bicontinuous Interfacially Jammed Emulsion Gels, J. Am. Chem. Soc. 133 (2011) 6945–6947. https://doi.org/10.1021/ja201650z.

[127] T.J. Thorson, E.L. Botvinick, A. Mohraz, Composite Bijel-Templated Hydrogels for Cell Delivery, ACS Biomater. Sci. Eng. 4 (2018) 587–594. https://doi.org/10.1021/acsbiomaterials.7b00809.

[128] M.N. Lee, M.A. Santiago-Cordoba, C.E. Hamilton, N.K. Subbaiyan, J.G. Duque, K.A. Obrey, Developing Monolithic Nanoporous Gold with Hierarchical Bicontinuity Using Colloidal Bijels, J Phys Chem Lett. 5 (2014) 809–812. https://doi.org/10.1021/jz5001962.

[129] J.W. Tavacoli, J.H.J. Thijssen, A.B. Schofield, P.S. Clegg, Novel, Robust, and Versatile Bijels of Nitromethane, Ethanediol, and Colloidal Silica: Capsules, Sub-Ten-Micrometer Domains, and Mechanical Properties, Adv. Funct. Mater. 21 (2011) 2020–2027. https://doi.org/10.1002/adfm.201002562.

[130] B. Holley, A. Faghri, Permeability and effective pore radius measurements for heat pipe and fuel cell applications, Appl. Therm. Eng. (2006). https://doi.org/10.1016/j.applthermaleng.2005.05.023.

[131] R. Xiao, E.N. Wang, Microscale liquid dynamics and the effect on macroscale propagation in pillar arrays, Langmuir. 27 (2011) 10360–10364. https://doi.org/10.1021/la202206p.

[132] T.T. Mai, C.Q. Lai, H. Zheng, K. Balasubramanian, K.C. Leong, P.S. Lee, C. Lee, W.K. Choi, Dynamics of wicking in silicon nanopillars fabricated with interference lithography and metal-assisted chemical etching, Langmuir. 28 (2012) 11465–11471. https://doi.org/10.1021/la302262g.

[133] M. Hilpert, A. Ben-David, Infiltration of liquid droplets into porous media: Effects of dynamic contact angle and contact angle hysteresis, Int. J. Multiph. Flow. 35 (2009) 205–218. https://doi.org/10.1016/j.ijmultiphaseflow.2008.11.007.

[134] K.A. White, A.B. Schofield, B.P. Binks, P.S. Clegg, Influence of particle composition and thermal cycling on bijel formation, J. Phys. Condens. Matter. 20 (2008). https://doi.org/10.1088/0953-8984/20/49/494223.

[135] M.N. Lee, J.H.J. Thijssen, J.A. Witt, P.S. Clegg, A. Mohraz, Making a Robust Interfacial Scaffold: Bijel Rheology and its Link to Processability, Adv. Funct. Mater. 23 (2013) 417–423. https://doi.org/10.1002/adfm.201201090.

[136] K.M. McDevitt, T.J. Thorson, E.L. Botvinick, D.R. Mumm, A. Mohraz, Microstructural characteristics of bijel-templated porous materials, Materialia. 7 (2019) 100393. https://doi.org/10.1016/j.mtla.2019.100393.

[137] K.R. Mangipudi, E. Epler, C.A. Volkert, Topology-dependent scaling laws for the stiffness and strength of nanoporous gold, Acta Mater. 119 (2016) 115–122. https://doi.org/10.1016/j.actamat.2016.08.012.

[138] J. Bear, Dynamics of fluid in porous media, Elsevier, New York, 1972.

[139] O. Stenzel, O. Pecho, L. Holzer, M. Neumann, V. Schmidt, Predicting effective conductivities based on geometric microstructure characteristics, AIChE J. 62 (2016) 1834–1843. https://doi.org/10.1002/aic.15160.

Appendix A. Uncertainty Analysis

Nanowire Porosity. The porosity is calculated by the number density N and diameter d of the nanowire arrays. The number density is calculated by counting the number of nanowires with large area (15 μm × 15 μm). Since the counted nanowire number is large enough (> 200) for the set 1 and set 2, the uncertainty associated with number density is considered negligible in the porosity calculation. Instead, the uncertainty in the diameter is identified based on the diameter distribution of each sample group. Therefore, the uncertainty in the porosity is

$$\left(\frac{\Delta\phi}{\phi}\right)^2 = \left(2\frac{\Delta d}{d}\right)^2 + \left(\frac{\Delta N}{N}\right)^2 \tag{A1}$$

Capillary performance parameter. The capillary performance parameter is a function of porosity, fluid viscosity, surface tension, wicking height, and measurement time. The uncertainty in the capillary performance parameter is given by

$$\left(\frac{\Delta K/R_{eff}}{K/R_{eff}}\right)^2 = \left(\frac{\Delta\sigma}{\sigma}\right)^2 + \left(\frac{\Delta\phi}{\phi}\right)^2 + \left(\frac{\Delta\mu}{\mu}\right)^2 + \left(2\frac{\Delta h}{h}\right)^2 + \left(\frac{\Delta t}{t}\right)^2 \tag{A2}$$

The fluid properties vary with the lab temperature 298 ± 2 K; therefore, the uncertainty in the surface tension and viscosity is 0.6% and 4.4%, respectively, which can be negligible. Also, the time frame of the camera is 60 fps, leading to the uncertainty around 8.4 ms, which can be negligible (< 0.015%) over the long measurement period. Therefore, the standard deviation of the wicking height is considered Δh to calculate the overall uncertainty.

Wicked volume flux. The wicked volume flux $\dot{V}''$ is calculated by droplet volume in spherical cap shape. The droplet volume is calculated by following equation:

$$V = \frac{\pi}{3}\left(\frac{R_d}{\sin\theta}\right)^3 (2 + \cos\theta)(1 - \cos\theta)^2 \tag{A3}$$

where R_d is the radius of the drawing area, θ is the contact angle. Then the wicked volume flux is calculated by the following equation:

$$\dot{V}'' = \frac{1}{A_d}\frac{dV}{dt} \tag{A4}$$

where t is the time and A_d is the drawing area. Therefore, the uncertainty in the $\dot{V}''$ is

$$\left(\frac{\Delta\dot{V}''}{\dot{V}''}\right)^2 = \left(\frac{\Delta R_d}{R_d}\right)^2 + \left(3\frac{\Delta\tan(\theta)}{\tan(\theta)}\right)^2 + \left(\frac{\Delta t}{t}\right)^2 \tag{A5}$$

Since the R_d and θ is recorded in high0speed camera with 320×192 pixels, the resolution for the R_d and θ is 1.52 µm and 1.02 °, respectively. Also, the images are captured in 5,000 fps, the time uncertainty is 0.2 ms.